

**INLINE MACH ZENDER INTERFEROMETER (IMZI) BASED
SENSORS FOR HUMIDITY AND BIOCHEMICAL CONCENTRATION
MEASUREMENTS**

ASIAH BINTI LOKMAN

**FACULTY OF ENGINEERING
UNIVERSITY OF MALAYA
KUALA LUMPUR**

2016

**INLINE MACH ZENDER INTERFEROMETER (IMZI) BASED
SENSORS FOR HUMIDITY AND BIOCHEMICAL CONCENTRATION
MEASUREMENTS**

ASIAH BINTI LOKMAN

**THESIS SUBMITTED IN FULFILLMENT OF THE REQUIREMENT
FOR THE DEGREE OF DOCTOR OF PHILOSOPHY**

**FACULTY OF ENGINEERING
UNIVERSITY OF MALAYA
KUALA LUMPUR**

2016

UNIVERSITY OF MALAYA
ORIGINAL LITERARY WORK DECLARATION

Name of Candidate: ASIAH LOKMAN

Registration/Matric No: KHA120042

Name of Degree: DOCTOR OF PHILOSOPHY

Title of Project Paper/Research Report/Dissertation/Thesis ("this Work"):

INLINE MACH ZENDER INTERFEROMETER (IMZI) BASED SENSORS FOR HUMIDITY AND BIOCHEMICAL CONCENTRATION MEASUREMENTS

Field of Study: PHOTONIC

I do solemnly and sincerely declare that:

- (1) I am the sole author/writer of this Work;
- (2) This Work is original;
- (3) Any use of any work in which copyright exists was done by way of fair dealing and for permitted purposes and any excerpt or extract from, or reference to or reproduction of any copyright work has been disclosed expressly and sufficiently and the title of the Work and its authorship have been acknowledged in this Work;
- (4) I do not have any actual knowledge nor do I ought reasonably to know that the making of this work constitutes an infringement of any copyright work;
- (5) I hereby assign all and every rights in the copyright to this Work to the University of Malaya ("UM"), who henceforth shall be owner of the copyright in this Work and that any reproduction or use in any form or by any means whatsoever is prohibited without the written consent of UM having been first had and obtained;
- (6) I am fully aware that if in the course of making this Work I have infringed any copyright whether intentionally or otherwise, I may be subject to legal action or any other action as may be determined by UM.

Candidate's Signature

Date:

Subscribed and solemnly declared before,

Witness's Signature

Date:

Name:

Designation:

UNIVERSITI MALAYA
PERAKUAN KEASLIAN PENULISAN

Nama: _____ (No. K.P/Pasport: _____)

No. Pendaftaran/Matrik:

Nama Ijazah:

Tajuk Kertas Projek/Laporan Penyelidikan/Disertasi/Tesis (“Hasil Kerja ini”):

Bidang Penyelidikan:

Saya dengan sesungguhnya dan sebenarnya mengaku bahawa:

- (1) Saya adalah satu-satunya pengarang/penulis Hasil Kerja ini;
- (2) Hasil Kerja ini adalah asli;
- (3) Apa-apa penggunaan mana-mana hasil kerja yang mengandungi hakcipta telah dilakukan secara urusan yang wajar dan bagi maksud yang dibenarkan dan apa-apa petikan, ekstrak, rujukan atau pengeluaran semula daripada atau kepada mana-mana hasil kerja yang mengandungi hakcipta telah dinyatakan dengan sejelasnya dan secukupnya dan satu pengiktirafan tajuk hasil kerja tersebut dan pengarang/penulisnya telah dilakukan di dalam Hasil Kerja ini;
- (4) Saya tidak mempunyai apa-apa pengetahuan sebenar atau patut semunasabahnya tahu bahawa penghasilan Hasil Kerja ini melanggar suatu hakcipta hasil kerja yang lain;
- (5) Saya dengan ini menyerahkan kesemua dan tiap-tiap hak yang terkandung di dalam hakcipta Hasil Kerja ini kepada Universiti Malaya (“UM”) yang seterusnya mula dari sekarang adalah tuan punya kepada hakcipta di dalam Hasil Kerja ini dan apa-apa pengeluaran semula atau penggunaan dalam apa jua bentuk atau dengan apa juga cara sekalipun adalah dilarang tanpa terlebih dahulu mendapat kebenaran bertulis dari UM;
- (6) Saya sedar sepenuhnya sekiranya dalam masa penghasilan Hasil Kerja ini saya telah melanggar suatu hakcipta hasil kerja yang lain sama ada dengan niat atau sebaliknya, saya boleh dikenakan tindakan undang-undang atau apa-apa tindakan lain sebagaimana yang diputuskan oleh UM.

Tandatangan Calon

Tarikh:

Diperbuat dan sesungguhnya diakui di hadapan,

Tandatangan Saksi

Tarikh:

Nama:

Jawatan:

ABSTRACT

Compact in-line fiber optic core cladding mode interferometers (CCMIs) have attracted much interest in recent years for various chemical, physical, and biological sensing applications. The working principle of CCMIs involves a mechanism to realize coupling and re-coupling between modes of the fiber core and fiber cladding. The core mode is guided by the core-cladding interface of the fiber while the cladding mode is guided by the cladding-ambience interface. Due to the optical phase difference (OPD) between the core and cladding modes, the CCMI could be used to measure various environmental parameters related to the ambience. This dissertation is concerned with the development of a simple and low cost fiber optics sensor based on interferometry modulated In-line Mach Zehnder Interferometer (IMZI). The proposed MZI structure is used to detect changes in relative humidity and various biochemical concentrations in distilled water. First, two main sensing methods are investigated; intensity modulation and interferometric technique are evaluated for RH measurements. A mixture of HEC and PVDF is used as a coating material for the tapered fiber. Then, the performance of the various sensors is investigated and compared. Next, a new sensor which is a dumbbell-shaped inline MZI is developed using an arcing process of a fusion splicer. The sensor probe consists of two bulges separated by a tapered waist that generates a good reflected interference spectrum. Lastly, Zinc Oxide (ZnO) nanowires structure is developed and used as a coating sensitive material for the IMZI sensor. ZnO was synthesized by aqueous solution of zinc nitrate hexahydrate ($\text{Zn}(\text{NO}_3)_2 \cdot 6\text{H}_2\text{O}$ (0.01 M) and hexamethylenetetramine (HMTA; $\text{C}_6\text{H}_{12}\text{N}_4$) (0.01 M) in deionized (DI) water. The performance of sensors with and without ZnO nanowires coating are investigated for both RH and uric acid concentration measurements. Overall, the proposed dumbbell shape MZI sensor has a high potential as it is easy to fabricate, cheap and compact.

ABSTRAK

Dalam beberapa tahun kebelakangan ini, kompak gentian optic teras-pelapisan interferometer (CCMI) telah menarik minat dalam aplikasi sensor untuk pelbagai bidang kimia, fizikal dan biologi. Prinsip kerja CCMI melibatkan mekanisma gandingan dan gandingan semula antara mod teras gentian dan serat pelapisan. Mod teras dipandu oleh permukaan teras pelapisan gentian manakala mod pelapisan dipandu oleh pelapisan dan keadaan permukaan sekitar. Oleh kerana perbezaan fasa optik (OPD) antara mod teras dan pelapisan, yang CCMI boleh digunakan untuk mengukur pelbagai parameter. Disertasi ini adalah mengenai pembuatan sensor gentian optic dengan kos yang rendah dan mudah berdasarkan prinsip interferometer Mach Zehnder (MZI). Struktur MZI yang dicadangkan digunakan untuk mengesan perubahan dalam kelembapan relatif (RH) dan pelbagai kepekatan biokimia dalam air suling. Pertama, dua kaedah disiasat; keamatan modulasi dan teknik Interferometrik digunakan untuk ukuran RH. Campuran HEC dan PVDF digunakan sebagai bahan salutan untuk gentian tirus. Kemudian, prestasi pelbagai sensor disiasat dan dibandingkan. Seterusnya, struktur sensor MZI terbaru diperkenalkan dengan menggunakan proses pengarkaan oleh mesin splicer. Struktur sensor terdiri daripada dua bonjolan yang dipisahkan oleh bahagian tirus dimana bonjolan-bonjolan bertindak sebagai pemisah dan penggabung untuk menghasilkan pantulan spektrum. Akhir sekali, Zink Oksida (ZnO) nanowayar dihasilkan dan digunakan sebagai bahan salutan untuk sensor IMZI itu. ZnO telah disintesis oleh larutan zink nitrat hexaydrate ($\text{Zn}(\text{NO}_3)_2 \cdot 6\text{H}_2\text{O}$ (0.01 M) dan hexamethylenetetramine (HMTA; $\text{C}_6\text{H}_{12}\text{N}_4$) (0.01 M) dalam air ternyahion (DI). Prestasi sensor dengan salutan dan tanpa salutan ZnO nanowayar disiasat untuk mengesan perubahan dalam kelembapan relatif dan pelbagai kepekatan asid urik dalam air suling. Secara keseluruhan, sensor MZI dicadangkan mempunyai potensi kerana ia mudah dihasilkan, murah dan kompak.

ACKNOWLEDGEMENTS

بِسْمِ اللَّهِ الرَّحْمَنِ الرَّحِيمِ

First and foremost I would like to thank the ALMIGHTY for the successful completion of this thesis. I wish to express my heartfelt indebtedness and deep sense of gratitude to both my Mentors and Supervisors, Prof. Dr. Sulaiman Wadi Harun and Prof Dr.Hamzah Arof. I want to express my profound thanks to them for giving me the independence in choosing my own subject of research, as well as for many fruitful discussions, which greatly contributed to my scientific work.

My appreciation also goes to the members of the Photonic Research Center especially, Malathy, Kak Husna, Zuraidah, Ninik, Kak Wati, Tan Sin Jin, Arni, Fauzan, Kemar, Salbiah and Iman. You have made the lab most enjoyable to work in despite the many challenges we have to put up with.

To my parents Lokman Abdullah and my late mother Hamidah Mohd Salleh, thank you for your encouragement and your prayers. My deepest thanks go to my husband MohD Hafiz Hassan for all your love and support, and to our children Yusuf and Najwa for the joy you bring and for cheering me up especially those days when research can be something of a pain rather than just pure pleasure.

Finally big thanks to all who helped me whether directly or indirectly during the making of this work.

TABLE OF CONTENTS

ABSTRACT	iii
ABSTRAK	iv
ACKNOWLEDGEMENTS	v
TABLE OF CONTENTS	vi
LIST OF FIGURES	ix
LIST OF TABLES	xiv
LIST OF SYMBOLS AND ABBREVIATIONS	xv
CHAPTER 1: INTRODUCTION	1
1.1 Background	1
1.2 Introduction to fiber-optic humidity sensor	2
1.3 Introduction to fiber-optic biochemical sensor (FOBS)	3
1.4 Research motivation	4
1.5 Research objectives	5
1.6 Thesis outline	5
1.7 Original Contributions	6
CHAPTER 2: BACKGROUND THEORY	8
2.1 Introduction	8
2.2 Optical Fiber Basic	8
2.3 Overview of Fiber Optic Sensors	10
2.4 Optical interferometer	13
2.5 Design Consideration of Interferometer for Sensing Application	17
2.6 Review on fiber-optic in-line interferometers based sensors	17
2.6.1 Grating type sensor	18
2.6.2 Tapered fiber based sensor	20
2.6.3 Compact in-line core cladding mode interferometer (CCMI)	21
2.7 Review on sensor coating sensitive material	25
2.7.1 Carbon Nanotubes	26
2.7.2 Zink Oxide Nanostructures	28

2.7.3	Thin film coating.....	31
2.8	Summary.....	33

CHAPTER 3: DEVELOPMENT OF EVANESCENT WAVE BASED FIBER

SENSORS FOR RELATIVE HUMIDITY MEASUREMENT.....		34
3.1	Introduction	34
3.2	Development of sensitive material for humidity.....	36
3.3	FOHS based on intensity modulation technique	39
3.3.1	Preparation of the sensor probe and experimental setup	39
3.3.2	Performance of the FOHS based on intensity modulation.....	42
3.4	FOHS based on interferometric technique	46
3.4.1	Performance of the FOHS based on transmission spectrum	47
3.4.2	Performance of the FOHS based on reflection spectrum.....	53
3.5	Fiber Bragg Grating (FBG) based humidity sensor	56
3.5.1	Preparation of the sensor probe and experimental setup	57
3.5.2	Performance of the FBG based RH sensor	60
3.6	Summary.....	62

CHAPTER 4: DEVELOPMENT OF NEW INLINE MACH-ZEHNDER

INTERFEROMETER (IMZI) FOR SENSING APPLICATIONS.....		64
4.1	Introduction	64
4.2	Fabrication of in-line MZI.....	66
4.3	The operation principle and transmission characteristic of the dumbbell shaped MZI.....	70
4.4	Dumbbell shape MZI for Relative Humidity measurement.....	78
4.4.1	Experimental arrangement for RH sensor	79
4.4.2	Performance of the inline dumbbell shaped MZI based RH sensor	80
4.5	Dumbbell shape MZI for Bio-Chemical detection	85
4.5.1	Experimental Set-up.....	86
4.5.2	Effect of Temperature on Bio-Chemical Sensing	94
4.5.3	Multiple Linear Regression Analysis using SPSS Statistics software....	97
4.6	Summary.....	98

CHAPTER 5: INLINE MACH-ZEHNDER INTERFEROMETER (IMZI) WITH ZNO NANOWIRES COATING FOR THE MEASUREMENTS OF HUMIDITY AND URIC ACID CONCENTRATIONS	100
5.1 Introduction.....	100
5.2 Synthesis of Zink Oxide Nanostructure	102
5.3 Relative Humidity (RH) Sensor Based on Inline Mach ZehndeInterferometer with ZnO Nanowires Coating.....	105
5.4 Inline Mach Zehnder Interferometer with ZnO Nanowires Coating for the measurement of uric acid concentrations	113
5.4.1 Experimental arrangement for uric acid sensing.....	115
5.4.2 Performance of the proposed uric acid sensor.....	116
5.5 Summary.....	119
CHAPTER 6: CONCLUSION AND FUTURE WORK	121
6.1 Conclusion.....	121
6.2 Future Work	126
REFERENCES.....	127
LIST OF PUBLICATION AND PAPERS PRESENTED	142
APPENDIX.....	144

LIST OF FIGURES

Figure 2.1: Basic structure of optical fiber	9
Figure 2.2 : Total internal reflection in an optical fiber.....	10
Figure 2.3: Schematic diagram of a typical intensity based fiber-optic sensor	12
Figure 2.4: Schematic diagram of a typical phase modulated sensor utilizing MZI	13
Figure 2.5: Fabry-Perot optical fiber interferometer (a) reflection (b) transmission.....	15
Figure 2.6: Sagnac optical fiber interferometer	15
Figure 2.7: Michelson optical fiber interferometer.....	16
Figure 2.8: Schematic diagram of a Mach-Zehnder interferometer.....	16
Figure 2.9: FBG (a) periodic structure (b) refractive index modulation inside fiber's core and (c) spectral response	19
Figure 2.10: The in-line MZI structures based on (a) three tapers and (b) misaligned spliced joint.....	23
Figure 2.11: Schematic diagram of two in-line MIs based on (a) the fiber taper and (b) the core offset structure.....	24
Figure 2.12: Single walled nanotubes (SWNTs) and multi-walled nanotubes (MWNTs) (Scarselli, Castrucci, & De Crescenzi, 2012).....	27
Figure 2.13: ZnO nanostructures in various morphologies	30
Figure 3.1: Procedure to prepare the HEC/PVDF mixture	38
Figure 3.2: The polymer composite solution and its microscopic image	38
Figure 3.3: Fiber tapering rig used in this study	40
Figure 3.4: Microscopic images of the tapered fiber (a) without and (b) with the HEC/PVDF composite coating	41
Figure 3.5: Experimental setup for the proposed sensor to detect change in RH using the tapered fiber coated with HEC/PVDF composite. Abbreviation 'ASE' means an amplified spontaneous emission and 'OSA' an optical spectrum analyzer.	42

Figure 3.6: The output spectra of the transmitted light from the tapered fiber with and without HEC/PVDF composite coating.....	43
Figure 3.7: Output power versus relative humidity with linear fitting	44
Figure 3.8: The output power versus relative humidity with a quadratic fitting trend ...	45
Figure 3.9: Microscopic images of the SMF (a) Before etching (with a diameter of 125 μm), (b) Etched SMF for 30 minutes (with final diameter of 50 μm), and (c) Etched SMF for 10 minutes (with final diameter of 87.5 μm) (d) Etched SMF coated with HEC/PVDF composite.....	47
Figure 3.10: Experimental setup of our RH sensor based on transmission spectrum.....	48
Figure 3.11: Transmission spectra of our sensor measured at different relative humidity percentages (60, 70 and 80) for the cases of tapered-fibre diameters being equal to (a) 50 μm and (b) 87.5 μm	50
Figure 3.12: Shifts observed for the wavelength transmittance maximum with increasing relative humidity from 10 to 80%.....	52
Figure 3.13: Wavelength shift against RH within a RH range from 20 to 45 %.....	52
Figure 3.14: Experimental setup for the proposed sensor to detect change in relative humidity using the tapered fiber (via etching technique) coated with HEC/PVDF composite.....	53
Figure 3.15: The variation of reflected spectra under different RH levels for the RH sensor configured with tapered fiber probe.	54
Figure 3.16: The sensor response to humidity measured using resonant wavelength shift in the proposed sensor based on reflection.	55
Figure 3.17: The linear relationship between humidity and resonant wavelength shift within 20 to 45% RH range.....	56
Figure 3.18: Microscope image of the FBG before and after etching with HF.....	58
Figure 3.19: The reflection spectrum of the FBG before and after etching process.....	59

Figure 3.20: Measured reflection spectra of the FBG sensor under different reflective humidity levels	61
Figure 3.21: Wavelength shift versus relative humidity for the proposed FBG sensor..	61
Figure 3.22: Linear relationship between the wavelength shift and relative humidity within the range of 20-45% and 50-80%.	62
Figure 4.1 : (a) Striping and (b) cleaving of a bare SMF.....	67
Figure 4.2: The image of a fusion splicer machine (Sumitomo Type 39). Inset shows the image of the working area.....	68
Figure 4.3: Three steps in fabricating the MZI structure (a) end facets of two fibers are matched and aligned using a manual operation (b) The first bulge of MZI structure is formed using a multiple arching process. (c) The second bulge is formed in a similar fashion.....	69
Figure 4.4: The microscope image of the fabricated dumbbell shaped MZI.....	69
Figure 4.5: Core and cladding modes propagation inside the proposed dumbbell shape MZI	70
Figure 4.6: Bulges of MZI with diameter of (a) 177 μm (b) 183 μm and (c) 195 μm ...	72
Figure 4.7: The transmission spectra of the MZI for three different bulge diameters	72
Figure 4.8: The output spectrum for the two dumbbell sensors with different length L	73
Figure 4.9: The experiments set-up for the thermo-optic and thermal expansion	75
Figure 4.10: Temperature response of the MZI with L=0.5cm	75
Figure 4.11: Temperature response of the MZI with L=0.1cm	76
Figure 4.12: The wavelength shift against the temperature	77
Figure 4.13: The experimental setup for the proposed dumbbell shape MZI based sensor to detect change in RH.....	80
Figure 4.14: The variation of spectra under different RH levels	82
Figure 4.15 : The sensor response to humidity measured using resonant wavelength shift for MZI dumbbell structure.	83

Figure 4.16: The linear relationship between humidity and resonant wavelength shift .	84
Figure 4.17: The reversibility of MZI-based sensor for two different runs	84
Figure 4.18: The experimental setup of the proposed biochemical sensors	86
Figure 4.19: Reflected spectrum from the dumbbell shape MZI immersed into various glucose concentrations	88
Figure 4.20: The relation between one of the measured dip wavelengths of the interference spectrum and the glucose concentration in distilled water	89
Figure 4.21: The measured dip wavelength of the interference spectrum against the sodium chloride concentration in distilled water	91
Figure 4.22: The measured dip wavelength of the interference spectrum against the glucose concentration in distilled water	91
Figure 4.23: The output comb spectrum of the sensor at various uric acid concentrations in DI water solution	92
Figure 4.24: The wavelength change of one of the transmission dips with the increase in uric acid concentration	93
Figure 4.25: The effect of temperature on glucose solution	95
Figure 4.26: The effect of temperature on NaCl solution	95
Figure 4.27: The effect of temperature on uric acid solution.....	96
Figure 4.28: The wavelength change of one of the transmission dips with the increases of temperature	96
Figure 5.1: The procedure to prepare the ZnO composite	104
Figure 5.2: The ZnO solution was kept for 24 hours before use	104
Figure 5.3: Microscope and FESEM images of the sensor probe coated with ZnO.....	105
Figure 5.4: The microscope image of the fabricated dumbbell shaped IMZI.....	107
Figure 5.5: The experimental setup for the proposed RH sensor to detect change in RH using the fabricated inline dumbbell shaped MZI coated with ZnO nanowires.	108

Figure 5.6: The variation of spectra under different RH levels for the RH sensor configured with IMZI fiber probe.....	110
Figure 5.7: The linear relationship between humidity and resonant wavelength shift for with and without coated ZnO.....	111
Figure 5.8: The reversibility of the results obtained for two different runs (relative humidity).....	112
Figure 5.9 : The experimental setup used to detect different uric acid concentration using the inline MZI dumbbell structures	115
Figure 5.10: An interference pattern for without ZnO composite	117
Figure 5.11: An interference pattern for with ZnO composite	117
Figure 5.12: The wavelength change of one of the transmission peaks with the increase in uric acid concentration.....	118
Figure 5.13: The reversibility of the results obtained for two different runs.....	119

LIST OF TABLES

Table 3.1: The performance of humidity sensor using interferometric technique.....	63
Table 4.1: The characteristic of the IMZI sensors	77
Table 4.2: Performance of Bio-Chemical Sensors.....	94
Table 4.3: The summary of test analysis.....	98
Table 5. 1: The comparison of the proposed RH sensor.....	111
Table 5.2: The performance of the proposed uric acid detection sensor	119
Table 6.1 :The performance of humidity sensor using interferometric technique.....	123

University of Malaya

LIST OF SYMBOLS AND ABBREVIATIONS

n	Index of refraction
v	The light speed
c	Light speed in vacuum space
θ_1, θ_2	Angles between the incident and the refracted beams
θ_c	Critical angle
n_{eff}	Optical fiber core effective refractive index
A	Refractive index modulation
λ_B	Bragg wavelength
I	Intensity of the interference signal
φ	Phase difference between the core and cladding modes.
Δn_{eff}	Effective refractive indices
L	Length of the interferometer region
λ	The input wavelength.
α_{TOC}	Thermal-optic coefficient (TOC)
α_{TEC}	Thermal expansion coefficient (TEC)
y_i	Dependent variable
X_i	Independent variables
β_1, β_n	Coefficients of independent variables
IMZI	In-line Mach Zehnder Interferometer
RH	Relative Humidity
FOHS	Fiber Optic Humidity Sensors
FBGs	Fiber Bragg Gratings
HPLC	Liquid Chromatography
MFC	Microfiber Coupler
HEC	Hydroxyethylcellulose
PVDF	Polyvinylidene fluoride
MLR	Multiple Linear Regression
FPI	Fabry-Perot Interferometers
SI	Sagnac Interferometer

MI	Michelson Interferometer
MZI	Mach-Zehnder Interferometer
HF	Hydrofluoric
SiO ₂	Silicon Dioxide
CCMI	Core Cladding Mode Interferometer
OPD	Optical Phase Difference
MMF	Multimode Fiber
SMF	Single Mode Fiber
Nm	Nanometer
CNT	Carbon Nanotube
SWNT	Single Walled Nanotubes
MWNT	Multi-Walled Nanotubes
POF	Plastic Optical Fiber
ZnO	Zink Oxide
VLS	Vapour-Liquid-Solid
PVD	Physical Vapour Deposition
CVD	Chemical Vapour Deposition
VOC	Volatile Organic Compounds
ISAM	Ionic Self-Assembled Monolayer
ASE	Amplified Spontaneous Emission
OSA	Optical Spectrum Analyzer
RI	Refractive Index
OPD	Optical Phase Difference
FSR	Free Spectral Range
ER	Extinction Ratio
NaCl	Sodium Chloride
PEO	Polyethylene Oxide
DI	Distilled
FESEM	Field Emission Scanning Electron Microscope
LOD	Limit of Detection

CHAPTER 1: INTRODUCTION

1.1 Background

Fiber-optic technology has grown rapidly since its successful inception in the 1970's (Grattan & Meggitt, 1995; Kasap, 2012). It has revolutionized telecommunication network due to its outstanding advantages of low loss and large bandwidth. According to Charles K Kao, one of the pioneers of glass fibers for optical communications, "the low-transmission loss and the large bandwidth capability of the fiber systems allow signals to be transmitted for establishing communication contacts over large distances with few or no provisions of intermediate amplification". He was jointly awarded the 2009 Nobel Prize in Physics for his ground-breaking achievements concerning the transmission of light in fibers for optical communication (Kasap, 2012).

The expansion and subsequent mass production of components to sustain the fiber optic communication industry have spurred a major development to optical sensor technology (Culshaw, 1984; López-Higuera, 2002; Udd & Spillman Jr, 2011). Currently, fiber optics sensors have been extensively used in sensing applications of various physical, chemical and even biological parameters. Fiber optics sensors offer a lot of advantages over conventional sensors including compactness, small size, fast response, high resolution, high sensitivity, good stability, good repeatability and immunity to electromagnetic interference in various applications.

This dissertation is concerned with the development of a simple and low cost fiber optics sensor based on interferometry modulated In-line Mach Zehnder Interferometer (IMZI). The MZI is fabricated using an arcing process of a fusion splicer to form two bulges, which are separated by a tapered waist. This MZI is sensitive to changes in the

refractive index of its surrounding. Here, the proposed MZI structure is used to detect changes in relative humidity and various biochemical concentrations in distilled water.

1.2 Introduction to fiber-optic humidity sensor

Relative humidity (RH) is a measure of wetness or dryness of the atmosphere. It is defined as the ratio of the water vapor in air to the maximum amount of water vapor under a certain temperature and pressure. The monitoring of humidity is crucial for numerous chemical, steel and biomedical industries, where humidity may affect the health of workers and the quality of products. Humidity sensors are also used to monitor the health of big structures such as bridges or planes so that possible risk of leakage due to corrosion can be predicted (Sun, Li, Wei, Li, & Cui, 2009). Therefore relative humidity measurement has been extensively studied and a great variety of sensors, including capacitive, resistive, thermal conductivity and optical have been developed for this purpose. So far, electronic humidity sensors dominate the market because their technology of fabrication is well established. However, the field of optical fiber sensors has grown enormously since the 60's and at the present, there exist niche applications where optical fiber humidity sensors can advantageously compete with the electronics sensors.

Fiber optic humidity sensors (FOHS) use optical fiber technology to guide a light signal which is modulated by the ambient humidity and then collected back by a detector, conditioned and processed. Thanks to the low attenuation and large wideband operating range of the fiber, it is possible to transmit large sensor data over kilometer distances. In addition, the use of several interrogating techniques enables the existence of distributed humidity sensors configurations (Q. Wu, Semenova, Wang, & Farrell, 2011) . There are also a number of applications where possible electric hazard posed by the electronic sensor itself or electromagnetic interference that is present in the surrounding

environment dictate the use of fiber optic sensors. In some fields, accessibility can be limited and the implementation of light-weight systems using sensors that are small in dimension and simple in geometry is preferable so that they can be easily embedded into the construction materials.

To date, a wide range of relative humidity (RH) sensing techniques based on optical fibers have been reported including the ones using long period gratings (Del Villar, Zamarreño, Hernaez, Arregui, & Matias, 2010), fiber Bragg gratings (FBGs) (Miao et al., 2009), side polished fibers (Alvarez-Herrero, Guerrero, & Levy, 2004), plastic optical fibers (Muto, Suzuki, Amano, & Morisawa, 2003), and surface plasmon resonance (Qi, Honma, & Zhou, 2006). These FOHS have been used in applications traditionally in the domain of conventional sensors (Yeo, Sun, & Grattan, 2008).

1.3 Introduction to fiber-optic biochemical sensor (FOBS)

According to the Obesity Prevention Council President in Malaysia, 3.6 million adults are estimated to be affected by diabetes. Nowadays in Malaysia, diabetes or high blood glucose is one of major disease caused by abnormal amount of glucose in blood. Diabetes can be efficiently managed, but potential complications include heart disease, stroke, and kidney damage. Apart from diabetes, high blood pressure is also a concern. Chronic high blood pressure can stealthily cause vessel changes in the back of the eye (retina), abnormal thickening of heart muscle and brain damage. One of factor that cause this problem is the unusual level of sodium in human serum. Meanwhile, uric acid is a product of metabolic break-down of purine nucleotides. Abnormal levels uric acid in human serum and urine are related to several medical complications such as gout, Lesh-Nyhan syndrome, and renal failure. Therefore, the need for biochemical sensors that can detect these chemicals is pressing (Arora, Tomar, & Gupta, 2014; Erden & Kılıç, 2013; Peng, 2013).

Conventional techniques that have been developed to detect the levels of these chemicals in human body include liquid chromatography (HPLC) (Ferin, Pavão, & Baptista, 2013; N. A. Rahman, Hasan, Hussain, & Jahim, 2008), enzymatic assay (Thakur & Sawant, 2013) and other electrochemical (Khan, Haque, & Kim, 2013) processes. Of late, optical fiber sensors have also been used to detect physical parameters as well as chemical compounds (Gehrich et al., 1986; Mignani & Baldini, 1996). For instance, a compact micro-ball lens structure fabricated at the cleaved tip of a microfiber coupler (MFC) was used for sensing various glucose concentrations in deionized water (Harun, Jasim, Rahman, Muhammad, & Ahmad, 2013). A tapered multimode fiber could also be used as a sensor probe for detecting different concentration of sodium chloride (NaCl) in de-ionized water (H. Rahman et al., 2011). A tapered Plastic Optical Fiber coated with Zink Oxide was demonstrated for sensing uric acid concentration (M Batumalay et al., 2014). These research works show that fiber-optic sensors have a great potential for applications in biochemical sensing.

1.4 Research motivation

To solve some issues associated with conventional fiber-optic sensors such as having complicated configuration or being bulky and expensive; a miniature IMZI based dumbbell structure is proposed. The new IMZI structure offers several advantages as it is easy to fabricate, economical and has a good repeatability.

1.5 Research objectives

This thesis introduces a new fiber-optic sensor based on a simple, compact and low cost In-Line Mach Zehnder Interferometer (IMZI) structure for relative humidity (RH) and biochemical concentration measurements. The new IMZI structure is dumbbell shaped, consisting of two bulges separated by a tapered waist. The following objectives are outlined to guide this research work.

1. To evaluate various sensing techniques for RH and biochemical concentrations.
2. To fabricate a new IMZI based on dumbbell structure using a fusion splicing machine as a compact, easy to fabricate and low cost sensor probe.
3. To investigate the performance of IMZI based on dumbbell structure for measurement of RH.
4. To investigate the performance of IMZI based on dumbbell structure for measurement of biochemical sensors.

1.6 Thesis outline

The thesis is organized as follows. Chapter 1 presents the background, motivation and objective of this study. Chapter 2 reviews various related topics including optical fiber, fiber sensors, interferometers and sensitive coating materials. Chapter 3 describes two main RH sensing methods for tapered fiber which are intensity modulation and interferometric techniques. It also elaborates on hydroxyethylcellulose (HEC) and polyvinylidene fluoride (PVDF) used as a coating material for the tapered fiber. Finally, the performance of the sensors using different coating materials is investigated and compared.

Chapter 4 discusses the development of a new dumbbell-shaped inline MZI using an arcing process of a fusion splicer for RH measurement and detecting bio-chemical concentration in distilled water. The sensor probe consists of two bulges separated by a tapered waist that generates a good reflected interference spectrum. Important parameters and characteristics of Inline MZI are introduced, then the performance of the sensor is analyzed. Finally, multiple linear regression (MLR) analysis is carried out using a statistical software where the dependent variable is wavelength shift and the independent variables are the biochemical concentration and temperature.

Chapter 5 proposes ZnO nanowires structure as a coating material for the inline MZI for both RH and uric acid concentration measurements. Both measurements are based on interferometric technique where change in the transmission spectrum of the reflected light is related to the change in the refractive index of the surrounding. The performance of both sensors is investigated for the probe with and without ZnO nanowires coating. Chapter 6 concludes the overall study and offers possible future works.

1.7 Original Contributions

The main contributions of this thesis are listed as follows;

- 1 Fabrication of two main sensing methods: intensity modulation and interferometric technique for RH measurements using tapered fiber coated with new material HEC/PVDF .
- 2 Fabrication of new dumbbell-shaped inline MZI using arcing process of a fusion splicer.
- 3 The optimization of parameter and characteristics of inline MZI.
- 4 Development of ZnO nanowires structures as coating material.

- 5 Demonstration of inline MZI as a sensor probe coated with HEC/PVDF for various relative humidity detection.
- 6 Demonstration of inline MZI as a sensor probe for various concentration of biochemical in distilled water.
- 7 Demonstration of inline MZI as a sensor probe coated with ZnO nanowires structure for various relative humidity detection.
- 8 Demonstration of inline MZI as a sensor probe coated with ZnO nanowires structure for various concentration of uric acid in distilled water.

University of Malaya

CHAPTER 2: BACKGROUND THEORY

2.1 Introduction

Optical fibers have played a major role not only in communication but also in sensing application. Every year, new concepts and constructions for optical fiber sensors are tested for sensing physical, biochemical, mechanical and structural parameters. Optical fiber sensors offer several advantages such as sensitivity, lightweight, compactness and immunity to electromagnetic interference that make them attractive and preferable in various applications. The main objective of this thesis is to propose and demonstrate new fiber-optic sensors based on a simple, compact and low cost in-Line Mach Zehnder Interferometer (MZI) structure for relative humidity (RH) and biochemical concentration measurements. In this chapter, a thorough literature review on this topic is presented. General principles of optical fiber and fiber sensors and in particular a review on interferometers and sensor coating sensitive materials is discussed in this chapter.

2.2 Optical Fiber Basic

Optical fibers were initially used for telecommunications where they were designed for transmitting light over long distances with little loss in intensity (Keiser, 2003). Materials used for the optical fiber is typically silica glass or polymer. Figure 2.1 shows the typical structure of a fiber. The center is called core, which is surrounded by a layer called cladding. The fiber structure is designed so that the index of refraction of the cladding material is less than that of the core material. This structure confines the light within the core and guides the light to propagate in the direction parallel to fiber's axis.

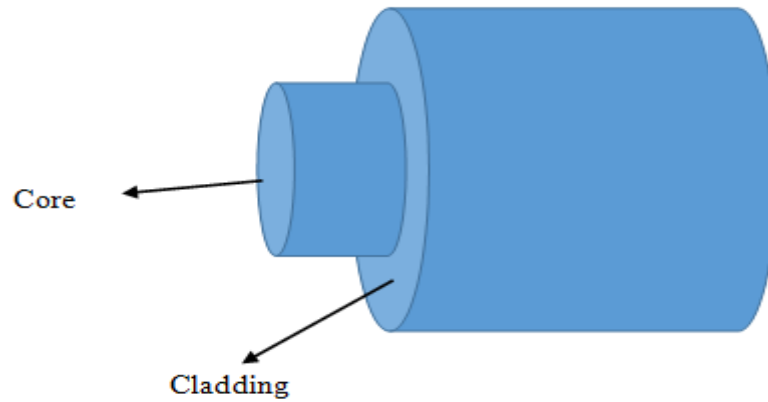


Figure 2.1: Basic structure of optical fiber

The ratio of the speed of light in a vacuum to that in the matter is the index of refraction n of the material;

$$n = \frac{c}{v} \quad (2.1)$$

where $c = 3 \times 10^8 \text{ m/s}$, a light speed in vacuum space, v is the light speed in the matter. The difference of the speed of light in two materials with different refractive indices changes the direction of light travelling at the interface between two materials. If n_1 and n_2 are the refractive indices of two materials, at the interface it follows Snell's law

$$n_1 \sin \theta_1 = n_2 \sin \theta_2 \quad (2.2)$$

where θ_1 and θ_2 are the angles between the incident and the refracted beams respectively with respect to the normal of the surface. If $n_1 > n_2$, then $\theta_1 < \theta_2$. If θ_1 is increased, θ_2 will also increase. When θ_2 reaches 90° , θ_1 becomes the so-called critical angle θ_c .

$$\theta_c = \sin^{-1} \frac{n_2}{n_1} \quad (2.3)$$

when θ_1 is greater than the critical angle, the total internal reflection is happened; the light is totally reflected back and does not pass through the interface to escape out of the fiber as shown in Figure 2.2. Total internal reflection is the mechanism of light propagating

along a fiber by using the cladding with n_2 to reflect the light back to the core with n_1 ($n_1 > n_2$) (Udd, Michal, Watanabe, Theriault, & Cahill, 1988).

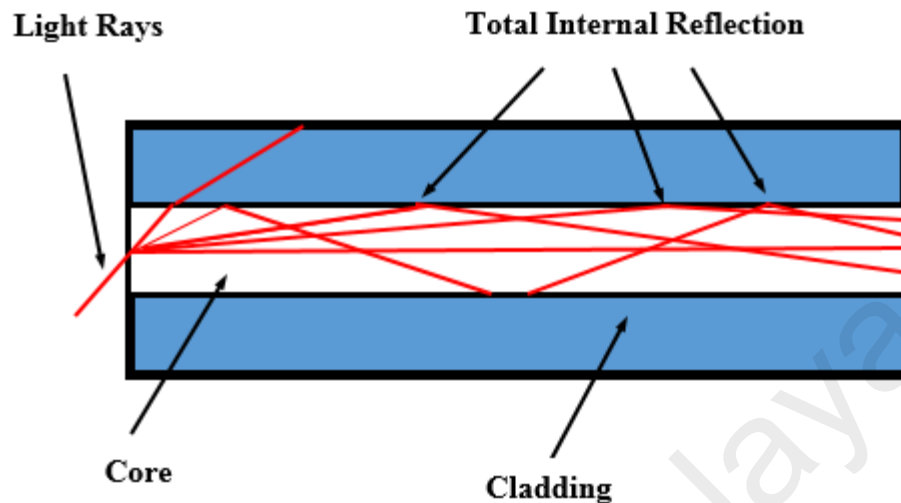


Figure 2.2 : Total internal reflection in an optical fiber

2.3 Overview of Fiber Optic Sensors

Fiber optic sensor technology has been an important user of technology related with the optoelectronic and fiber optic communication industry (Udd et al., 1988). Currently, as component prices have reduced and quality enhancements have been made, the ability of fiber optic sensors to replace several traditional sensors for temperature, pressure, biochemical, humidity and other sensor applications have also increased (Golnabi, 2000). Additionally, fiber optic sensor offers many advantages over conventional electronic sensors which include their easy integration into a wide variety of structure, incapability to conduct electric current, robust and more immune to harsh environments. Environmental and atmospheric monitoring, industrial chemical processing, utilities and biotechnology, as well as defense and security, are some of the areas that find use for fiber optic sensors.

With increasing emphasis on safeguarding the environment, fiber-optic sensors are being employed to measure pollutant levels and contamination in the environment in real time. The multiplexing capability of fiber optic sensors makes them an excellent candidate for structural health monitoring in aerospace and satellite applications where weight is a major consideration. It can also be used remotely to monitor several chemical processes in otherwise hazardous conditions. In medicine, there has been a tremendous growth in the field of biomedical optics and optical technology. Fiber optics has been found extremely useful in implementing non-invasive imaging techniques like optical coherence tomography and delivering laser light into internal organ tissues via optical fiber conduit. The field of optical sensing is bound to prosper as new technologies are being developed and tested continuously for a multitude of sensing applications.

Fiber optic sensors can be broadly divided into two basic categories; intensity modulated and phase or wavelength modulated sensors (Tracey, 1991). Intensity-modulated sensors detect the amount of light that is a function of the perturbing environment, as shown in Figure 2.3. Physical perturbation interacts with the fiber or a mechanical transducer attached to the fiber. The perturbation causes a change in received light intensity, which is a function of the phenomenon being observed. Intensity-modulated sensors normally require more light to function better than the phase-modulated sensors do. Hence, plastic optical fibers are generally used for intensity-modulated sensors.

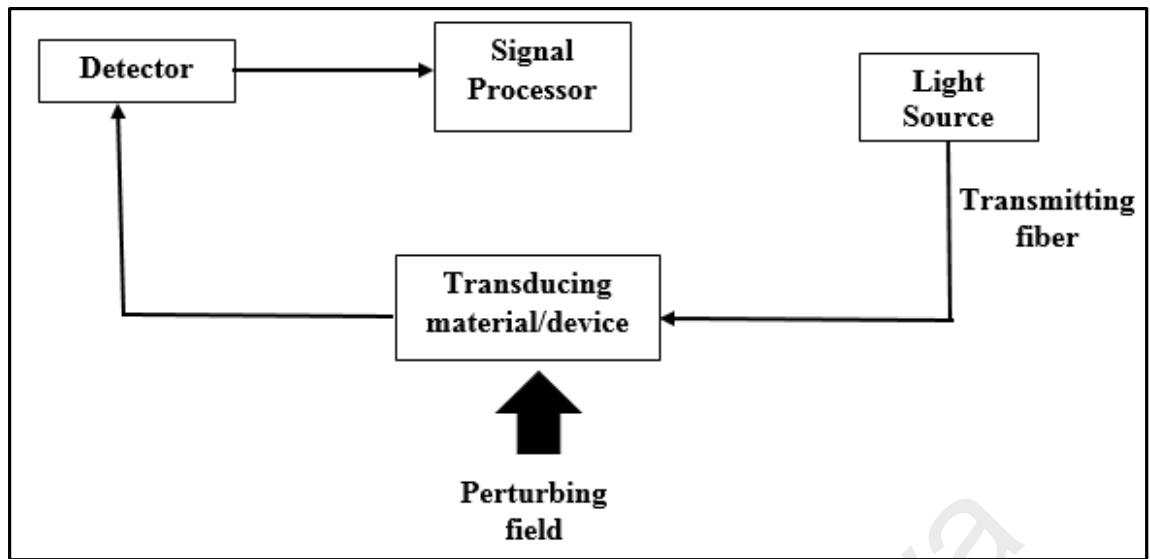


Figure 2.3: Schematic diagram of a typical intensity based fiber-optic sensor

Since phase-modulated sensors use interferometric techniques to detect physical perturbations, they are much more accurate than intensity-modulated sensors. Figure 2.4 shows a schematic diagram of a typical Mach Zehnder interferometer (MZI) setup. The laser light source is split such that it travels in the reference fiber and the sensing fiber, which is exposed to the perturbing environment. If the light in the reference arm is exactly in phase with the sensing arm, they constructively interfere resulting in an increased light intensity. If they are out of phase, destructive interference occurs and the received light intensity is lower. Such a device experiences a phase shift if the sensing fiber under the influence of perturbation has a length or refractive index change or both. Fabry-Perot, Michelson and Sagnac interferometers could also be used for a phase-modulated sensor. In this research, we have used inline MZI with dumbbell shape structure made of silica optical fiber for the proposed sensing devices.

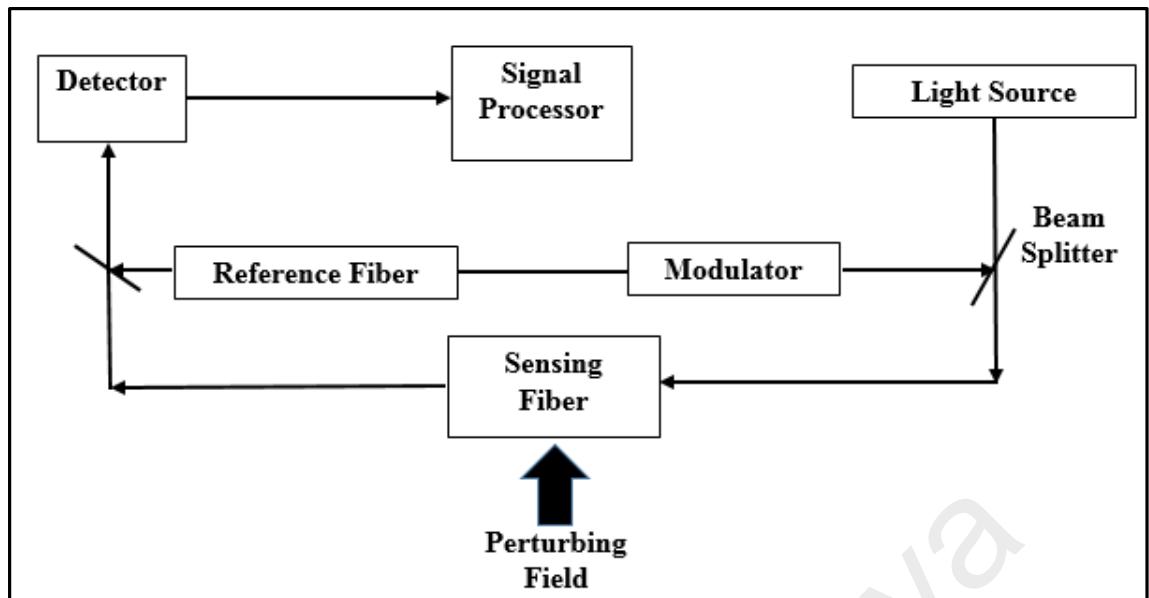


Figure 2.4: Schematic diagram of a typical phase modulated sensor utilizing MZI

2.4 Optical interferometer

Interferometry is the technique of superimposing two (or more) waves to obtain interference spectrum due to the phase differences between these waves. An interferometer utilizes two waves with the same wavelength. If they have the same phase, their electric fields will add to each other constructively; otherwise, if there is a 180° phase difference between them they add destructively. Typically, an incoming light wave is split into two (or more) parts, and then combined together to create an interference pattern after traveling different optical paths. Optical paths different by an integral number of wavelengths (or odd multiple of half wavelengths, i.e. 180° out of phase) correspond to constructive (or destructive) interference. In terms of the optical spectrum, the minimum attenuation wavelength can be “shifted” to maximum attenuation wavelength if the optical path difference varies by 180° . Based on the maximum (or minimum) attenuation wavelength shift one can tell the phase difference induced by the environmental (i.e. refractive index or strain) change, hence the interferometer can be utilized as a sensor. Different configurations of interferometers have been realized with

the optical fibers, i.e. Fabry-Perot interferometers (FPI) (Jiang & Gerhard, 2001), Sagnac interferometer (SI) (Blake, 1997), Michelson Interferometer (MI) (Lucki, Bohac, & Zeleny, 2014) and Mach-Zehnder interferometer (MZI) (Choi, Kim, & Lee, 2007).

A Fabry-Perot Interferometer (FPI) are widely used in telecommunications, lasers and spectroscopy for controlling and measuring the wavelength of light (Jiang & Gerhard, 2001). Figure 2.5 shows two different optical fiber based FPI. One is based on the reflection while the other on transmission. A FPI is typically made of a transparent plate with two reflecting mirrors.

A Sagnac Interferometer (SI) is made by two splitting light waves, which are propagating in opposite directions as shown in Figure 2.6. It is based on Sagnac configuration (Blake, 1997) (Lofts, Ruffin, Parker, & Sung, 1995) where the interference spectrum is realized due to the interaction between these two waves. Information about the waves can be extracted from the resulting interference of the waves which are examined in order to detect very small changes in the waves' properties. This method is suitable in a variety of applications including measurement, sensing and lasers (Hariharan, 2003).

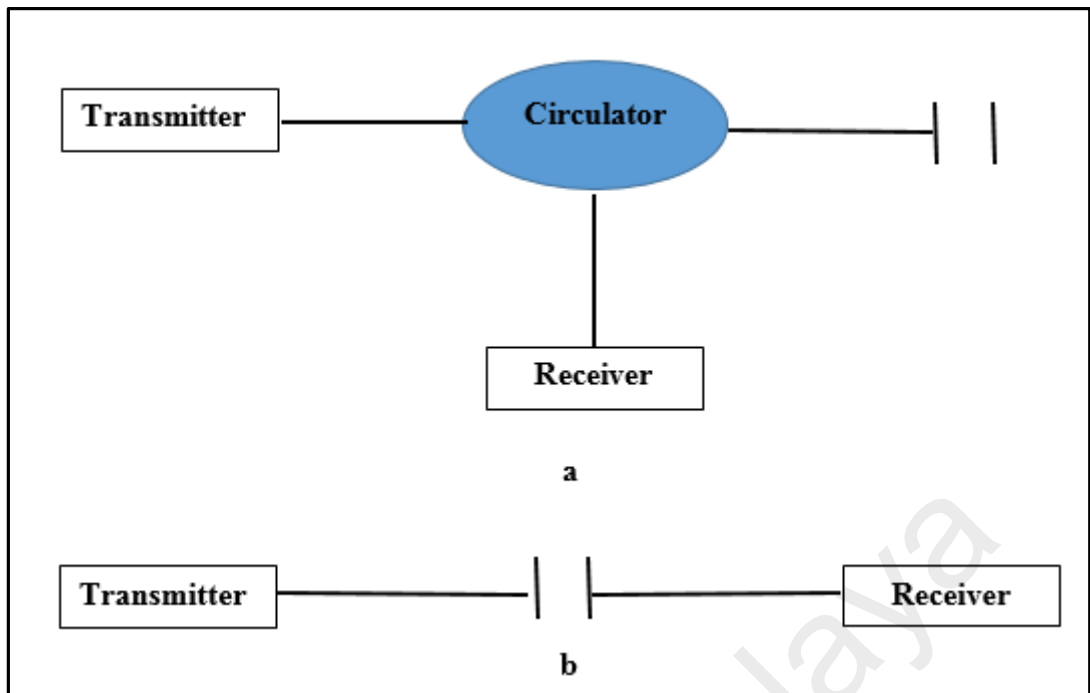


Figure 2.5: Fabry-Perot optical fiber interferometer (a) reflection (b) transmission

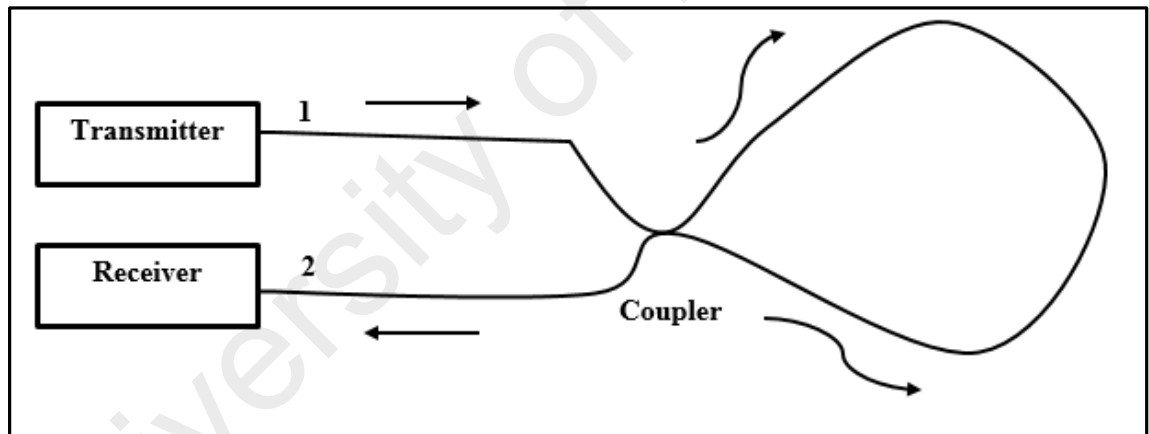


Figure 2.6: Sagnac optical fiber interferometer

Figure 2.7 shows the basic configuration of Michelson Interferometer (MI), comprises of two optical fibers, one transmitter, one receiver and one fiber coupler. Light emitted by the transmitter is divided into two different paths by the coupler, reflected back by mirrors 1 and 2 respectively and then recombined by the coupler into receiver. It is widely used in sensor applications especially for measurements of temperature and RIs of liquid specimens (Lucki et al., 2014) (Yuan, Yang, & Liu, 2008).

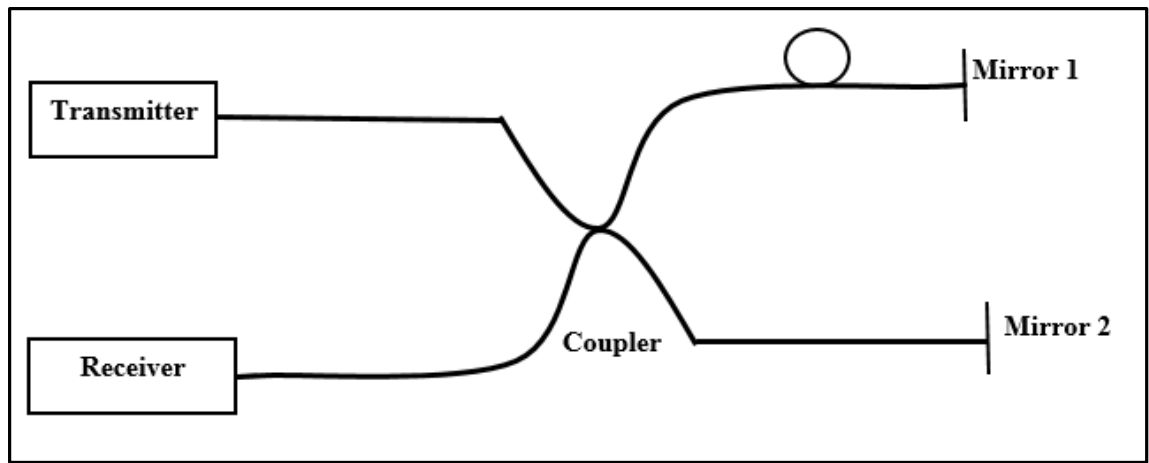


Figure 2.7: Michelson optical fiber interferometer

The simplest structure of a fiber based MZI is depicted in Figure 2.8, which comprises of a laser light source that is being split into two separate beam paths using a 3 dB fiber coupler. 50% of the light beam goes in the optical fiber probe and the remaining 50% enters the reference fiber. The recombination of the two beams is detected and the phase interference is measured. The change in the phase could be attributed to physical change in the path length itself or a change in the refractive index along the path (Hariharan, 2003). If the light waves arrive in phase, they interfere constructively resulting in the strengthening of the intensity. Conversely, a destructive interference (weakening in intensity) occurs if they arrive out of phase (Choi et al., 2007).

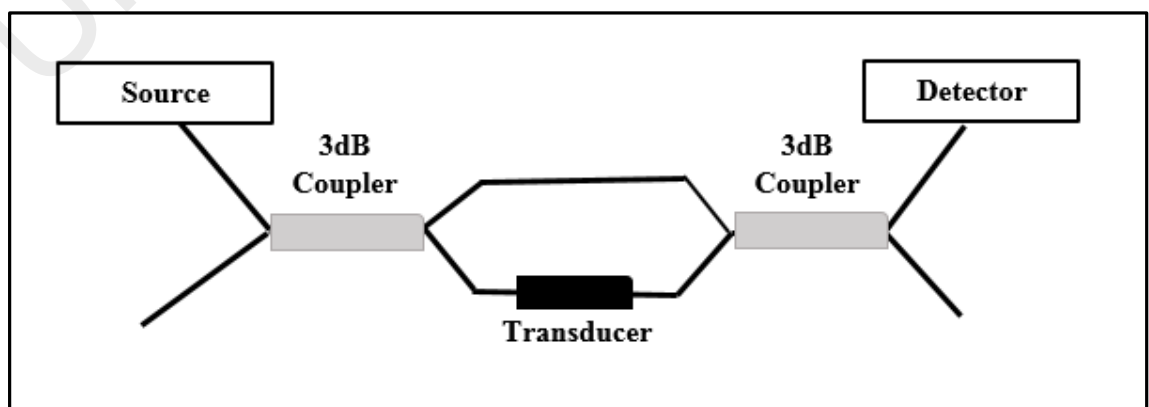


Figure 2.8: Schematic diagram of a Mach-Zehnder interferometer

2.5 Design Consideration of Interferometer for Sensing Application

Phase-modulated or interferometric sensors are one of sensor types that useful for sensor applications due to their high sensitivity (Tian, 2008). Both MZI and the MI have received a tremendous attention in recent years especially in optical fibers sensors applications due to their advantages such as easy to fabricate and high sensitivity. The interference principles of MI are quite similar to the MZI except that MI only requires one fiber structure to use as the splitter and combiner (Lee et al., 2012). MZI can be considered as one of excellent fiber optical interferometers due to their simple structure and widely used for many areas in photonics devices. MZI sensors can be realized by two fiber arm or in-line single fiber structures. In sensor fields, the reference signal stability is needed. For the two-fiber interferometric sensor, extra attention is required to stabilize the reference signal. Though, for the in-line interferometric sensor, since one channel is shielded by the cladding, while the other is shielded by core, the perturbations are common to both channel and thus do not affect the interference. Also, the in-line structure offers several advantages such as easy alignment, compact, high coupling efficiency and high stability. Therefore this thesis will focuses on in-line single fiber structure for sensing application.

2.6 Review on fiber-optic in-line interferometers based sensors

With the advent of optical fiber technology, a considerable level of research has been concentrated on in-line fiber optic interferometers based sensors. A few method have been proposed, including the grating type (Fan, Zhu, Shi, & Rao, 2011), (Allsop, Reeves, Webb, Bennion, & Neal, 2002), (J.-F. Ding, Shao, Yan, & He, 2005), tapered fiber type (D. Wu et al., 2011), (B. Li et al., 2011; Tian & Yam, 2009), fiber peanut-shape structure ((D. Wu, Zhu, Chiang, & Deng, 2012), connector-offset type sensor (Nguyen,

Hwang, Moon, Moon, & Chung, 2008),(E. Li, Wang, & Zhang, 2006) ,etc. Since the inline fiber optic interferometric sensor technologies are made by normal SMFs, it has a relatively low fabrication cost.

2.6.1 Grating type sensor

A fiber Bragg grating (FBG) is a passive optical device based on the refractive index modulation of the optical fiber core and consists of a period in range of hundreds of nanometers, created through the exposure of the fiber optics core to an optical interference pattern of ultraviolet radiation. The FBG structure and its spectral response are illustrated in Fig. 2.9. The operation principle of a FBG is based on the signal reflection in each plane of the periodic structure as shown in Fig. 2.9(a). When the Bragg condition is matched, all the reflected components are in phase and are added, otherwise, the components are out of phase and vanished. Fig. 2.9 (c) shows the spectral response of the FBG, where the central wavelength of the reflected spectrum coincides with the Bragg wavelength, λ_B . The Bragg wavelength is defined as the central wavelength of the reflection mode that satisfies the first order Bragg condition, and it is given by

$$\lambda_B = 2\Lambda n_{eff} \quad (2.4)$$

where Λ is the refractive index modulation period and n_{eff} is the optical fiber core effective refractive index (Srimannarayana et al., 2008). The Bragg wavelength depends both on the n_{eff} and Λ and, therefore, any external disturbance acting on these parameters can be measured by analyzing the Bragg wavelength of the reflected signal.

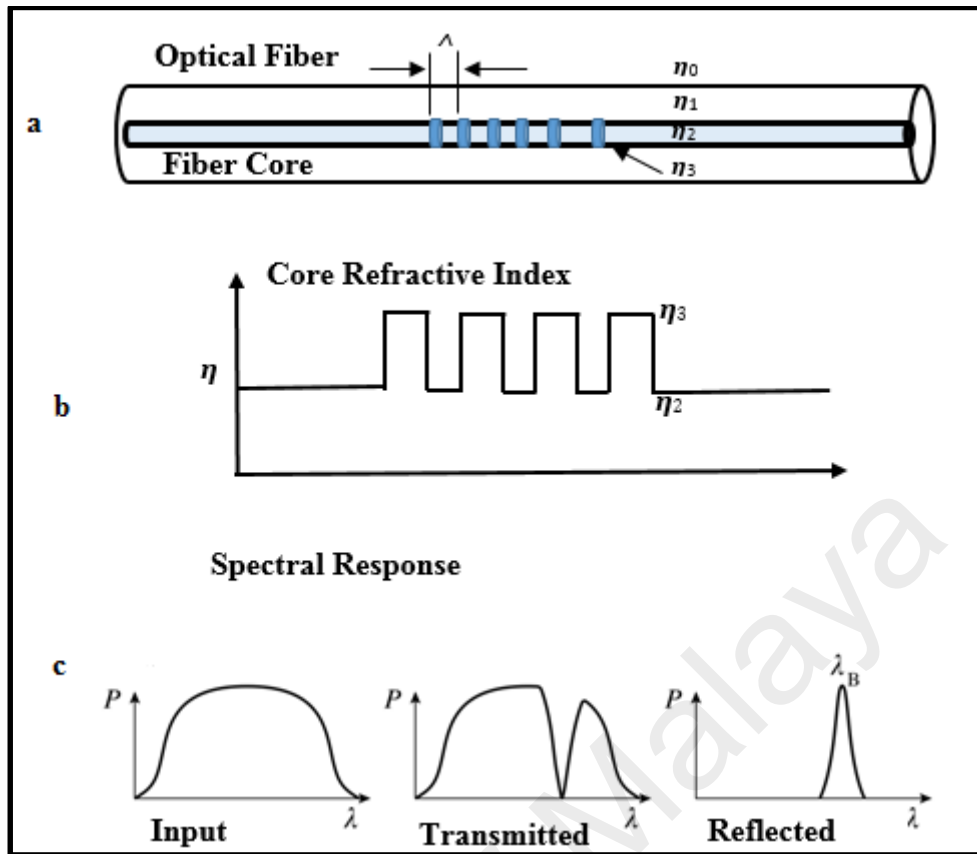


Figure 2.9: FBG (a) periodic structure (b) refractive index modulation inside fiber's core and (c) spectral response

Till today, FBGs have been extensively studied for sensing various physical parameters such as temperature, strain, pressure, acceleration, torsion, flow and others (Balta et al., 2005), (Dawood, Shenoi, & Sahin, 2007; P. Wang, Liu, Li, Chen, & Zhao, 2011) (Müller, Buck, & Koch, 2009). For instance, FBG sensors can monitor deformations and stresses in reinforced concrete elements, and urban infrastructures when they are used in structural monitoring (Ansari, 2005) (Abrate, 2002). The FBGs are also suitable for distributed temperature sensing and they have high detection accuracy, but the temperature sensitivity is usually low. Recently, an etched FBG have also attracted much interest as they exhibit a proportionally large evanescent field that travel along the cladding and can be manipulated for various sensing applications (Zhang, Chen, Zheng, Hu, & Gao, 2013), (Hassan, Bakar, Dambul, & Adikan, 2012).

2.6.2 Tapered fiber based sensor

Tapered optical fibers can be grouped into two categories: adiabatic (small taper angle) and non-adiabatic (abrupt taper angle) which depend on the taper angle. It is obtained by a tapering technique, which involves a process of reducing the fiber's cladding diameter by heating and pulling the fiber ends (Love et al., 1991). If the cladding of the fiber is decreased or removed, the evanescent field will expose to the environment. This characteristic is very useful for sensor applications, where various shapes and properties of tapered fibers are proposed and fabricated for sensor applications. For instance, Lim et al. (Lim et al., 2011) demonstrated the microfiber knot resonator using a tapered fiber for current measurement. In this work, the tapered fiber was fabricated from a standard communication SMF using a flame brushing technique. The fiber tapering rig comprises two fiber holders on the translation stage, a sliding stage, an oxy-butane burner fixed on the sliding stage, two stepper motors and the controller board. The oxygen gas and butane gas from separate gas cylinders are mixed and supplied to the torch tip. During the tapering process, the torch moved back and forth along the uncoated segment as its flame brushes against the exposed core while the fiber is stretched slowly. The moving torch provides a uniform heat to soften the fiber with good uniformity along the exposed section while it is stretched by a high precision stepper motor (LINIX stepping Motor). However, this structure is susceptible to some environmental perturbations and causes adsorption and scattering of light and transmission of microfiber decay over time (L. Ding, Belacel, Ducci, Leo, & Favero, 2010). Other than that a small mechanical strength induced can cause cracks in the glass structure and result to an unrecoverable loss in tapered fibers (Gilberto Brambilla, Xu, & Feng, 2006).

Tapered optical fiber can also be produced by a chemical etching process that uses hydrofluoric (HF) acid as an etchant for silica fiber. This method is simple and cheap. In this technique, optical fiber is dipped in a HF acid solution and the etching starts from the

contact surface between the silica glass and HF. The interaction between silicon dioxide (SiO_2) and HF ions causes the removal of silica glass based on the following chemical reaction;



One disadvantage of this etching technique is that the quality of the fabricated tapered fiber is greatly affected by temperature change, vibrations and turbulences at the liquid interface during the etching process (Friedbacher & Bubert, 2011).

2.6.3 Compact in-line core cladding mode interferometer (CCMI)

Compact in-line fiber optic core cladding mode interferometers (CCMIs) are attracted many research interest in recent years for various chemical, physical, and biological sensing applications. The CCMI involves a mechanism to realize the coupling and re-coupling between the modes of the fiber core and fiber cladding. The core mode is guided by the core-cladding interface of the fiber and the cladding mode is guided by the cladding-ambient interface. Due to the optical phase difference (OPD) between the core and cladding modes, the CCMI could be used to measure various environmental parameters. The typical in-line fiber optic CCMI sensors are Mach Zehnder interferometer (MZI) and Michelson interferometer (MI) (Lee et al., 2012).

In the MZI, there are a splitter to couple part energy of the core mode into the cladding modes and a combiner to recombine the cladding modes into the core. Due to the OPD between cladding modes and core mode, an interference pattern could be achieved from the output side in the case of a flat spectrum input. The output intensity of the MZI is governed by:

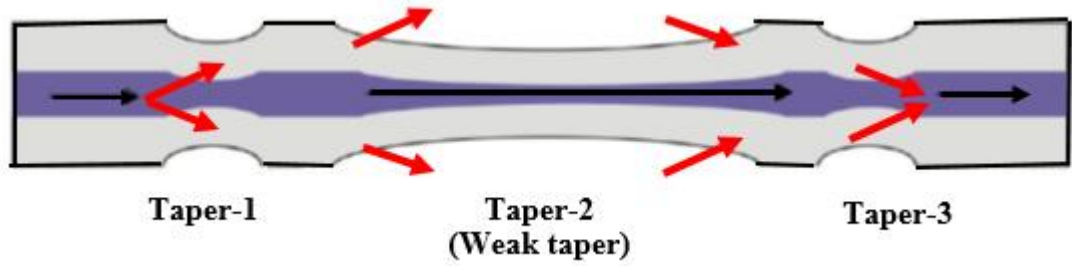
$$I = I_1 + I_2 + 2\sqrt{I_1 I_2} \cos(\varphi) \quad (2.6)$$

where I is the intensity of the interference signal, I_1 and I_2 are the intensity of the light propagating in the fiber core and cladding respectively and φ is the phase difference between the core and cladding modes. It is approximately equal to (Zhu, Wu, Liu, & Duan, 2012):

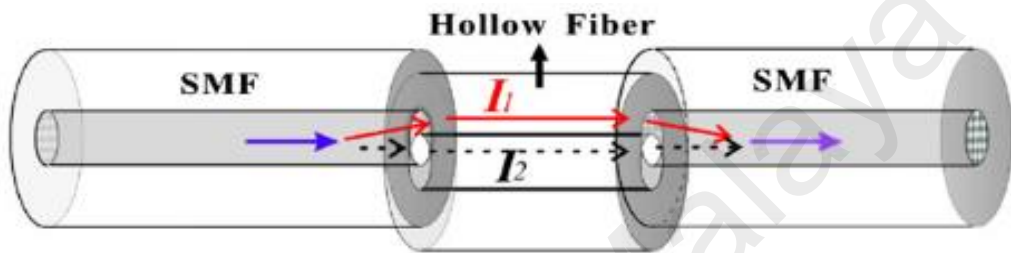
$$\varphi = \left(\frac{2\pi(\Delta n_{eff})L}{\lambda} \right) \quad (2.7)$$

where Δn_{eff} is defined as $(n_c^{eff} - n_{cl}^{eff})$ which is the difference of the effective refractive indices of the core and the cladding modes, L is the length of the interferometer region and λ is the input wavelength. Since the core mode is confined by thick cladding and cladding modes are directly unprotected to environment, Thus, MZIs can be used as refractive index sensors based on the wavelength shift of the interference fringes. For instance, Wu et. al. (D. Wu et al., 2011) proposed and demonstrated a inline MZI based refractive index sensor using a probe based on three cascaded SMF tapers.

Figure 2.10 (a) shows the schematic diagram of the proposed in-line MZI, which consists of three tapers; taper-1, taper-2 and taper-3. In this structure, taper-1 and taper-3 acts as the beam splitters and combiners, respectively to form a MZI. Taper-2 is used to increase the evanescent field of the cladding mode excited by taper-1 in the external medium. As earlier stated, the in-line MZI needed the splitter and combiners in order to separate the input optical signal into two different paths and the recombine them together. The other typical techniques to form the splitter and combiner in SMF include misaligned spliced joint (Duan et al., 2011). Figure 2.10 (b) shows the misaligned splice joined structure which was obtained by using the commercial fusion splicing machine.



(a) Three tapers structure
(Wu et al., 2012)



(b) Misaligned spliced joint structure
(Duan et al., 2011)

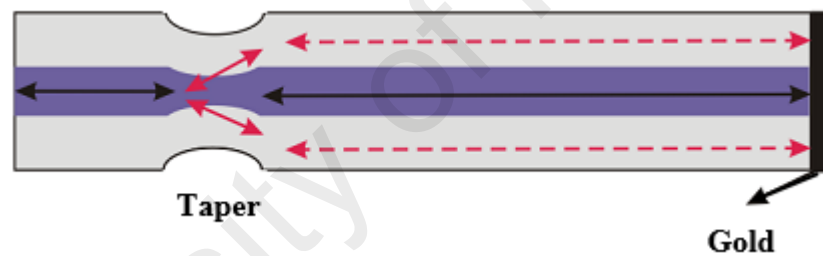
Figure 2.10: The in-line MZI structures based on (a) three tapers and (b) misaligned spliced joint

Fiber-optic sensors based on MIs are quite similar to MZIs. The main difference between MI and MZI are that the MI only requires one fiber structure to act as the splitter and combiner and the existence of a reflector in MI configuration. Indeed, an MI is like a half of an MZI in arrangement. Therefore, the fabrication method and the operation principle of MIs are almost similar as MZIs. Since the optical signal propagates along the interference arms twice, the relative phase difference between core mode and cladding mode could be explained as:

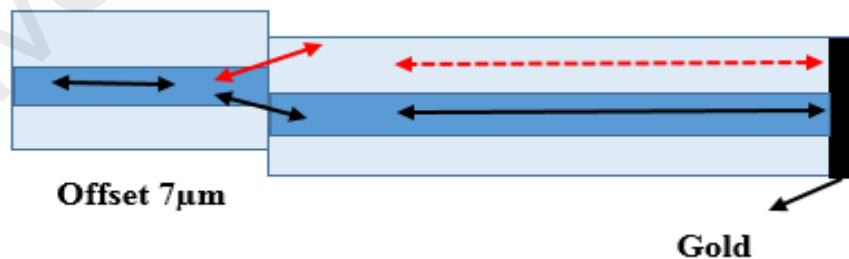
$$\phi_{MZI}^m = \frac{4\pi\Delta\eta_{eff}^m L}{\lambda} \quad (2.8)$$

where $\Delta\eta_{eff}^m$ is the effective RI difference between the core mode and the m th cladding mode, L is the interaction length, and λ is the input wavelength.

Various configurations of in-line MI have been reported. Li et al (E. Li et al., 2006) demonstrated an in-line MI based temperature sensor by simply splicing a section of multimode fiber (MMF) to SMF as sensor probe. Then, Yuen et al (Yuan et al., 2008) have proposed an in-line MI which consists of a section of two core fibers and SMF for flow velocity sensor. Meanwhile, the in-line MIs based on air-holes collapsing of PCF have been reported by Fernando et al for hydrostatic pressure sensing (Fávero et al., 2010). However, these inline MI require special fiber that makes it expensive to use in mass production. In contrast, the other ways to achieve the low cost in line MIs in SMF include LPG (Kim, Zhang, Cooper, & Wang, 2005), fiber taper (Tian, Yam, & Loock, 2008) and core offset structure (Lu, Men, Sooley, & Chen, 2009). Figure 2.11 shows two in-line MIs fabricated using SMF based on fiber taper and core-offset structures.



(a) Fiber Taper
(Tian, Yam, & Loock, 2008)



(b) Core offset
(Lu et. al. 2009)

Figure 2.11: Schematic diagram of two in-line MIs based on (a) the fiber taper and (b) the core offset structure

2.7 Review on sensor coating sensitive material

An optical fiber is coated with a special material, other than a protective buffer to create a fiber that is sensitive to various stimuli such as magnetic fields, pressure, thermal gradients, electric field, electric currents and bending forces. This coating also provides additional protection against detrimental environmental effects and useful for various applications. The combination of fiber optics with sensitive material as such thin film and nanostructures offers a great potential for the realization of novel sensor concepts. This sensitive material functions as a transducer to get response and feedback from environments, in which optical fibers are employed to work as signal carrier. This section reviews on fiber-optic sensors with nanostructure coatings.

In general, nanotechnology can be understood as a technology of design, fabrication and applications of nanostructures. Nanotechnology also includes fundamental understanding of physical properties and phenomena of nanomaterial and nanostructures. Study on the fundamentals relationships between physical properties, phenomena and material dimensions in the nanometer scale, is also referred to as nanoscience. Nanotechnology is a technology that involves with small structures or small sized materials. The typical dimension spans from sub-nanometer to several hundred nanometers. A nanometer (nm) is one billionth of a meter or 10^{-9} . One nanometer is approximately the length equivalent to ten hydrogen or five silicon atoms aligned in a line. Materials in the micrometer scale mostly exhibit physical properties the same as that of bulk form. However materials in the nanometer scale may exhibit physical properties distinctively different from that of bulk. Suitable control of the properties of nanometer-scale structures can lead to new science as well as a new devices and technologies.

There has been an explosive growth of nanoscience and technology in the last few years, primarily because of the availability of new strategies for the synthesis of nanomaterial and new tools for characterization and manipulation. Several method of

synthesizing nanoparticles, nanowires and tubes, and their assemblies have been discovered. On the other side, wide variety of nanostructures such as nanowires, nanotubes and nonporous material have also attracted great interest to researchers due to its unique advantages (Arregui, 2009). Nanostructured materials are a new class of materials which provide one of the greatest potentials for improving performance and extended capabilities of products in a number of industrial sectors, including the aerospace, tooling, automotive, recording, cosmetics, electric motor, duplication, and refrigeration industries.

2.7.1 Carbon Nanotubes

Recently much effort has been devoted to developing sensitive materials to construct optical fiber based sensors. The discovery of carbon nanotubes (CNTs) (Iijima, 1991) has generated great interest among researchers to develop high performance devices. Carbon is a unique material and can be good metallic conductor in the form of graphite, a wide bandgap semiconductor in the form of diamond or a polymer when reacted with hydrogen. The ongoing exploration on electrical, physical, chemical and mechanical properties contributes a wide range of applications such as nano-electronics, sensors, field emission and electrodes. The electrical properties of CNTs are extremely sensitive to charge transfer and chemical doping effects by various molecules. There are two classes of CNTs as shown in Figure 2.12: single walled nanotubes (SWNTs) and multi-walled nanotubes (MWNTs) (Scarselli, Castrucci, & De Crescenzi, 2012). SWNTs have only one layer of graphene cylinder, while MWNTs have many layers. Although SWNTs are structurally similar to a single layer of graphite, they can be either metallic or semiconducting depending on the tube diameter and the chirality. In general three techniques are used for synthesizing CNTs: (i) carbon arc-discharge technique; (ii) laser-ablation technique; and (iii) chemical vapor deposition (CVD) technique.

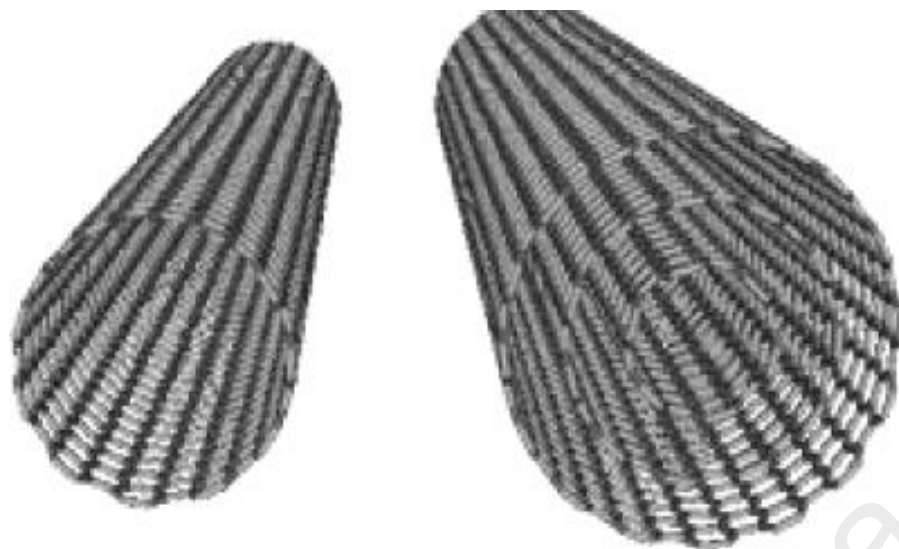


Figure 2.12: Single walled nanotubes (SWNTs) and multi-walled nanotubes (MWNTs) (Scarselli, Castrucci, & De Crescenzi, 2012).

Lately, the potential of CNTs as sensing elements and tools for biomolecular analysis as well as sensors for gases and small molecules have been demonstrated (J. Li et al., 2003). CNTs integrated with biological functionalities are expected to have great potential in biomedical applications due to their unique one-dimensional quantum wires with high surface-to volume ratio. Their electronics properties are very sensitive to molecular adsorption and it is expected that the CNTs sensing elements will be affected if coupled with biomolecules which is high ions carrier (J. Li et al., 2003; Star, Gabriel, Bradley, & Grüner, 2003). To date, CNTs have been utilized in biosensors in many forms such as probes (Vo-Dinh, Alarie, Cullum, & Griffin, 2000; Woolley, Guillemette, Cheung, Housman, & Lieber, 2000), field-effect-transistor using a single semiconducting CNTs (Bradley, Cumings, Star, Gabriel, & Grüner, 2003), a random CNT network (Koehne et al., 2003) and nano-electrode array (Azamian, Davis, Coleman, Bagshaw, & Green, 2002; Guiseppi-Elie, Lei, & Baughman, 2002)

Recently, Batumalay et. al. (Malathy Batumalay et al., 2014) also proposed tapered plastic optical fiber (POF) coated with SWNT polyethylene oxide composite for measurement of different concentrations of uric acid in de-ionized water. The tapered

POF was fabricated by etching method using acetone, sand paper and de-ionized water to achieve a waist diameter of 0.45 mm and tapering length of 10 mm. The measurement is based on intensity modulation technique where the output voltage of the transmitted light is investigated for different uric acid concentration. Results shows that SWCNT-PEO coated fiber enable to increase the sensitivity of the fiber-optic sensor.

2.7.2 Zink Oxide Nanostructures

The innovation of Zink Oxide (ZnO) nanostructures in 2001 (Gusatti et al., 2011) has swiftly expanded because of their unique and novel applications in nano-electronics, sensors, field emission and electrodes. These nanostructures attracted great interest to researchers due to its unique advantages in combination with immobilized enzymes and can enhance the direct electron transfer between the enzyme's active sites and the electrons (Ali, Ibupoto, Kashif, Hashim, & Willander, 2012). ZnO is representative of II–VI semiconductor compounds, is a very versatile and important material. It has a unique position among semiconducting oxides due to its piezoelectric and transparent conducting properties. ZnO has a wide band gap (3.37 eV) and a large exciton binding energy (60 meV) (Chen et al., 2012). A wide band gap has many benefits like enabling high temperature and power operations, reducing electronic noise, making sustenance in large electric fields possible and raising breakdown voltages. Recently, various synthesis techniques have been developed to fabricate ZnO nanocrystals with different shapes, which include metal-catalyzed vapour-liquid-solid (VLS) growth, physical vapour deposition (PVD), chemical vapour deposition (CVD), metal-organic vapour-phase epitaxy, metal-organic CVD, template-assisted growth and oxidation method (Arregui, 2009; Subramanyam, Srinivasulu Naidu, & Uthanna, 2000; Yawong, Choopun, Mangkorntong, Mangkorntong, & Chiang, 2005). Many of these techniques however are complicated needing a high temperature for synthesis and also have a long reaction time.

Apart from this, these techniques also utilize toxic components and require expensive experimental setup.

The oxidation method on the other hand is a simple low-cost technique and very commonly used for the synthesis of ZnO nanostructures. ZnO nanostructures have been successfully synthesized by oxidizing Zn foils at 700°C in air without the presence of a catalyst and carrier gas (Kissinger, 1957). Sekar and co-workers (Sekar, Kim, Umar, & Hahn, 2005) reported that ZnO nanowires were grown on Si (100) substrates by oxidation of metallic Zn powder at 600°C. As shown in Figure 2.13, the synthesized ZnO materials have been found to have rod like, belt like, wire like and needle like morphologies. This method for synthesis of ZnO is economical as it uses the oxygen from the air (Liu, Jian-er, Larbot, & Persin, 2007; Viswanathan & Gupta, 2003; Yao et al., 2007). In this thesis, an economical and environment friendly route has been used for the synthesis of ZnO by using a sol-gel immersion method.

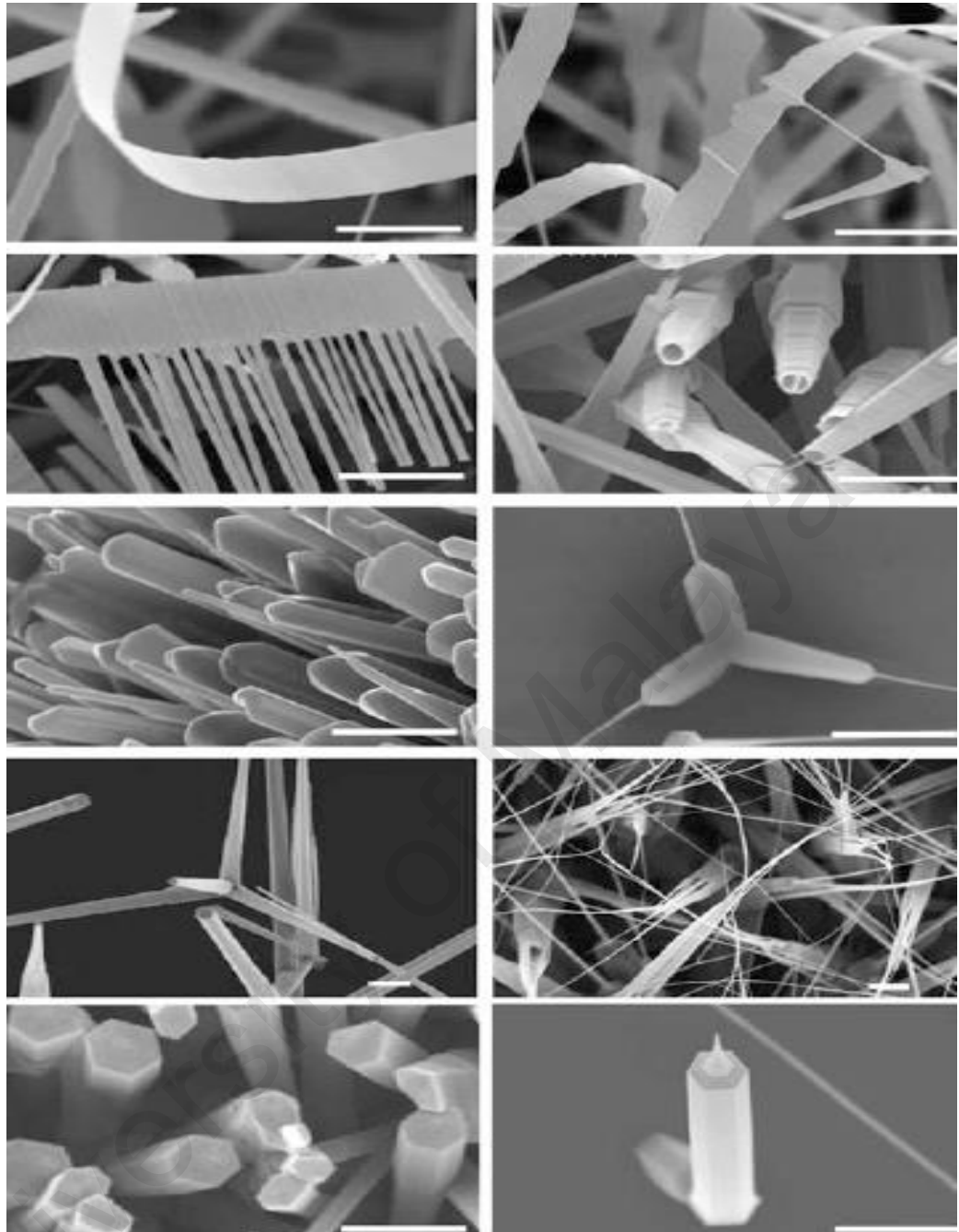


Figure 2.13: ZnO nanostructures in various morphologies

(Arregui, 2009)

Up to date, various fiber-optic sensors are proposed and demonstrated based on ZnO nanostructures. For instance, Batumalay et. al. (2014) used a tapered POF coated with ZnO nanostructures for measurement of different concentrations of uric acid in de-ionized water and changes in relative humidity (RH) (M Batumalay et al., 2014) (M Batumalay et al., 2014) (M Batumalay et al., 2014) (M Batumalay et al., 2014).The

experimental results show that tapered POF with seeded ZnO nanostructures increases the sensitivity of sensor for uric acid detection as well as RH.

2.7.3 Thin film coating

Thin films are two-dimensional nanostructures by definition. Generally, they are used to reduce the (surface) properties of a bulk material in those cases where a change of the bulk properties is too expensive or simply impossible to achieve for physical or chemical reasons. In addition, combinations of thin films may serve to achieve complex combinations of surface properties. For instance, Silva et. al. (Silva, Rocha-Santos, & Duarte, 2008) proposed a fluorosiloxane polymer coated optical fiber sensor for detection of volatile organic compounds (VOCs). Fluorosiloxane polymers constitute an interesting class of polymers for coating the optical fibre sensor because of their useful and versatile properties: high thermostability, hydrophobicity, lipophobicity, hydrolytic stability, high chemical inertness and low dielectric constant (Bergström & Hilbert, 2005). Besides their chemical and thermal stability the polymers also have a low glass temperature, which is an interesting property when absorption and diffusion phenomena are concerned (Demathieu, Chehimi, & Lipskier, 2000). Hence they have many applications in shielding coatings, biotechnology, aeronautics (Ameduri & Boutevin, 2005) and optical sensing. Abdelghani et. al. (1997) demonstrated optical fibre sensor coated with porous silica layers for gas and chemical vapour detection (Abdelghani, Chovelon, Jaffrezic-Renault, Veilla, & Gagnaire, 1997). In this work, a thin polymeric film was deposited on the cleaved optical fiber end by dip-coating method. The optical fiber was then cured at 1 hour. The sensing principle is based on fact that the energy of the light guided through the optical fiber depends upon the variance between the refractive index of the core and the cladding of the optical fiber. When, the analyte absorbs into the specific porous silica cladding, its refractive index changes, thus leading

to a variation of the light power. These variations are proportional to the amount of analyte absorbed on the sensitive surface.

In other work, Muto et al. (Muto et al., 2003) demonstrated humidity sensors which are based on reversible absorption of water (H_2O) from the ambient atmosphere into a porous thin-film interferometer that sits on the tapered fiber. The water absorbed changes the refractive index of the thin films and subsequently transforms the lossy fiber into a light guide. Corres et al. demonstrated a similar humidity sensor based on nanostructured films, which were deposited onto tapered fibers using the ionic self-assembled monolayer (ISAM) deposition technique (Jesús M Corres, Arregui, & Matías, 2007). In other scheme, simple humidity sensor is proposed and demonstrated using a POF based on intensity modulation technique coated with a polymer blend of hydroxyethylcellulose/ polyvinylidene fluoride (HEC/PVDF) composite that acts as the humidity sensitive cladding (Batumalay et al., 2013). The humidity sensitive layer of the composite has an RI value which is higher than that of the core in dry state. This condition creates a lossy waveguide and as the cladding layer hydrates, the RI value falls below that of the core and increases the intensity of light propagating through the core. The results show that the HEC/PVDF coated fiber responds to variation in humidity by changing its conductance.

2.8 Summary

Thorough literature reviews on optical fiber basic, fiber sensors, interferometers and sensor coating sensitive materials have been discussed in this chapter. At first, some basic principle on optical fiber and recent development on fiber-optic sensors were given. Then, the background of optical fiber based interferometer is described that includes Fabry-Perot, Sagnac, Michelson and Mach Zender structures. This chapter also presented the background of in-line fiber optic interferometers sensors by providing the some literature review and working principle. Finally this chapter introduces various sensitive materials and explains its role in improving the sensitivity of sensor.

University of Malaya

CHAPTER 3: DEVELOPMENT OF EVANESCENT WAVE BASED FIBER SENSORS FOR RELATIVE HUMIDITY MEASUREMENT

3.1 Introduction

The developments of novel optical fiber structures have become the central focus of optical fiber researches in recent years. For instance, tapered optical fibers and inline Mach Zehnder interferometers are proposed for various applications in microscale and nanoscale photonic devices (Lim et al., 2011; Tian, Yam, Barnes, et al., 2008). The new optical fiber structures have found many applications in the fields of biochemical, biomedical, environmental and other areas. In a nutshell, these structures enhance the interaction between the evanescent fields in the probes and their surrounding environments. Furthermore, the optical fiber structures can guide light at both visible and infrared wavelength regions with low loss (H. Rahman et al., 2011).

The monitoring of humidity is crucial for numerous industrial applications, where humidity may affect the quality of products and health of workers like in many chemical and biomedical industries. Humidity sensors are also frequently used to monitor big structures such as bridges or planes so that possible risk of leakage due to corrosion can be predicted (Sun et al., 2009). Therefore relative humidity measurement has been extensively studied and a great variety of sensors, including capacitive, resistive, thermal conductivity and optical have been developed for this purpose in the last decades. So far, electronic humidity sensors control the bulk of the market because their technology of fabrication is well established. However, the field of optical fiber sensors has grown enormously since the 60's and at the present there exist niche applications where optical

fiber humidity sensor technology can advantageously compete with its electronics counterpart.

Fiber optic humidity sensors (FOHS) use optical fiber technology to guide a light signal which is modulated by the ambient humidity and then collected back by a detector, conditioned and processed. Thanks to the low attenuation and large wideband operating range of the fiber, it is possible to transmit large sensor data quantities over kilometer distances. In addition, the use of several interrogating techniques enable the existence of distributed humidity sensors configurations (Q. Wu et al., 2011) . There are also a high number of applications where the possible electric hazard produced by the electronic sensor itself or the electromagnetic interferences of the surrounding environment render the use of electronic humidity sensors unfeasible. In some fields, humidity must be measured in areas where space is tight and accessibility is limited. The small dimensions and simple geometries of optical fiber enable them to be implemented in light-weight systems and employed in such challenging conditions such as embedded into construction materials.

To date, a wide range of relative humidity (RH) sensing techniques based on optical fibers have been reported including the ones using long period gratings (Del Villar et al., 2010), fiber Bragg gratings (FBGs) (Miao et al., 2009), side polished fibers (Alvarez-Herrero et al., 2004), plastic optical fibers (Muto et al., 2003), and surface plasmon resonance (Qi et al., 2006). In this chapter, tapered fibers and FBG are used to develop evanescent-wave based fiber sensors for relative humidity (RH) measurement. Two main sensing approaches; intensity modulation and interferometric technique are also examined in this work.

3.2 Development of sensitive material for humidity

In earlier works, a variety of sensing materials, such as polyimide, crystal violet, porous silica xerogel (Jesús M Corres et al., 2007), agarose, and a variety of methyl polymers that have been used for RH measurement. For instance, Bariain et. al. (Bariain, Matías, Arregui, & Lopez-Amo, 2000) proposed and demonstrated an optical fiber humidity sensor based on a tapered fiber coated with agarose gel. The agarose gel is a material that is commonly used for biological research applications (Doliba, Wehrli, Babsky, Doliba, & Osbakken, 1998; Kurihara et al., 1998). It is considered a biopolymer, which is produced from marine algae (*Gracilaria verrucosa*). Normally, it is in the form of white powder which is soluble in water at 34–38°C. It gels to form double propeller structure, which join to form a three-dimensional net (Clark & Ross-Murphy, 1987) and (Iglesias, Garcia, Roques, & Bueno, 1993). The obtained gel is insoluble in water and can be easily deposited on the fiber. Its porosity determines the quantity of water that the gel is capable of absorbing and therefore, it operates very well as a sensitive material for humidity sensor.

In another work, Estalla et al. (Estalla, de Vicente, Echeverría, & Garrido, 2010) demonstrated a fiber optic humidity sensor based on a porous silica xerogel film as the sensing element. This film was synthesised by the sol–gel process and fixed onto the end of the optical fiber by dip-coating technique. This intrinsic sensor works in reflection mode, and the transduction takes place in the light that travels through the core of the fiber. In our work, we introduce a new sensitive material by combining hydroxyethyl cellulose (HEC) and polyvinylidene fluoride (PVDF). In this section, the preparation of the HEC/PVDF composite is explained in detail.

Figure 3.1 shows the step by step procedure to prepare the HEC/PVDF mixture. Firstly, 1g of PVDF powder ($M_w = 275,000$) is dissolved in 120 ml dimethyl sulfoxide (DMSO) and 100ml distilled water at 90°C in water bath. Then the solution of PVDF is cooled down to room temperature and 4 g of HEC is added to the solution. The mixed solution is continuously stirred at room temperature for about 10 hours in order to generate a three-dimensional structure of the mesh gel (hydrogel). DMSO is used in the preparation of the HEC/PVDF as solvent since HEC is only soluble in water while PVDF isn't. Figure 3.2 shows a sample of the polymer composite solution, which is obtained by blending HEC and PVDF and its microscopic image (Batumalay et al., 2013). The mixture turns into a gel-like material after a long period of agitation, and finally stabilizes and forms a three-dimensional mesh structure after being coated onto the sensor probe. The mesh gel has a good absorption of water in the air. Then, this material is slowly dropped onto the various sensor probes using syringe and the sensor performance will be investigated in this chapter.

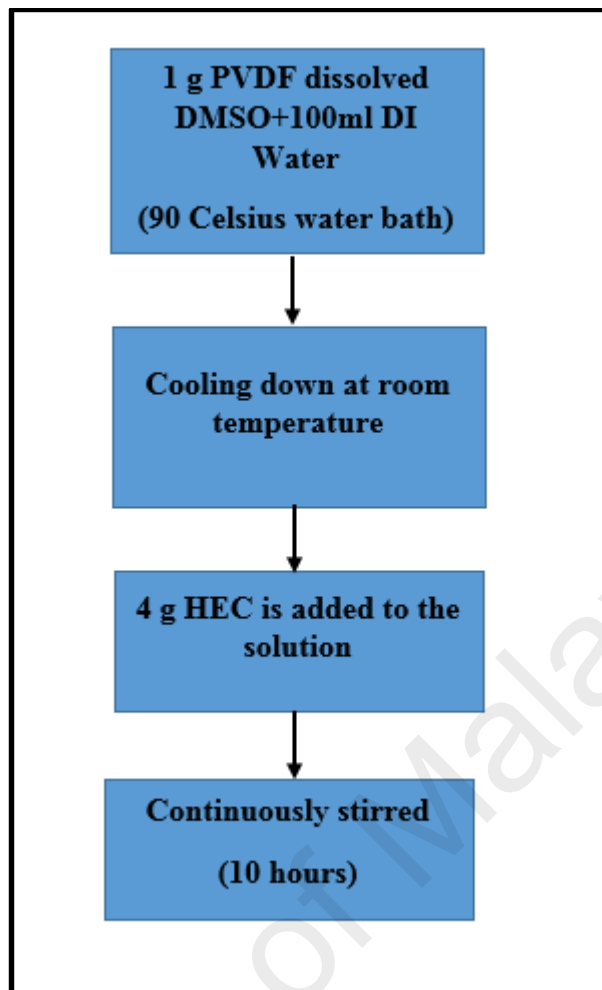


Figure 3.1: procedure to prepare the HEC/PVDF mixture



Figure 3.2: The polymer composite solution and its microscopic image

3.3 FOHS based on intensity modulation technique

Tapered optical fibers exhibit significant evanescent field that travel along the cladding and can be manipulated for various sensing applications, (Muhammad, Jasim, Ahmad, Arof, & Harun, 2013; H. Rahman et al., 2011). Recently, many evanescent wave-based sensors have been proposed and demonstrated for humidity measurement. For instance, Muto et al. demonstrated humidity sensors which were based on reversible absorption of water (H₂O) from the ambient atmosphere into a porous thin-film interferometer that sits on the tapered fiber (Muto et al., 2003). The water absorbed from the ambience changed the refractive index of the thin films and subsequently transformed the lossy fiber into a light guide. Humidity sensing was also demonstrated using a tapered fibre with agarose gel (Bariain et al., 2000). In this section, we present an innovative RH sensor based on tapered fiber coated with a polymer blend of HEC/PVDF composite. The composite coating changes its optical properties in response to the RH change of its surrounding. The measurement is based on intensity modulation technique where the output power of the transmitted light is linked with changes in RH.

3.3.1 Preparation of the sensor probe and experimental setup

A tapered fiber was prepared from a standard communication single-mode fiber (SMF) using a flame brushing technique. Figure 3.3 shows the fiber tapering rig assembled in the laboratory, which is used to fabricate the sensor probe. The rig comprises two fiber holders on the translation stage, a sliding stage, an oxy-butane burner fixed on the sliding stage, two stepper motors and the controller board. The oxygen gas and butane gas from separate gas cylinders are mixed and supplied to the torch tip. The SMF used in this experiment has a core and cladding diameters of 8.3 and 125 μm , respectively. The coating of a short section of the fiber (about several cm in length) is removed and the bare

fiber is then stretched on fiber holders for the tapering process. The fiber is pulled only from one side by a controllable motor. During the tapering, the torch moved back and forth along the uncoated segment as its flame brushes against the exposed core while the fiber is stretched slowly. The moving torch provides a uniform heat to soften the fiber with good uniformity along the exposed section while it is stretched by a high precision stepper motor (LINIX stepping Motor). After the tapering process, the fiber is held straight by the translation stages so that the sensing material could be deposited onto the tapered section.

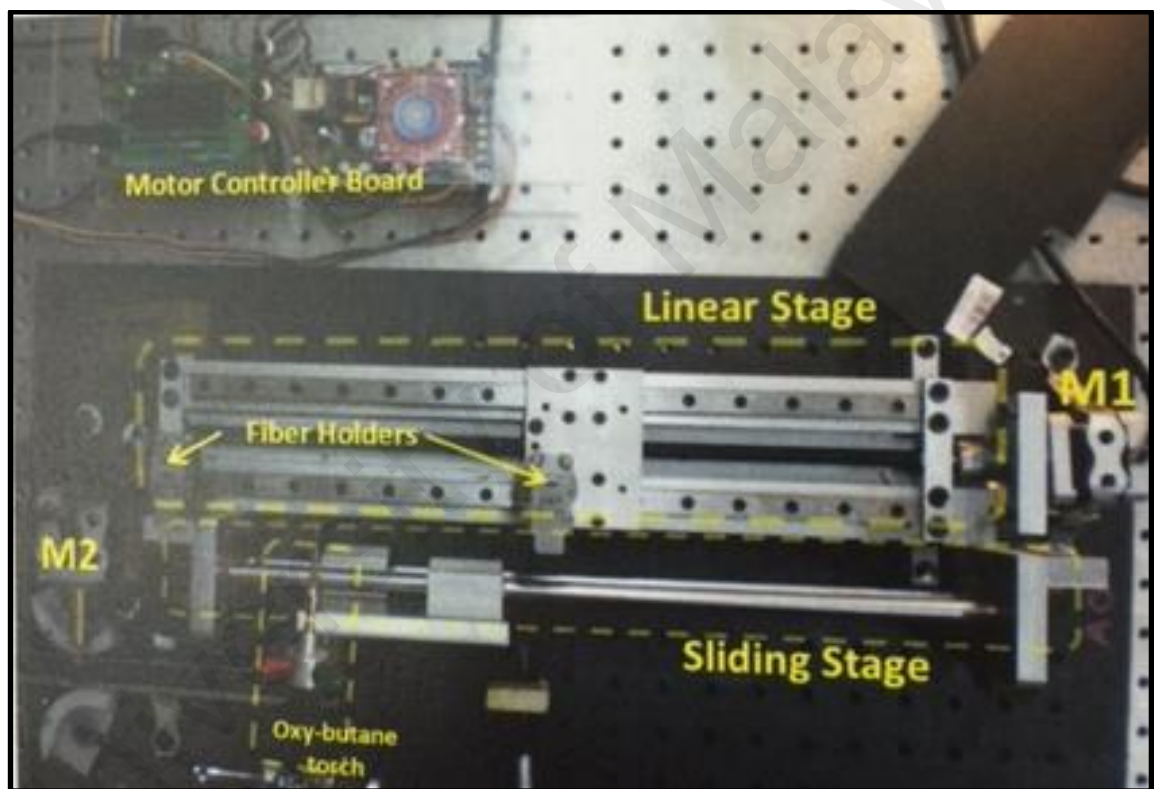


Figure 3.3: Fiber tapering rig used in this study

Here, we choose a combination of HEC and PVDF, as the sensing materials because they are relatively common and inexpensive. The prepared HEC/PVDF composite solution is slowly dropped onto the tapered fiber using syringe and left to dry for 48 hours. Figures 3.4 (a) and (b) show the microscopic images of the tapered fiber with and without the HEC/PVDF composite. The tapered fiber has a waist diameter of

around $5 \mu\text{m}$ as shown in Figure 3.4 (a). The tapered fiber coated with HEC/PVDF (Figure 3.4 (b)) is then used as a sensor probe in the RH sensing experiments.

Figure 3.5 shows the experimental setup for the proposed sensor to detect change in RH using the tapered fiber coated with HEC/PVDF composite. The input and output ports of the tapered fiber are connected to amplified spontaneous emission (ASE) laser source, and optical spectrum analyzer (OSA), respectively. The sensor probe is placed in a sealed chamber with a dish filled with saturated salt solution. Exposing the HEC/PVDF composite to the RH changes inside the chamber produces variations in the output optical power. In the experiment, the performance of the proposed sensor is investigated for various changes in RH ranging from 50 to 80% using 1365 data logging humidity temperature meter.

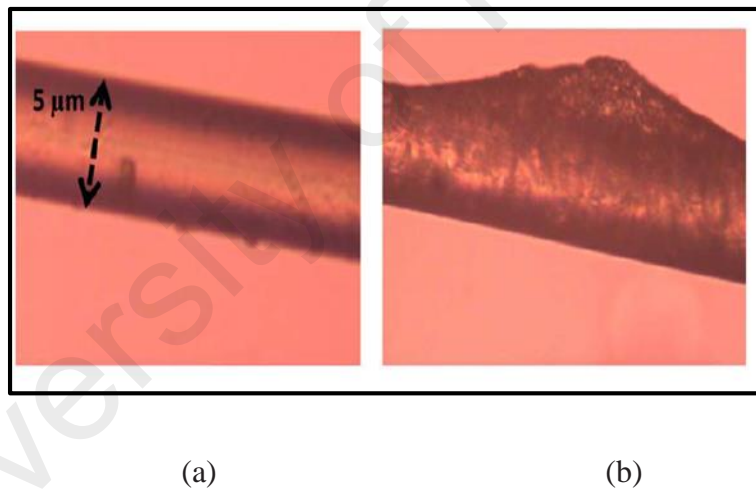


Figure 3.4: Microscopic images of the tapered fiber (a) without and (b) with the HEC/PVDF composite coating

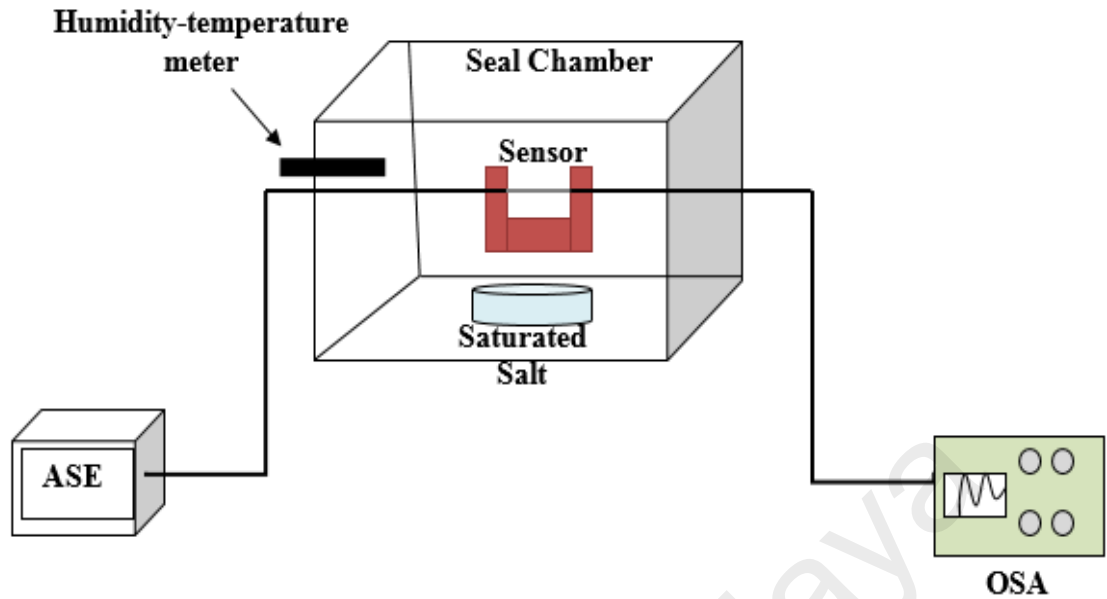


Figure 3.5: Experimental setup for the proposed sensor to detect change in RH using the tapered fiber coated with HEC/PVDF composite. Abbreviation ‘ASE’ means an amplified spontaneous emission and ‘OSA’ an optical spectrum analyzer.

3.3.2 Performance of the FOHS based on intensity modulation

Figure 3.6 shows the output spectra of the transmitted light from the tapered fiber with and without HEC/PVDF composite coating. As shown in the figure, the transmitted light intensity drops by around 9 dB at 1550 nm after the tapered fiber is coated with the composite. This is attributed to the change in the refractive index of the inner cladding layer, which increases from 1 to around 1.492 as the surrounding material changes from air to the humidity-sensitive HEC/PVDF composite. This suggests that the propagating light inside the tapered fiber leaks out from the core at some areas where the composite layer is thick. At these areas, the effective refractive index of the cladding is slightly higher than that of the core. This causes the tapered fiber to become a lossy waveguide and reduces the intensity of the light propagating through the tapered fiber (Morisawa, Amemiya, Kohzu, Liang, & Muto, 2001).

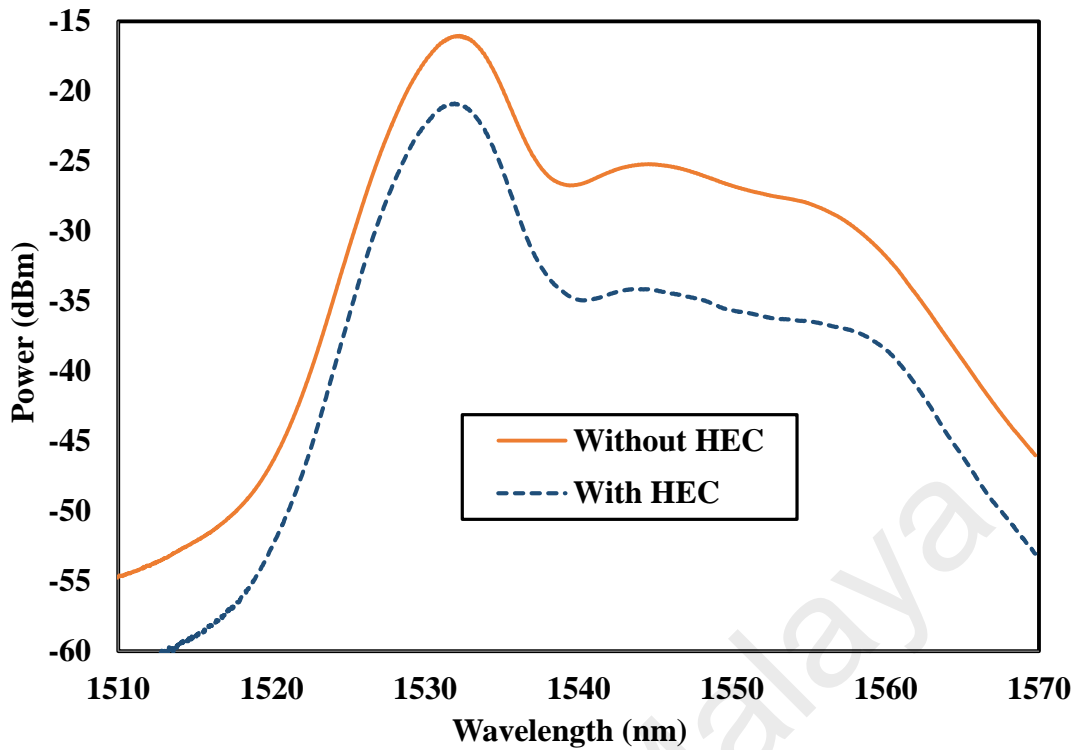


Figure 3.6: The output spectra of the transmitted light from the tapered fiber with and without HEC/PVDF composite coating.

The behavior of the proposed tapered fiber sensor against RH is investigated with and without the HEC/PVDF composite coating. At first, the results are fitted with a linear trend where the coefficient of determination is above 0.95 for both cases with and without HEC/PVDF coating as shown in Figure 3.7. The coefficient represents the goodness of fit such that a high value signifies a good fitting of the model. As seen in Figure 3.7, the intensity of the transmitted light from the tapered fiber increases with the increment of RH for both cases. It is found that the sensitivity of the sensor improves from 0.009 to 0.030 dB / %RH as the HEC/PVDF coating is applied on the sensor probe.

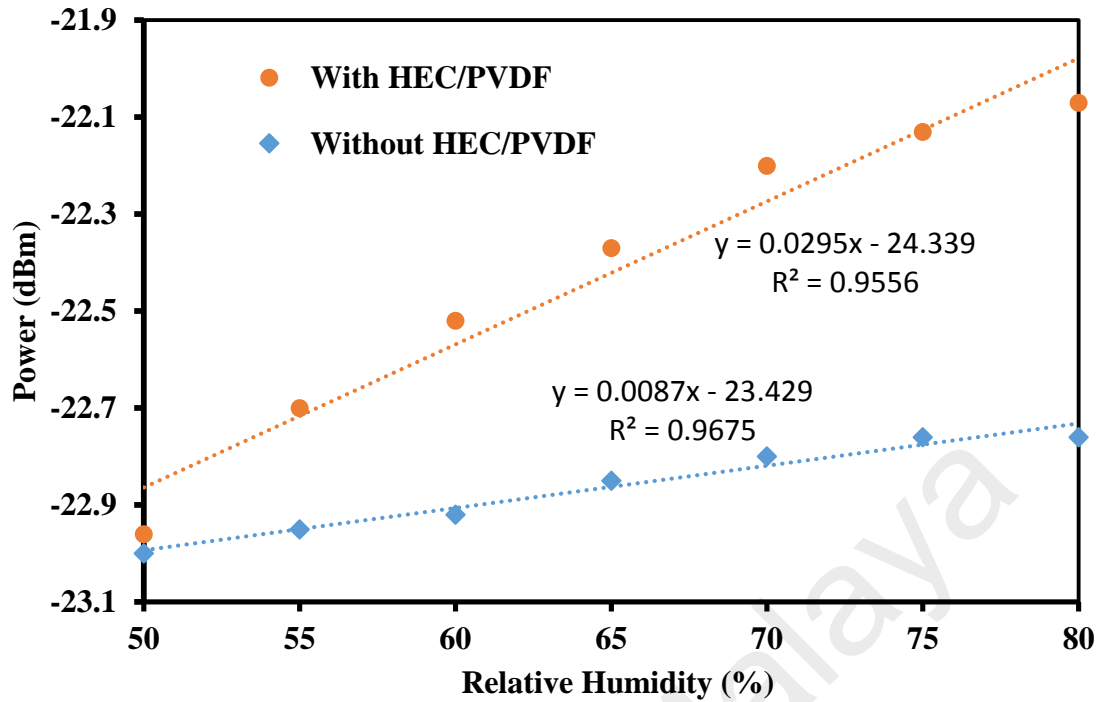


Figure 3.7: Output power versus relative humidity with linear fitting

Figure 3.8 also shows the variation of the transmitted light intensity through the tapered fiber against the RH. Without the HEC/PVDF layer, an output power dynamic range of 0.24 dB is obtained for 50 to 80% RH variation. The sensitivity of the sensor significantly increases when the tapered fiber is coated with the HEC/PVDF composite. It is also observed that the intensity of the transmitted light of the coated tapered fiber leaps in a quadratic fashion to the increase of the RH from 50 to 80%. For instance, the intensity of the transmitted light increases by 0.89 dB as the RH is increased from 50 to 80 % as shown in Figure 3.8. The adjusted R-square value or the coefficient of the determination which corresponds to the measure of the goodness of fit is 0.9982, which is slightly higher than the linear fitting.

In dry state, the humidity sensitive composite layer has an RI value which is higher than that of the core and thus it acts as a lossy waveguide. As the cladding layer

hydrates, the RI value falls below that of the core and thereby increases the intensity of propagating light. These results show that the proposed sensor is applicable for relative humidity sensing. However, the structures are susceptible to the air turbulence and the pollution of dust and moisture when exposed to air. The dust or moisture on the fiber taper may introduce loss to the transmission. Also, a small mechanical strength induced can cause cracked in the glass structure and results in an unrecoverable loss in the tapered fiber.

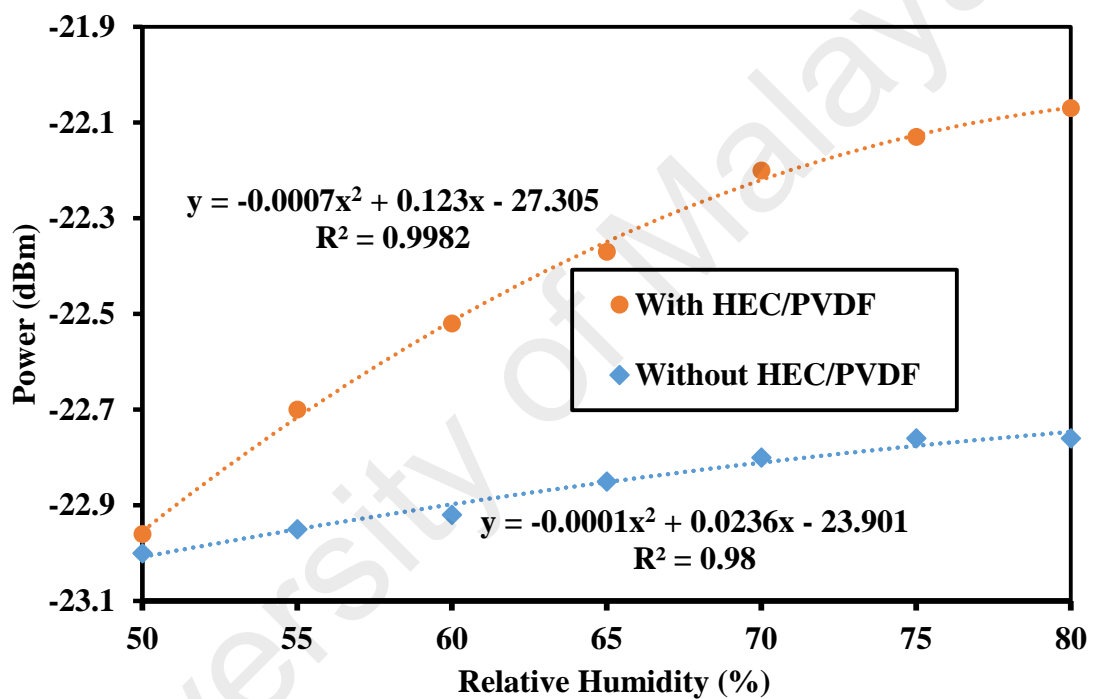


Figure 3.8: The output power versus relative humidity with a quadratic fitting trend

These results show that the proposed sensor is applicable for RH sensing and also has the ability to provide real time measurement. To be useful for industrial applications, a low cost light source and detector such as laser diode and a photodiode can be used and no other special requirements for light and detectors are necessary because this is an intensity-based sensor. In the next section, the interferometric technique is introduced for RH sensor using the same sensitive material based on HEC/PVDF composite.

3.4 FOHS based on interferometric technique

Earlier a humidity sensor that employs a tapered fiber coated with a mixture of HEC/PVDF polymer has been demonstrated based on the intensity modulation technique. Notice that this technique requires periodic recalibration to maintain the accuracy. In this section, we propose and investigate a new FOHS based on a wavelength shift occurring in a non-adiabatic tapered SMF coated with the HEC/PVDF composite. The composite coating changes its optical properties in response to the changes of the relative humidity of its surrounding. Here, the non-adiabatic tapered fiber is prepared using a chemical etching technique instead of flame brushing technique. The effect of tapered fiber diameters on the performance of the sensor is demonstrated. The performance of the sensor is also investigated for two different sensing configurations.

Up to date, various fabrication techniques have been developed for preparing tapered fiber. One of these techniques is based on chemical etching which uses hydrofluoric (HF) acid as an etchant for silica fiber. This method is simple and cheap. In this technique, optical fiber is dipped in a HF acid solution and the etching starts from the contact surface between the silica glass and HF. The interaction between silicon dioxide (SiO₂) and HF ions causes the removal of silica glass based on the following equation.



In this work, a tapered fiber is prepared from a standard communication-grade SMF with a chemical etching technique, using a solution of hydrofluoric acid (47%) for about 10 and 30 min, in order to obtain different diameters. The SMF had the diameters of core and initial cladding equal to 8.3 and 125 μm , respectively. The coating of a short section of the fiber (about several centimeters in length) is removed prior to the etching process. Next, the HEC/PVDF composite solution that has been prepared was gently

dropped onto the etched fiber, using a syringe, and is left to dry for 48 hours. Figures 3.9 (a), (b) and (c) show the microscopic images of the SMF fiber before and after 30 min- and 10 min-long etchings performed using hydrofluoric acid solution. Finally, Figure 3.9 (d) shows the etched fiber after it is coated with the HEC/PVDF composite.

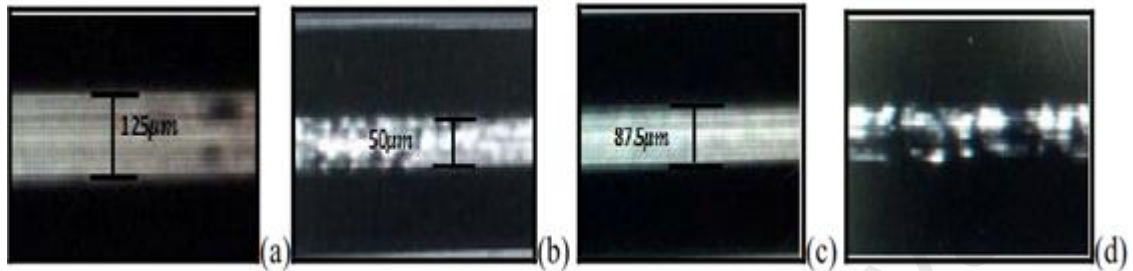


Figure 3.9: Microscopic images of the SMF (a) Before etching (with a diameter of 125 μm), (b) Etched SMF for 30 minutes (with final diameter of 50 μm), and (c) Etched SMF for 10 minutes (with final diameter of 87.5 μm) (d) Etched SMF coated with HEC/PVDF composite.

3.4.1 Performance of the FOHS based on transmission spectrum

Figure 3.10 depicts the experimental setup of the sensor aimed at detecting changes in the relative humidity using a transmission signal. The input and output ports of the microfiber are connected to a source of ASE and an OSA, respectively. A sensed probe is placed into a sealed chamber containing a dish filled with a saturated salt solution. Exposing the HEC/PVDF composite to the relative humidity changes inside the chamber produces variations in the optical transmission spectrum. In the experiment, the performance of our sensor has been investigated for the relative humidity changes using a 1365 data-logging humidity-temperature meter.

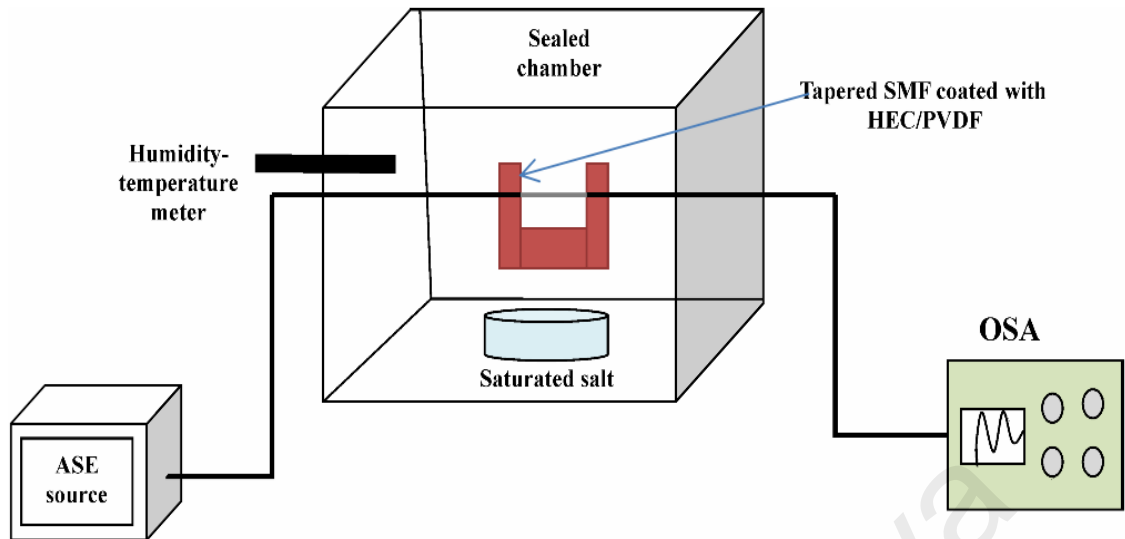


Figure 3.10: Experimental setup of our RH sensor based on transmission spectrum

The SMF diameter is reduced by chemical etching to allow the fundamental mode and higher-order modes to enter and propagate inside its core. As the light propagates through an air-cladding interface in the tapered waist region, the SMF is converted into a multi-mode fibre due to a large difference between the refractive indices of the air and the glass. These modes then recombine at the output end of the tapered fibre. The consequence of the back and forth coupling between the single mode of the untapered fibre and the two (or more) modes of the tapered fibre is oscillations of spectral response of the tapered fibre. This gives rise to a periodic behaviour of the transmission spectrum. The velocities and phases of the interfering modes at the air-cladding interface are sensitive to the change in the refractive index of the surrounding medium. Hence, various sensors can be implemented by monitoring the shifts occurring in the transmission spectrum of the modal interferometer. However, we have observed that the spectral response of the tapered fibre itself remains unchanged with varying humidity. This is the reason why the humidity measurements performed in this work are based on the tapered fiber coated with the humidity-sensitive layer such as the HEC/PVDF composite.

Figure 3.11 displays the transmission spectra of the ASE for the tapered SMF coated with the HEC/PVDF composite, which have been measured at different relative humidities ranging from 60 to 80%. The characteristics of the sensor are investigated for the cases of two tapered fibres with the diameters of 50 and 87.5 μm . As seen from Figures 3.11 (a) and (b), the transmission spectra for the both fiber diameters shift from shorter wavelengths to longer ones with increasing humidity. As an example, the wavelength corresponding to the transmittance maximum at the diameter of 87.5 μm shifts from 1554.56 to 1554.78 nm as the relative humidity increases from 60 to 80%. The wavelength shift becomes larger as the diameter of the fiber is reduced.

University of Malaya

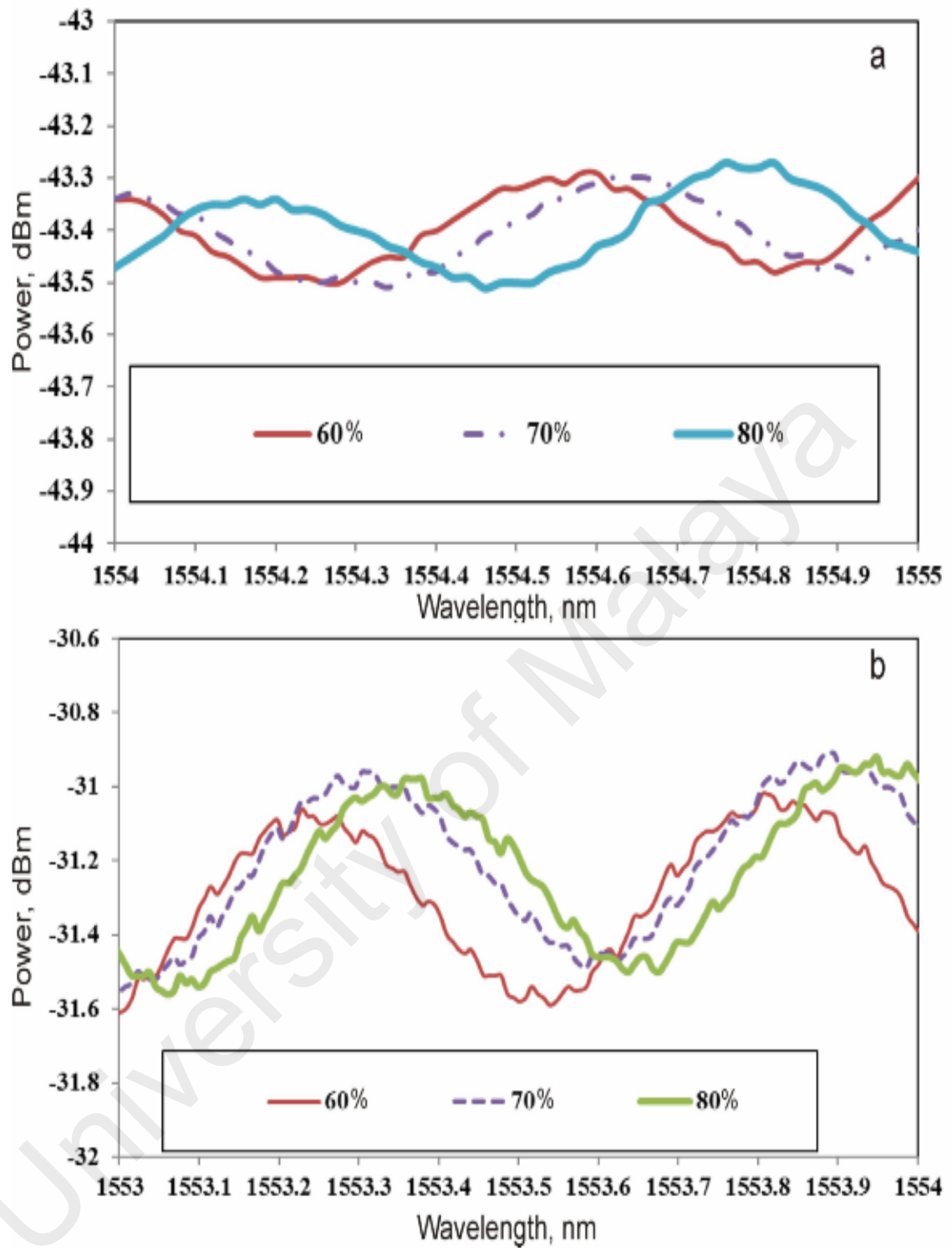


Figure 3.11: Transmission spectra of our sensor measured at different relative humidity percentages (60, 70 and 80) for the cases of tapered-fibre diameters being equal to (a) 50 μm and (b) 87.5 μm.

Figure 3.12 shows the dependencies of the wavelength transmittance maximum on the relative humidity for the HEC/PVDF-coated sensor. In the experiment, the tapered fiber diameter is fixed at the optimum diameter of 50 μm and the RH is varied at wider range from 10 % to 80 %. As seen from figure 3.12, the wavelength corresponding to the transmittance maximum shifts toward longer wavelength in a slight quadratic manner as the relative humidity increases. An increase in the humidity increases the refractive index of the HEC/PVDF layer and also the overall cladding refractive index. This in turn changes the velocity and the phase of the two modes interfering at the air-cladding interface. This effect is transformed into a shift of the comb-like transmission spectrum observed at the output of the tapered fiber. The square regression coefficient value, which measures the goodness of fit, is 0.9895 for the proposed sensor. The considerably high value of the coefficient allows the prediction of unknown relative humidity by the model. It is also observed that the RF sensor demonstrates a linear wavelength shift within a RH range from 20 to 45% as shown in figure 3.13. The sensitivity of the sensor is obtained at 0.0041nm/%. However, as the RH level is increased beyond 45%, the sensitivity of the sensor decreases as indicated by smaller wavelength change.

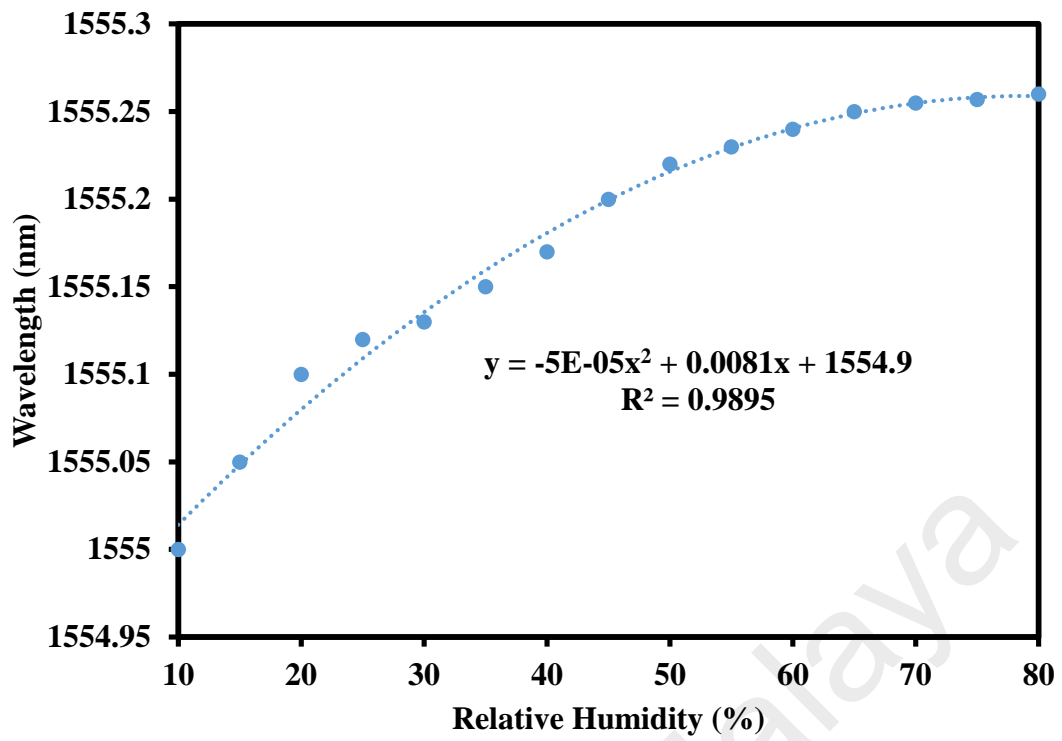


Figure 3.12: Shifts observed for the wavelength transmittance maximum with increasing relative humidity from 10 to 80%.

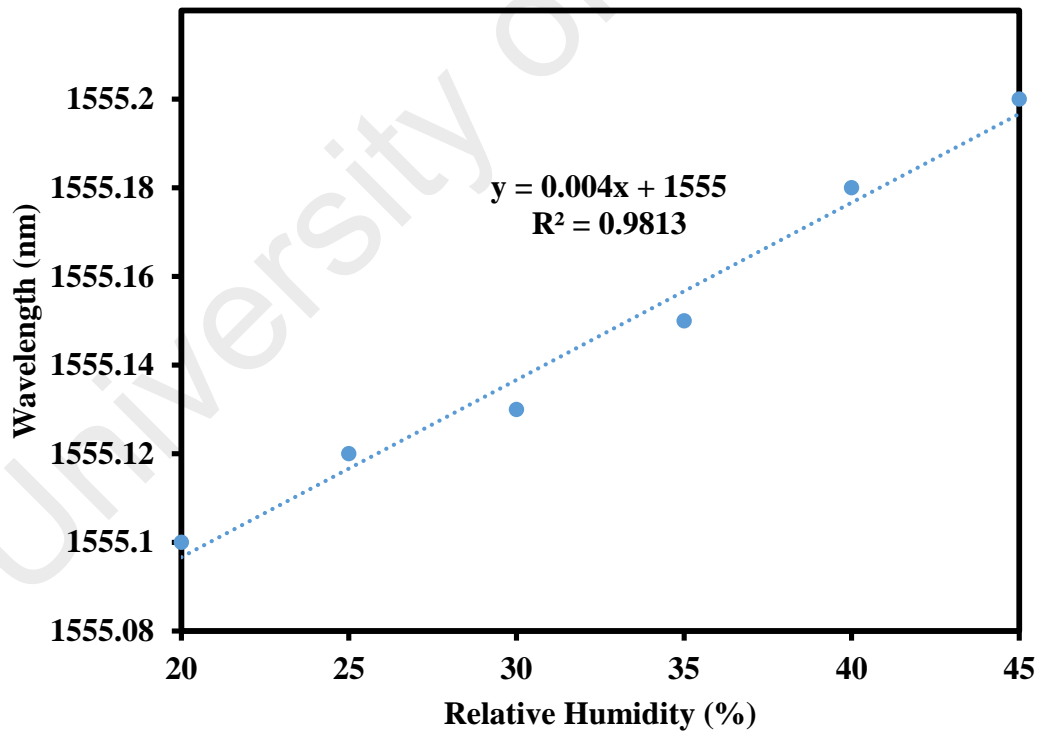


Figure 3.13: Wavelength shift against RH within a RH range from 20 to 45 %.

3.4.2 Performance of the FOHS based on reflection spectrum

In this section, a new evanescent wave based sensor is proposed and demonstrated using a tapered fiber coated with HEC/PVDF composite based on new configuration. The measurement is based on interferometric technique where the spectrum of the reflected light is investigated with respect to changes in relative humidity. Figure 3.14 shows the experimental setup for the proposed sensor, where the ASE light source is launched into a sensor probe via a 3 dB coupler. The reflected signal from the sensor is then routed into an OSA through the same coupler. The sensor probe is placed in a sealed chamber with a dish filled with saturated salt solution. Exposing the HEC/PVDF composite to the RH changes inside the chamber produces variations in the reflected spectrum. In the experiment, the performance of the proposed sensor is investigated for various changes in relative humidity ranging from 10% to 80% using a humidity meter with a data logging capability.

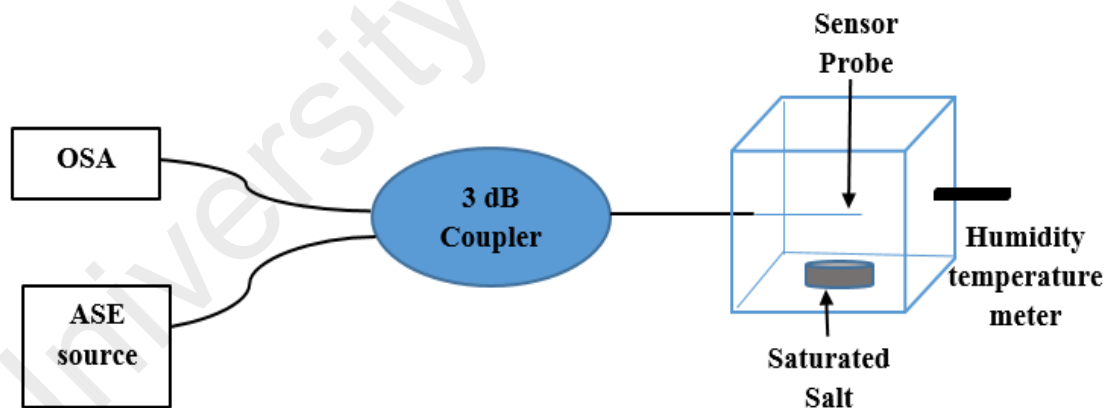


Figure 3.14: Experimental setup for the proposed sensor to detect change in relative humidity using the tapered fiber (via etching technique) coated with HEC/PVDF composite.

Figure 3.15 shows the measured ASE spectrum of the reflected light from the tapered SMF, which was coated with HEC/PVDF composite at various RH ranging from 10% to 80%. As seen in this figure, the resonant spectrum shifts from shorter to longer

wavelength with the increment of humidity. For instance, the resonant dip wavelength shifts from 1554.58 to 1554.85nm as the chamber RH is increased from 10 to 80%. The response of the sensor to humidity change can be explained as follows. The HEC/PVDF composite trapped water molecules in its body. These trapped water molecules increased the average density of the composite that resulted in an increase of its refractive index. Finally, the resonant wavelengths of the proposed sensor coated with the HEC/PVDF shifts with RH level change as a result of the refractive index change. This is opposed to the trend demonstrated by the uncoated structure where its output spectrum remains constant despite the increase in relative humidity.

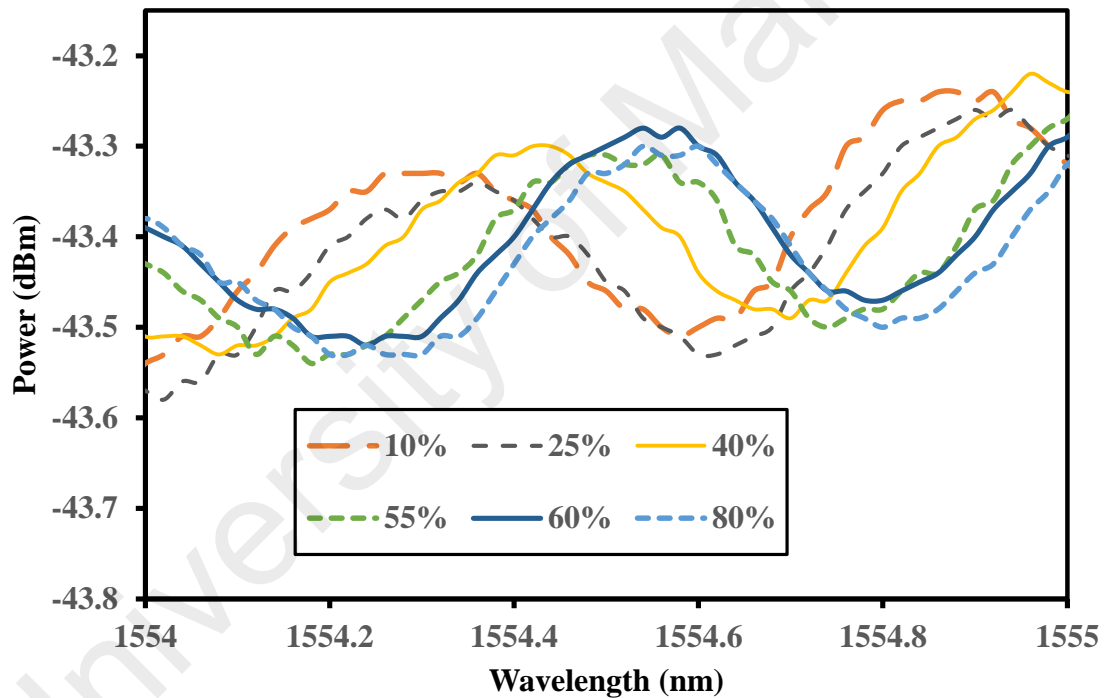


Figure 3.15: The variation of reflected spectra under different RH levels for the RH sensor configured with tapered fiber probe.

Figure 3.16 shows the sensor response to humidity measured using resonant wavelength shift. We find that the wavelength increases in a slightly quadratic manner with the increase in RH. The square regression coefficient value, which is used to measure the goodness of fit, is obtained at 0.9574. The coefficient value is considerably high but

slightly lower than the previous sensor configuration based on transmission. Figure 3.17 shows the linear region of the sensor response, which was obtained within the RH range from 20 to 45%. Within this range, the tapered fiber based sensor has a sensitivity of 0.0074nm/% with linearity of 98.85% and limit of detection of 0.65%. Next section evaluates another type of sensor probe for RH sensor.

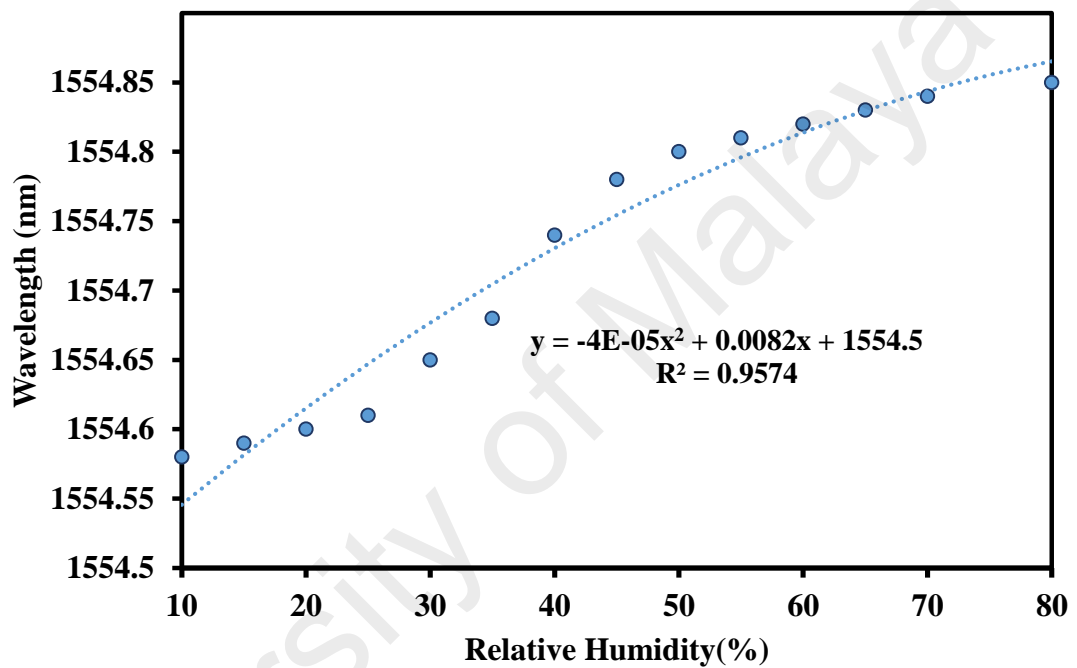


Figure 3.16: The sensor response to humidity measured using resonant wavelength shift in the proposed sensor based on reflection.

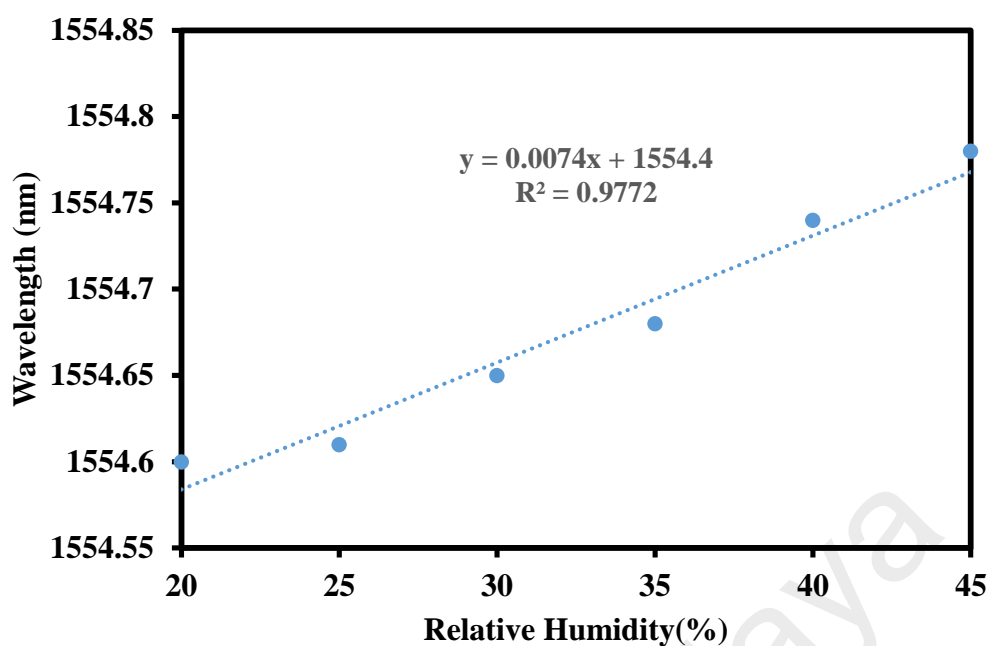


Figure 3.17: The linear relationship between humidity and resonant wavelength shift within 20 to 45% RH range

3.5 Fiber Bragg Grating (FBG) based humidity sensor

The possibility of inscribing a Bragg grating in conventional optical fibers opens a new field for optical sensing, being the subject of considerable research in recent years due to their advantages over conventional electronic devices. Till today, fiber Bragg gratings (FBGs) have been extensively studied for sensing various physical parameters such as temperature, strain, pressure, acceleration, torsion, flow and others (Balta et al., 2005), (Dawood et al., 2007; P. Wang et al., 2011) (Müller et al., 2009). For instance, FBG sensors can monitor deformations and stresses in reinforced concrete elements, and urban infrastructures when they are used in structural monitoring (Ansari, 2005) (Abrate, 2002). The FBGs are also suitable for distributed temperature sensing and they have high detection accuracy, but the temperature sensitivity is usually low. Recently, an etched FBG have attracted much interest as they exhibit a proportionally large evanescent field that travel along the cladding and can be manipulated for various sensing applications

(Zhang et al., 2013), (Hassan et al., 2012). Consequently, the travelling wave characteristics of an etched FBG are more sensitive to the ambience of its surrounding.

In this section, we present an innovative RH sensor based on FBG coated with HEC/PVDF composite. Changes in relative humidity alter the physical and optical properties of the coating thereby influencing the evanescent waves that travels within the coating (Batumalay & Harun, 2013).

3.5.1 Preparation of the sensor probe and experimental setup

A Bragg grating is a passive optical device based on the refractive index modulation of the optical fiber core, created through the exposure of the fiber optics core to an optical interference pattern of ultraviolet radiation. The operation principle of a FBG is based on the signal reflection in each plane of the periodic structure. When the Bragg condition is matched, all the reflected components are in phase and are added, otherwise, the components are out of phase and vanished. The Bragg wavelength, λ_B , at which the central wavelength of the reflection mode satisfies the first order Bragg condition, is given by:

$$\lambda_B = 2\Lambda n_{eff} \quad (3.2)$$

where Λ is the refractive index modulation period and n_{eff} is the optical fiber core effective refractive index (Srimannarayana et al., 2008). The Bragg wavelength depends both on the n_{eff} and Λ and, therefore, any external disturbance acting on these parameters can be measured by analyzing the Bragg wavelength of the reflected signal. Here, we used the FBG core and cladding diameters of $8.3 \mu m$ and $123 \mu m$, respectively as a probe.

In order to improve the sensitivity of sensor, the cladding of FBG was chemically etched using an aqueous solution of hydrofluoric acid (HF). It is because, when the cladding is reduced, the effective refractive index of fundamental mode is strongly

affected by surrounding refractive index and a change in the refractive index also causes a wavelength shift ($\Delta\lambda_n$) [9]:

$$\Delta\lambda_n = 2\Delta n \Delta\eta_p \quad (3.3)$$

where $\Delta\lambda_n$ is the change in wavelength of Bragg reflection, Δn is the difference between the cladding refractive index and surrounding refractive index and $\Delta\eta_p$ is the variation of the fraction of the total power of the unperturbed mode that flows in the etched region. The etching process is neutralized by immersing the fiber in distilled water. The etched FBG sensor was produced with the fiber immersed in the acid solution for about 30 minutes, resulting in a diameter of approximately $89 \mu m$ as shown in Figure 3.19.

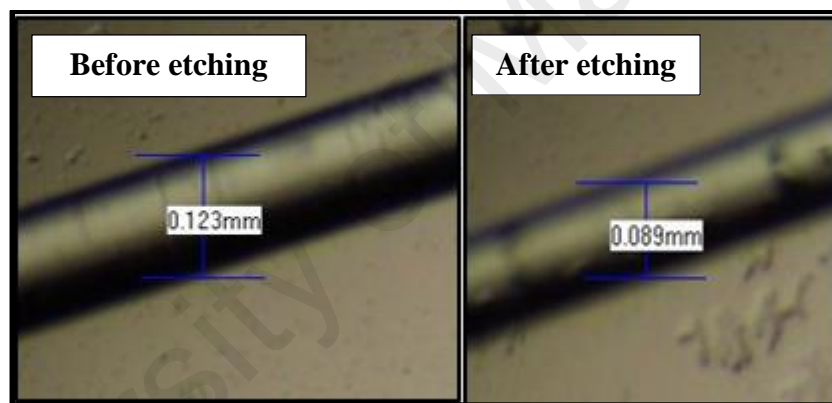


Figure 3.18: Microscope image of the FBG before and after etching with HF

Figure 3.19 show the FBG reflection spectrum before and after the etching process. As shown in the figure, the Bragg wavelength slightly shifted from 1557.36 nm shifts to the longer wavelength of 1557.44 nm after the etching. This is attributed to the stress during the etching process, which increases the refractive index of the cladding and shifts the Bragg wavelength to a longer wavelength. The FBG loss is also increased with the etching process, which is most probably due to the micro-bending loss.

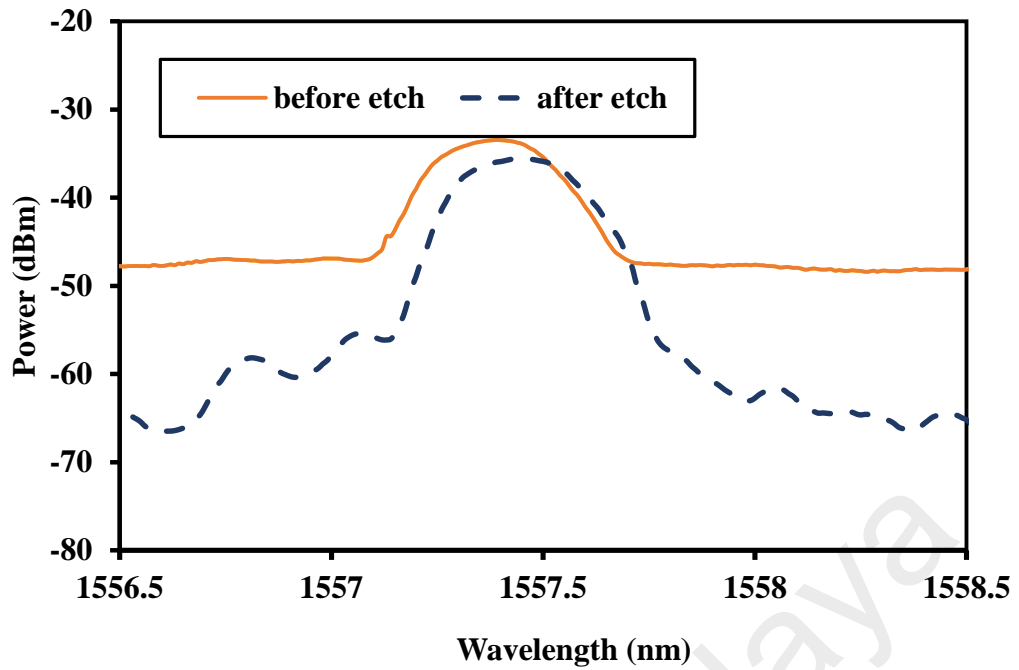


Figure 3.19: The reflection spectrum of the FBG before and after etching process.

Hygroscopic expansive polymers provide a promising approach to make humidity sensors because the polymer's volume will expand after absorbing water. The volume expansion induced elongation or refractive index (RI) change, which can be used for humidity sensing as described in the previous sections. In our earlier work, the HEC/PVDF polymer is coated on the surrounding surface of a tapered fiber for RH sensor. In this work, the prepared HEC/PVDF composite solution was slowly dropped onto the tapered FBG using syringe and left to dry for 48 hours. The tapered FBG coated with HEC/PVDF is used as a new probe for RH sensor. The performance of the RH sensor is evaluated using the experimental setup similar to Figure 3.14. The FBG was put on a closed chamber and it was connected to ASE source and OSA via a 3 dB coupler.

3.5.2 Performance of the FBG based RH sensor

A group of the reflection spectra under different relative humidity levels is illustrated in Figure 3.20. In this experiment, the chamber relative humidity level is adjusted from 10 %RH to 80 %RH. From these results, it is clearly seen that the Bragg wavelength of the HEC/PVDF polymer-coated FBG humidity sensor shifts toward the long-wavelength direction (red shift) as the relative humidity level increases. In Figure 3.21 another group of wavelength is shown to shift under different RH environmental conditions. It is observed that the wavelength increases in a slight quadratic manner with the increase in RH with the square regression coefficient values equal to 0.9783. This is attributed to the reduced cladding, which allows the surrounding humidity to interact with the HEC/PVDF polymer. The change of the refractive index of the polymer causes a wavelength shift as shown in the Figure 3.21.

Figure 3.22 shows another group of measured results on Bragg wavelength shifts under different RH at two different regions of 20 to 45 % and 50 to 80 %. From these results, a good linear relation between the Bragg wavelength and the relative humidity level can be confirmed within these two regions. The sensitivity of the sensor is obtained at 0.0011 nm/% at a RH range from 20% to 45%. At another range from 50 to 80 %, the sensitivity obtained is lower (0.0008 nm/%). This is attributed to the polymer coating on the fabricated FBG humidity sensor, which is not uniform all over whole FBG section as well as the adhesiveness of polymer coating to the fiber will decrease in high temperature condition. Since a polymer coated FBG sensor is sensitive to the temperature variation, temperature compensation is vital in this type of sensor.

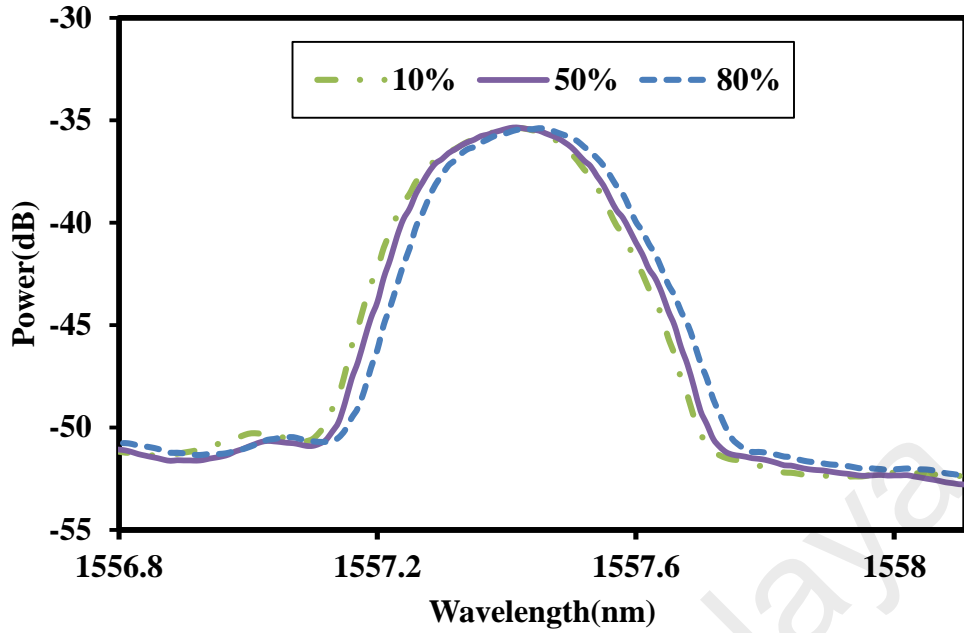


Figure 3.20: Measured reflection spectra of the FBG sensor under different reflective humidity levels

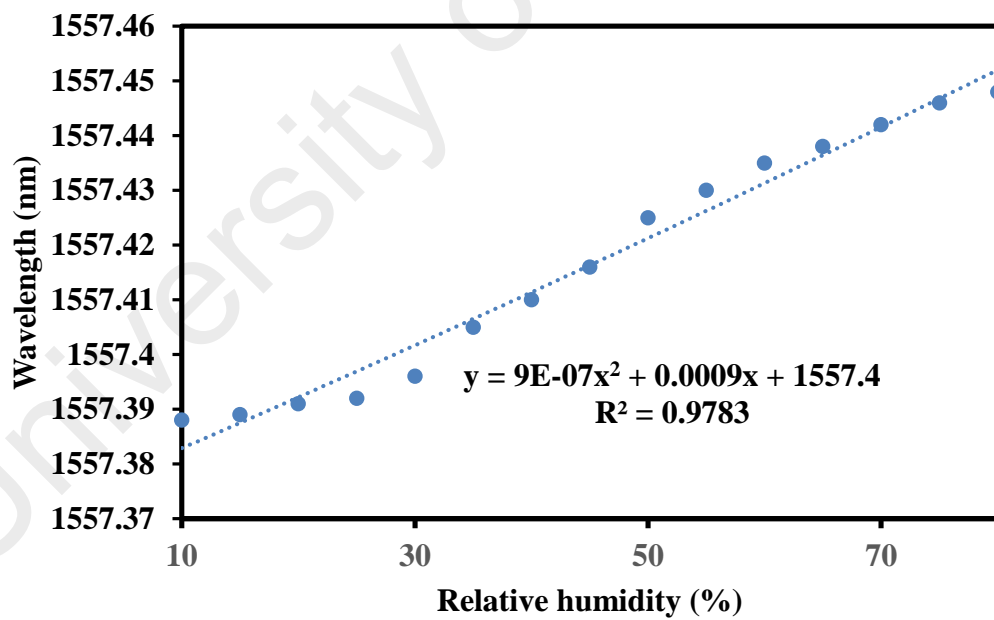


Figure 3.21: Wavelength shift versus relative humidity for the proposed FBG sensor

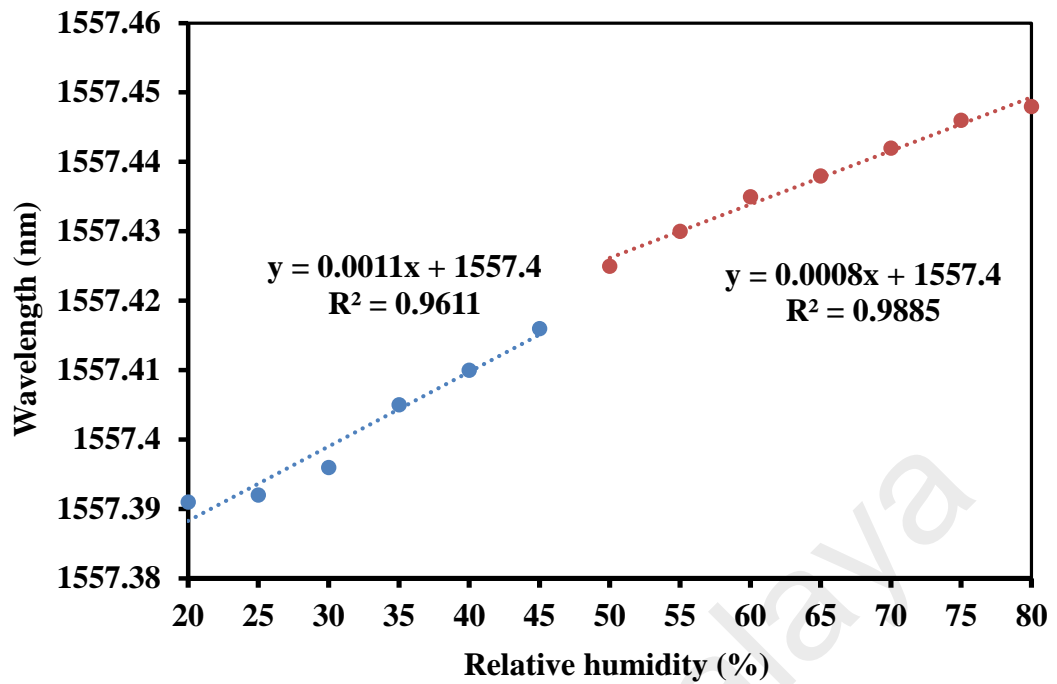


Figure 3.22: Linear relationship between the wavelength shift and relative humidity within the range of 20-45% and 50-80%.

3.6 Summary

In this chapter, two main sensing methods; intensity modulation and interferometric technique are evaluated for RH measurements. A mixture of HEC and PVDF is used as a coating material for the tapered fiber. These material are relatively common and inexpensive and the resulting polymer gel has a good absorption of water in the air. The hydrogel coating acts as an inner cladding whose refractive index decreases with the rise in humidity and thus allows more lights to be transmitted in humid state. A difference of up to 0.89 dB of the transmitted optical power is observed when RH changes from 50 to 80%. The proposed sensor has a sensitivity of about 0.030 dB/%RH with a slope linearity of more than 99.5 %.

A simple humidity sensor is also tested based on interferometric technique using a tapered non-adiabatic SMF coated with a mixed polymer composite HEC/PVDF. The tapered fiber, coated with a humidity-sensitive cladding creates intermodal interference

which enables the detection of humidity change. Based on transmission technique, the sensitivity of the sensor is obtained at 0.0041nm/% within the RH range from 20 to 45 % at the optimum tapered fiber diameter of 50 μm . The performance of the sensor is also investigated based on the reflected light from the sensor probe. It is observed that the resonant dip wavelength increases from 1554.58 to 1554.85 nm as the RH increases from 10 to 80%. Finally, an innovative RH sensor based on FBG coated with HEC/PVDF composite is introduced. It is observed that the reflected wavelength of FBG is red-shifted as the relative humidity increase from 10% to 80%. This is attributed to the changes in RH alter the physical and optical properties of the coating thereby influencing the evanescent waves that travels within the coating. The sensitivity of the sensor is obtained at 0.0011 nm/% within a RH range from 20 % to 45 %. The performance of the interferometric based RH sensor is summarized in Table 3.1.

Table 3.1: The performance of humidity sensor using interferometric technique

Parameter	SMF (Transmission)	SMF (Reflected)	FBG
Sensitivity (nm/%)	0.004	0.0074	0.0011
Linear Range (%)	20-45	20-45	20-45
Linearity (%)	99.1	98.85	98.05

These results show that all the tested sensors can potentially be applied for RH measurement as they are easy to fabricate and configured. However, for the FBG, a special equipment is needed which increases the overall cost. In Chapter 4, a new sensor is introduced to improve the sensitivity of the previous sensor.

CHAPTER 4: DEVELOPMENT OF NEW INLINE MACH-ZEHNDER INTERFEROMETER (IMZI) FOR SENSING APPLICATIONS

4.1 Introduction

Interferometry is the technique of superimposing two (or more) waves to obtain an interference spectrum due to the phase differences between these waves. An interferometer utilizes two waves with the same wavelength. If they have the same phase, their electric fields will add to each other constructively; otherwise, if there is a 180° phase difference between them they add destructively. Typically, an incoming light wave is split into two (or more) parts, and then recombined to create an interference pattern after traveling different optical paths. Optical paths difference by an integral number of wavelengths (or odd multiple of half wavelengths, i.e. 180° out of phase) correspond to constructive (or destructive) interference. In terms of the optical spectrum, the minimum attenuation wavelength can be “shifted” to maximum attenuation wavelength if the optical path difference varies by 180° . Based on the maximum (or minimum) attenuation wavelength shift one can tell the phase difference induced by the environmental (i.e. refractive index or strain) change, hence the interferometer can be utilized as a sensor. Different configurations of interferometers have been realized with the optical fibers, i.e. Fabry-Perot interferometers (FPI) (Jiang & Gerhard, 2001), Sagnac interferometer (SI) (Moon et al., 2007), Mach-Zehnder interferometer (MZI) (Allsop et al., 2002) and Michelson Interferometer (MI) (Swart, 2004).

FPIs are widely used in telecommunications, lasers and spectroscopy for controlling and measuring the wavelength of light (Hernández, 1988). A FPI is typically made of a transparent plate with two reflecting mirrors. Basically, the FPI can be divided into two types; extrinsic and intrinsic FPIs. The extrinsic FPI can be formed by air or polymer where its cavity is located at outside of the fiber. Although, the fabrication of

this type of FPI is relatively simple and low cost, it has many limitations such as low coupling process, need careful alignment and have packing problems. On the other hand, the cavity of an intrinsic FPI is formed inside the fiber by using a few techniques such as refractive index mismatch (Huang, Zhu, Chen, & Wang, 2005; Wei, Han, Tsai, & Xiao, 2008), fiber Bragg grating (FBG) (Z. Wang, Shen, Song, Wang, & Wang, 2007) and chemical etching (Machavaram, Badcock, & Fernando, 2007). However, these FPIs also suffer with few disadvantages such as the needs of complicated equipment, special fibers and involved dangerous chemical reagents for fabrication.

An SI is formed by two splitting light waves, which are propagating in opposite directions. It is based on Sagnac configuration (Fu et al., 2008) where the interference spectrum is realized due to the interaction between these two waves. Information about the waves can be extracted from the resulting interference of the waves which are examined in order to detect very small changes in the waves' properties. This technique is useful in a variety of applications including measurement, sensing and lasers (Fu et al., 2008; Moon et al., 2007). Recently, the MZI and the MI have also received tremendous attention especially in optical fibers sensors applications due to their advantages such as easy fabrication and high sensitivity. The interference principles of MI are quite similar to the MZI except that MI only requires one fiber structure to use as a splitter and combiner.

MZIs can be considered as an excellent fiber optical interferometer due to their simple structure and they are widely used for many applications in photonics devices. Up to date, there are several methods used to fabricate an optical fiber interferometer. Three main methods have normally been used in the fabrication of optical fiber interferometer; a sapphire rod heated by flame (Tong, 2010) a micro sapphire cylinder heated by CO₂ laser (Sumetsky, Dulashko, Fini, Hale, & DiGiovanni, 2006) and the flame brush technique (G Brambilla, Jung, & Renna, 2010).

With the advent of optical fiber technology, a considerable level of research activity has focused on in-line fiber optic interferometers. Compared with the conventional MZI which are based on two fiber couplers, the in-line MZI structure have the advantages of small size, easy fabrication and low cost. In this chapter, we propose a new inline MZI based on a simple dumbbell-shape structure. The MZI is fabricated using an arcing process of a fusion splicer to form two bulges, which are separated by a tapered waist. This MZI is sensitive to changes in its surrounding refractive index. Here, the proposed MZI structure is used to detect changes in relative humidity and various biochemical concentrations in distilled water.

4.2 Fabrication of in-line MZI

As one of the excellent fiber optical interferometers, inline MZI has virtues of simplicity, all fiber and inexpensive. In this work, the inline MZI is fabricated from a standard silica single-mode fiber (SMF) using a fiber stripper, a cleaver and a fusion splicer machine (Sumitomo Type 39). The SMF used has a core and cladding diameters of 8.3 μm and 125 μm , respectively. The first step in fabricating the MZI structure is to strip and cleave an SMF into two sections as illustrated in Figure 4.1. In the stripping process, the protective coating around optical fiber was removed in preparation for the next cleaving and fusion splicing processes. The fiber was separated into two sections, each with a flat and smooth end-surface during the cleaving process as illustrated in Figure 4.1(b)

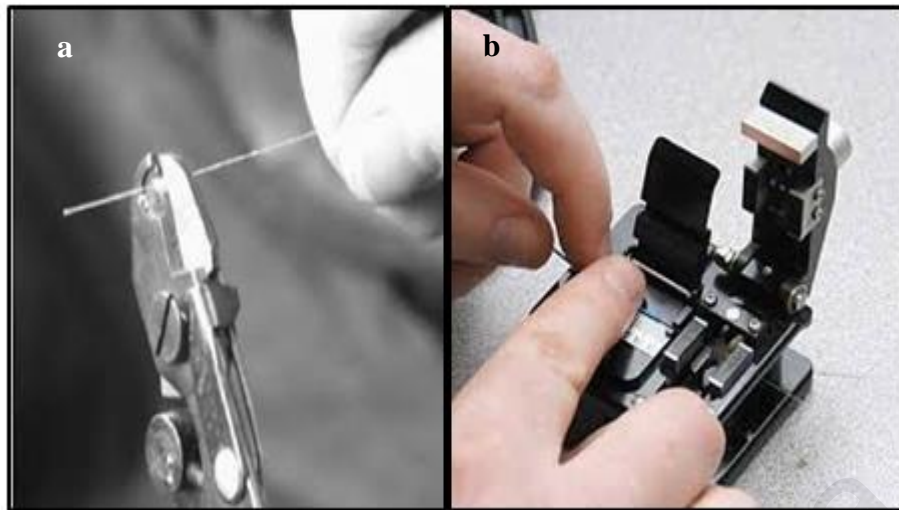


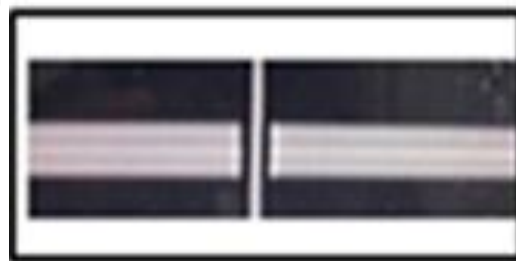
Figure 4.1 : (a) Stripping and (b) cleaving of a bare SMF

Figure 4.2 shows the image of the fusion splicer used in this study. Inset of Figure 4.2 depicts the top view image where both cleaved fibers are placed onto the holders. The fabrication of a dumbbell shape MZI is carried out using a manual “arc” function. In the process, the end facets of both fibers are matched and aligned manually using a keypad as shown in Figure 4.3 (a). In the experiment, the pre-fusion and fusion times are fixed at 0.05s and 1.65s, respectively while the “overlap” parameter is varied to fabricate a bulge structure with different diameters. While fusing the two sections of the fiber, the “arc” function is used so that extra pressure is exerted from both sides to form the first bulge at the joint as shown in Figure 4.3 (b). Once the first bulge is formed, the jointed fiber is then cleaved once again at a few mm away from the center of the first bulge as depicted in Figure 4.3 (c). Then the second bulge is formed in a similar fashion. It should be noted that the fusion splicer softens the ends of the two fibers with heat before pulling them together to join them at the center. When the “arc” function is used repeatedly, more material is lumped at the center, thus forming a bulge, while the neck of the bulge gets thinner. When the second bulge is made, it is a bit smaller in size than the first one as less material is available from the waist area between the bulges since it has been used to form the first bulge. The waist area also becomes thinner as it gets tapered even more. The

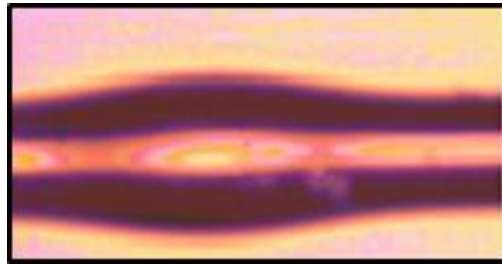
completed dumbbell structure is shown in Figure 4.4 where the diameters of the first and second bulges are approximately around $198\ \mu\text{m}$ and $196\ \mu\text{m}$ respectively.



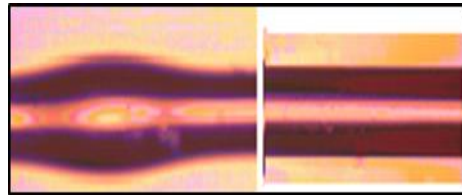
Figure 4.2: The image of a fusion splicer machine (Sumitomo Type 39). Inset shows the image of the working area.



(a) The image of end facets of two fibers, which are matched and aligned using a manual operation



(b) The first bulge of MZI structure.



(c) The second bulge is formed in a similar fashion.

Figure 4.3: Three steps in fabricating the MZI structure (a) end facets of two fibers are matched and aligned using a manual operation (b) The first bulge of MZI structure is formed using a multiple arching process. (c) The second bulge is formed in a similar fashion.

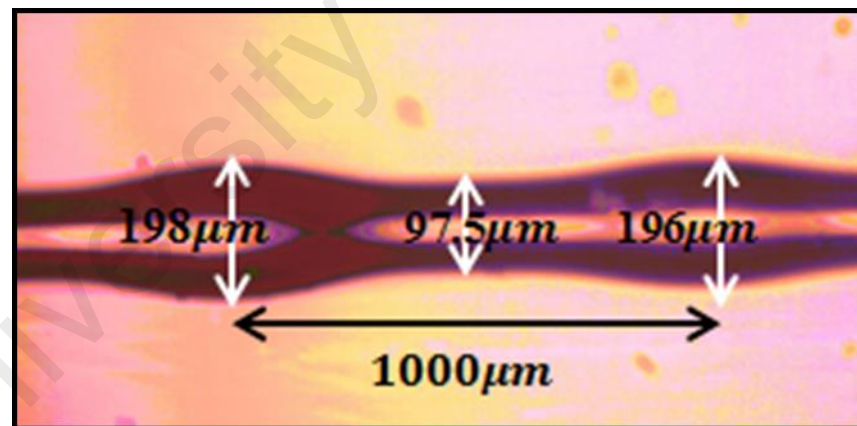


Figure 4.4: The microscope image of the fabricated dumbbell shaped MZI

4.3 The operation principle and transmission characteristic of the dumbbell shaped MZI

The propagation of light modes inside the dumbbell shape MZI is illustrated in Figure 4.5. The MZI consists of two arc-induced bulges in a single mode fiber, which functions as the beam splitter and beam combiner. The cladding modes are excited from the core mode by the first bulge, and then enter in an interferometer arm to travel in the fiber cladding. The rest of the light energy left in the core continues propagating forward. Before the core mode and cladding modes reach the second bulge, different modes possess different phase thus making the modal phase difference. Parts of the cladding modes are coupled back to the core of the SMF by the second bulge to make the modal interferences.

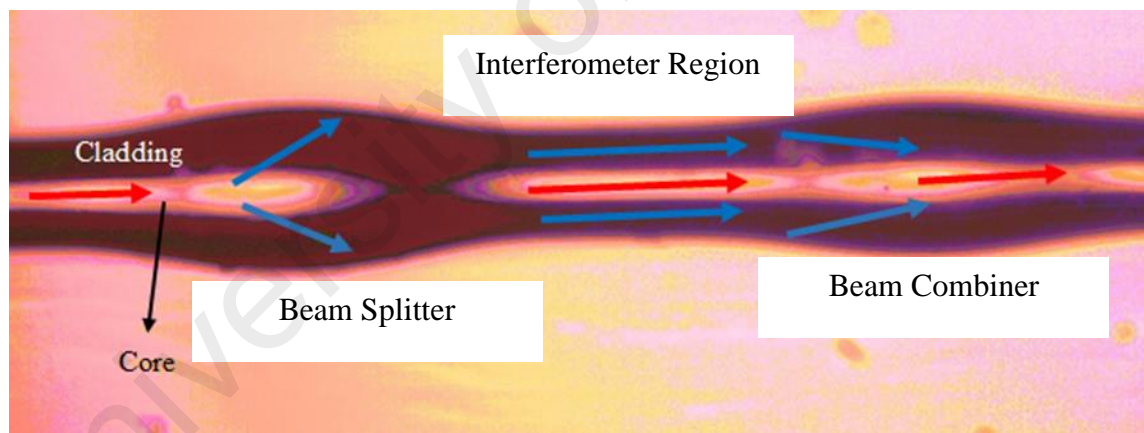


Figure 4.5: Core and cladding modes propagation inside the proposed dumbbell shape MZI

Due to the optical phase difference (OPD) between cladding modes and core mode, an interference pattern could be achieved from the output side in the case of a flat spectrum input. The output intensity of the MZI is governed by:

$$I = I_1 + I_2 + 2\sqrt{I_1 I_2} \cos(\varphi) \quad (4.1)$$

where I is the intensity of the interference signal, I_1 and I_2 are the intensity of the light propagating in the fiber core and cladding respectively and φ is the phase difference between the core and cladding modes. It is approximately equal to:

$$\varphi = \left(\frac{2\pi(\Delta n_{eff})L}{\lambda} \right) \quad (4.2)$$

where Δn_{eff} is defined as $(n_c^{eff} - n_{cl}^{eff})$ which is the difference of the effective refractive indices of the core and the cladding modes, L is the length of the interferometer region and λ is the input wavelength.

For a broadband spectrum input, an interference pattern in the output can be obtained when an OPD exist between the cladding mode and core mode. Since the two bulges act as a beam splitter and combiner, changes in their diameters (or thickness) lead to the change in output transmission spectrum where the extinction ratios of the interference fringe can be controlled. To verify these characteristics, we produce several dumbbell shaped MZIs with different diameters and detect their transmission spectra. Figure 4.6 shows three different MZIs with bulges diameters of 177 μm , 183 μm and 195 μm , which were obtained by setting the overlap parameters at 20 μm , 40 μm and 80 μm , respectively. The respective transmission spectra are depicted in Figure 4.7, which indicate interference combs with a free spectral range (FSR) of around 3.6 nm for all the spectra. This shows that size of bulges does not affects the FSR of the output comb spectrum. However, it is observed that the extinction ratio (ER) of the interference spectrum increases from 0.18 dB to 0.22 dB as the bulge diameter increases from 177 μm (overlap of 20 μm) to 195 μm (overlap of 80 μm).

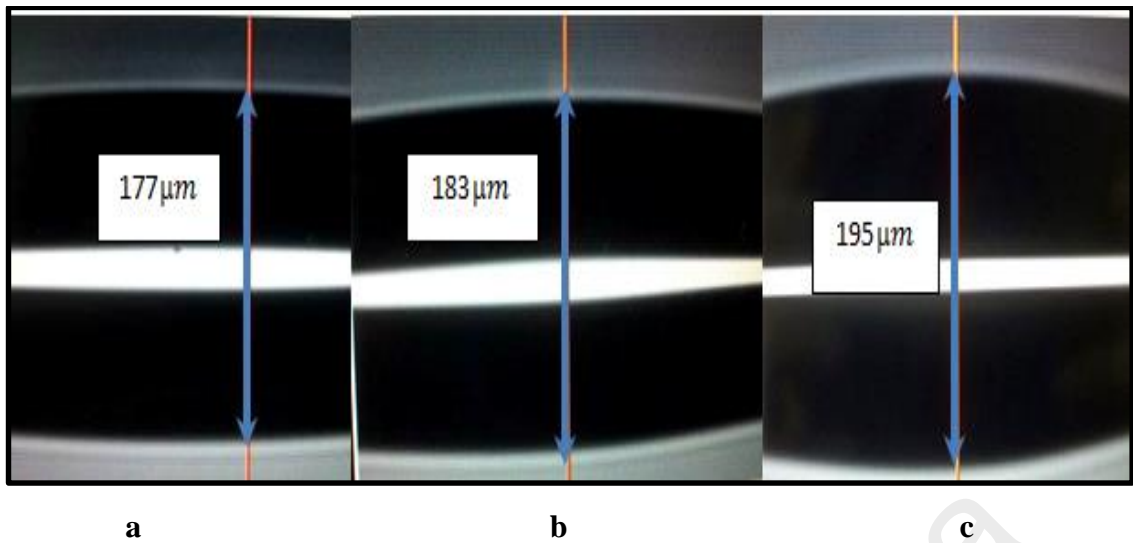


Figure 4.6: Bulges of MZI with diameter of (a) 177 μm (b) 183 μm and (c) 195 μm

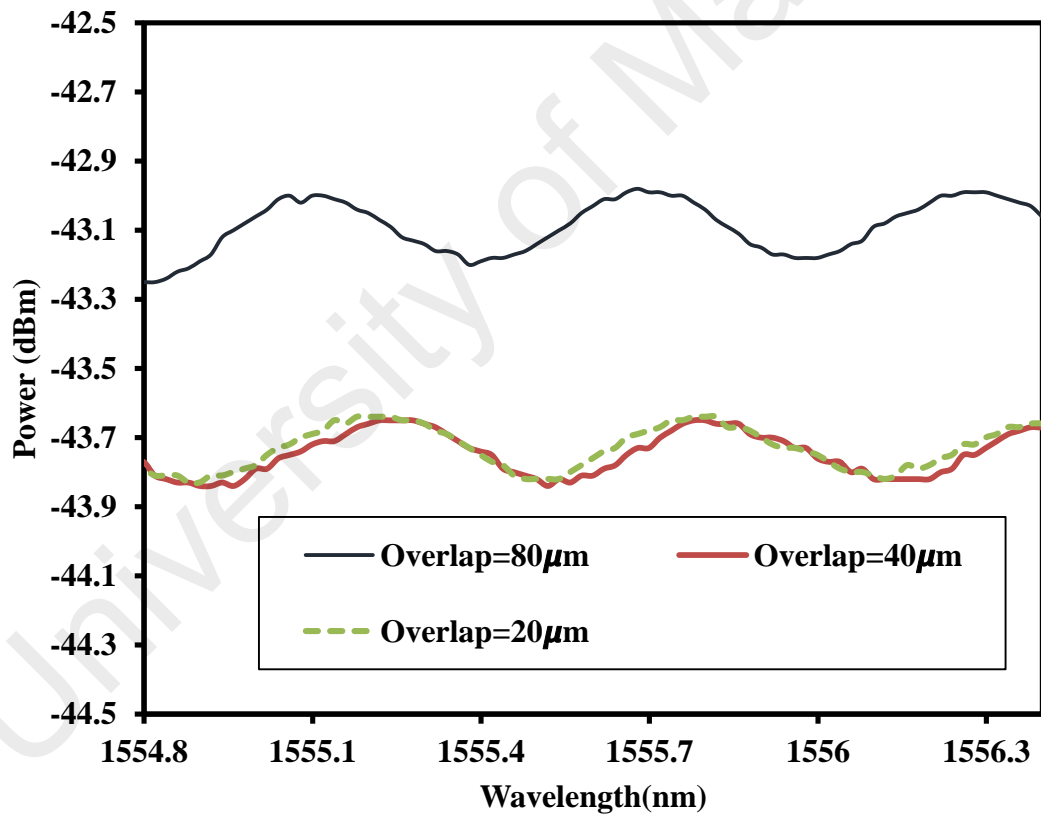


Figure 4.7: Transmission spectra of the MZI for three different bulge diameters

We also investigate the effect of separations between two bulges or the length of interferometer region on the characteristic of the transmission spectrum.

In the experiment, two different dumbbell shape MZI with lengths of interferometer region (**L**) of 0.1cm and 0.5cm are fabricated to investigate their transmission spectrum. Theoretically, the FSR of the transmission spectrum can be expressed as:

$$FSR = \lambda^2 / (\Delta n_{eff})L \quad (4.3)$$

where L is the separations between two bulges. Figure 4.8 compares the output spectrum for both dumbbell sensors. The unsmooth curve for both spectra is attributed to the non-uniqueness of cladding modes, which travels to the beam combiner and interferes with the core mode. It can be observed from this figure that, with the increase of the tapered waist length from 0.1 cm to 0.5 cm, the FSR at around 1549 nm region is decreased from 0.6 nm to 0.5 nm, which conforms to Equation 4.3. From these results, it can be concluded that the larger diameter bulges produces the higher ER, while the longer interferometer length produces the lower FSR.

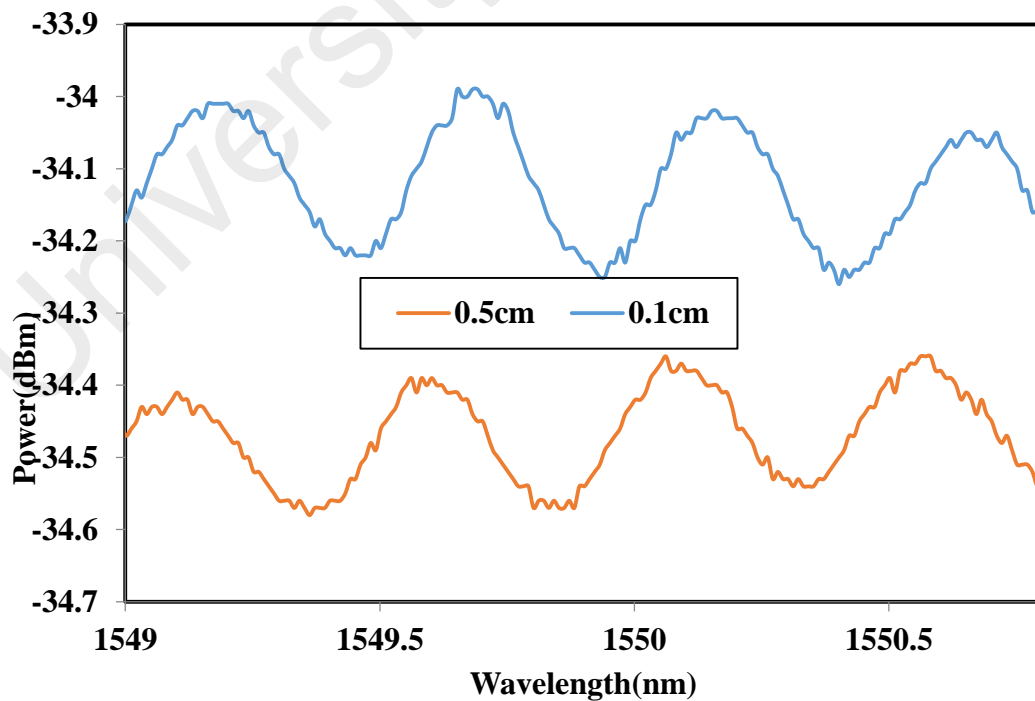


Figure 4.8: Output spectrum for the two dumbbell sensors with different length L

Next, two dumbbell shape MZIs are fabricated; one with bulge diameter of 195 μm and separation length 0.1cm, and another with the bulge diameter of 185 μm and separation length 0.5 cm. Both MZIs are used to investigate the effect of surrounding temperature on the characteristic of the output spectrum. It is well-known that the phase difference between the core and cladding modes is strongly dependent on the effective refractive index of the core and the cladding modes as well as the length of the interferometer region. Since the effective refractive index of the cladding is sensitive to the refractive index of the surrounding medium, the temperature variation leads to shift in the interference fringe spectral. This is due to changes in the effective refractive index difference between the core and the cladding modes, and the effective length of the interferometer. These are the results of the thermo-optic and thermal expansion effects respectively. The relationship can be expressed as (Kim et al., 2005):

$$\frac{\Delta\lambda}{\lambda} = \left(\frac{\Delta\eta_{eff}}{\eta_{eff}} + \frac{\Delta L_{eff}}{L_{eff}} \right) \text{Temp} = (\alpha_{TOC} + \alpha_{TEC}) \Delta T \quad (4.4)$$

where α_{TOC} and α_{TEC} is the thermal-optic coefficient (TOC) and thermal expansion coefficient (TEC) respectively.

Figure 4.9 shows the experimental set-up to investigate the effect of the surrounding temperature on the characteristic of both MZI sensor probes. We use an ASE source in conjunction of OSA to monitor the reflected spectrum at various surrounding temperature induced by the hot plate. The MZI bulge structure was placed on a hot-plate and the temperature was gradually increased up 130 °C while the interference spectrum was recorded for the experiment by OSA. Figure 4.10 and 4.11 shows the recorded interference spectra as the temperature is varied from 50 °C to 130 °C for L=0.5cm and 0.1 respectively. It was found that the interference dip shifts towards longer wavelength as the temperature increases. This is attributed to the heat that increases the effective index difference between the core and cladding modes as well as the effective length of

the interferometer, which in turn changes the phase difference and wavelength spacing of the interference spectrum according to Equation 4.4.

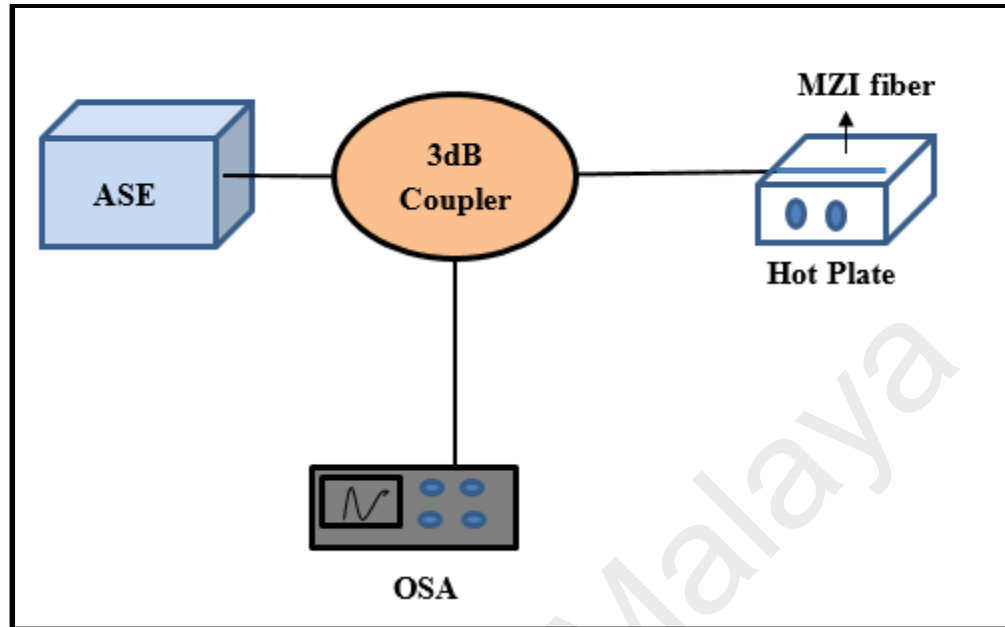


Figure 4.9: Experiment set-up for the thermo-optic and thermal expansion

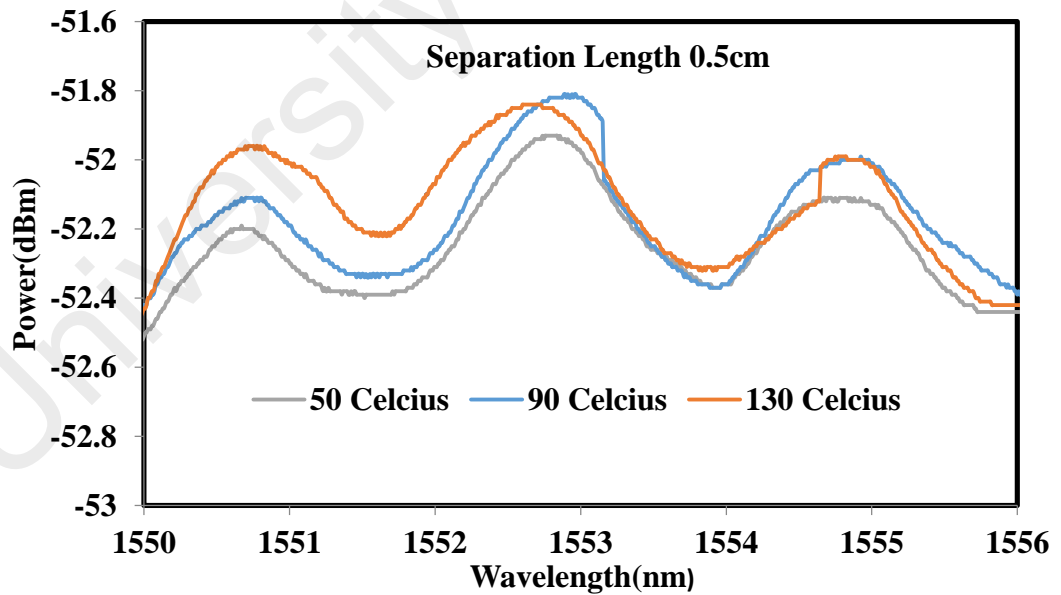


Figure 4.10: Temperature response of the MZI with L=0.5cm

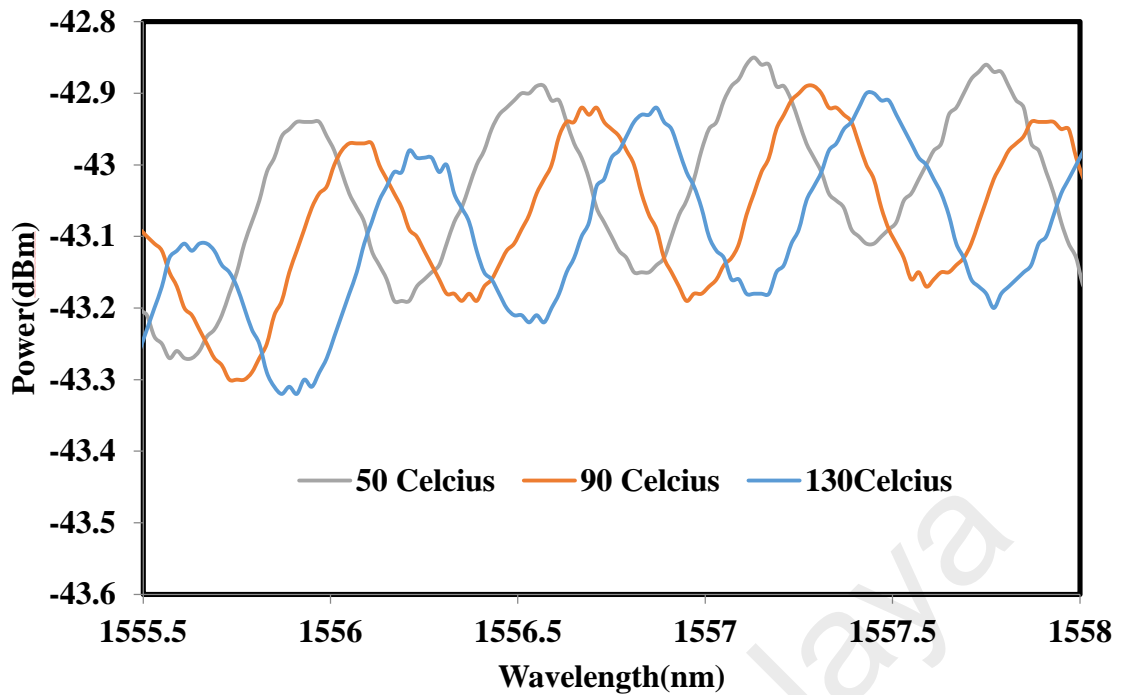


Figure 4.11: Temperature response of the MZI with $L=0.1\text{cm}$

Figure 4.12 shows the wavelength shift versus the temperature increase for temperature measurement ranging from $50\text{ }^{\circ}\text{C}$ and $130\text{ }^{\circ}\text{C}$. It is observed that the sensitivity of the first MZI with bulge diameter of $195\mu\text{m}$ and separation length of 0.1cm is 0.0061 nm/Celsius with a slope linearity of more than 98.78% . However, the sensitivity the second MZI with bulge diameter of $185\mu\text{m}$ and separation length of 0.5cm reduces to 0.0024nm/Celsius . From the observation, it is found that the insertion loss of the device goes up with the increase of the separation length. The reason is that the part of light that propagates along the air cavity will have to travel a longer distance as the waist length increases. Since the light propagating along the air cavity has a higher possibility to leak out as loss, the amount of the loss is proportional to the propagation distance. The characteristic of the proposed sensor is summarized in Table 4.1. It can be concluded that the sensor with shorter separation length and larger bulge's diameter shows a better performance in term of sensitivity. In the next section, the MZI with bulge diameter of

195 μ m and separation length of 0.1cm will be used as a sensor probe for relative humidity measurement.

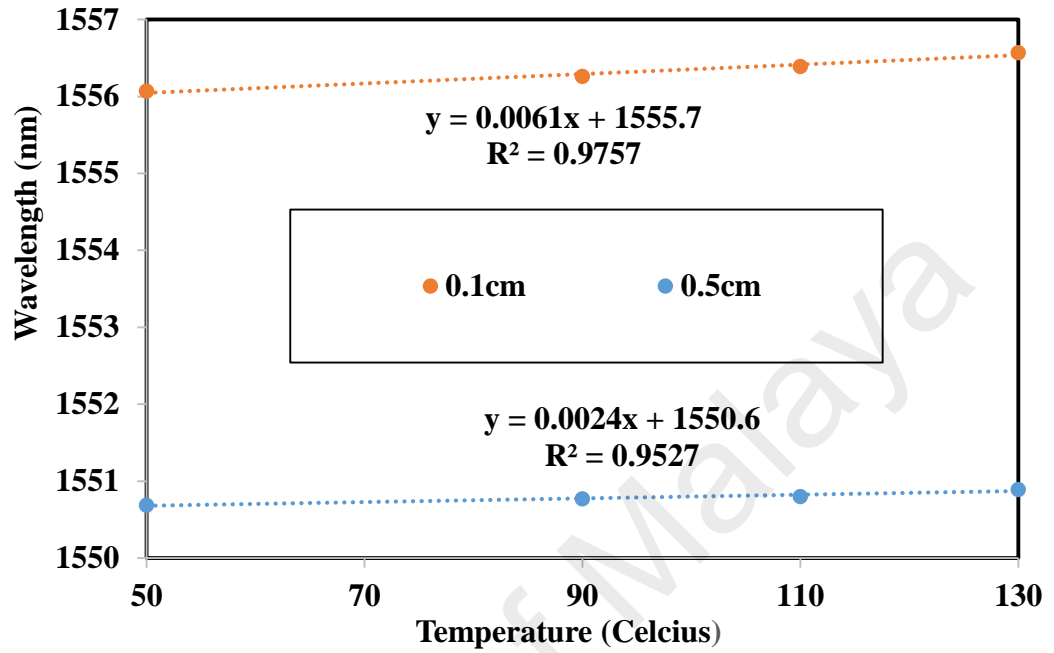


Figure 4.12: The wavelength shift against the temperature

Table 4.1: The characteristic of the IMZI sensors

Separation Length(cm)	Diameter(μ m)	Sensitivity (nm/Celsius)	Linearity (%)	Wavelength shift	Loss (dBm)
0.5	185	0.00024	97.6	Red-shift	20
0.1	195	0.0061	98.7	Red-shift	10

4.4 Dumbbell shape MZI for Relative Humidity measurement

Relative humidity (RH) is used to remark the dryness of the atmosphere, which is defined as the ratio of the water vapor in air to the maximum amount of water vapor under a certain temperature and pressure. It plays an important role in numerous industries like mining, chemical and biomedical plants as it may affect product quality and workers' health. RH is also monitored in big structures such as bridges or planes to control possible risks of corrosion (Jesus M Corres, Matias, & Arregui, 2008). In forestry areas, the RH of the environment is an essential parameter, which can forecast forest weather and judge the forest combustion. Up to date, RH measurement has been extensively studied and a great variety of sensors, including capacitive, resistive, thermal conductivity and optical humidity sensors have been developed in last few decades. So far, the humidity sensor market is monopolized by electronic sensors that enjoy well established fabrication technology. However, the field of optical fiber sensors has grown enormously and there are great potential that optical fiber humidity sensors can advantageously compete with their electronics counterparts.

In Chapter 3, two different approaches have been used in the fabrication of optical fiber humidity sensor probes; a tapered fiber and etched fiber Bragg grating (FBG). Both sensors are based on the interaction of evanescent wave with the surrounding. They are coated with a polymer blend of hydroxyethylcellulose/ polyvinylidene fluoride (HEC/PVDF) composite to increase the sensitivity. A combination of HEC and PVDF are choosing as a coating material for the sensor probe since they are relatively common and inexpensive. Furthermore, the mesh polymer gel has a good absorption of water in the air. This material was slowly dropped onto these sensor probes by using syringe and left to dry for 48 hours. However, both tapered fiber and etched FBG structures are susceptible to the air turbulence and the pollution of dust and moisture when exposed to air. The dust or moisture on the tapered or etched fiber may introduce loss to the

transmission. Chemical etching techniques also may influence by some environmental perturbations such as the vibration, temperature change and impurity in etchant solution. Finally, in order to manufacture the FBG, the special equipment is needed which increase the cost of sensor's fabrication.

In this section, a RH sensor is proposed and demonstrated using a dumbbell shape inline MZI coated with HEC/PVDF composite. The measurement is based on interferometric technique where the transmission spectrum of the reflected light is investigated with respect to changes in RH. This sensor offer a simple in fabrication technique without using dangerous chemical or flame, compact in size and low in fabrication cost.

4.4.1 Experimental arrangement for RH sensor

Figure 4.13 shows the experimental setup for the proposed sensor that detects changes in relative humidity using the fabricated inline dumbbell shaped MZI coated with HEC/PVDF composite. The inline MZI was fabricated from a standard silica SMF, using a fiber stripper, a cleaver and a fusion splicer machine. The fabrication technique was detailed in section 4.2. The completed dumbbell structure used in this experiment was shown in Fig. 4.4 where the diameters of the first and second bulges are approximately around 198 μm and 196 μm respectively. It has a tapered waist of 95 μm with a distance between two bulges is about 1000 μm . The dimensions of the dumbbell shaped structure were controlled precisely by the fusion splicer program, thus the repeatability of fabricating the bulges could be guaranteed. Then, the HEC/PVDF composite solution was prepared using the same procedures as explained in the previous chapter. The prepared solution was slowly dropped onto the MZI structure using a syringe and left to dry for 48 hours.

The input signal from the ASE source operating in 1550nm region is launched into a sensor probe via a 3 dB coupler. The reflected signal from the sensor is then routed into an OSA through the same coupler. The sensor probe is placed in a sealed chamber with a dish filled with saturated salt solution. Exposing the HEC/PVDF composite to the RH changes inside the chamber produces variations in the transmission spectrum. In the experiment, the performance of the proposed sensor was investigated for various changes in relative humidity ranging from 10% to 80% using a humidity meter with a data logging capability.

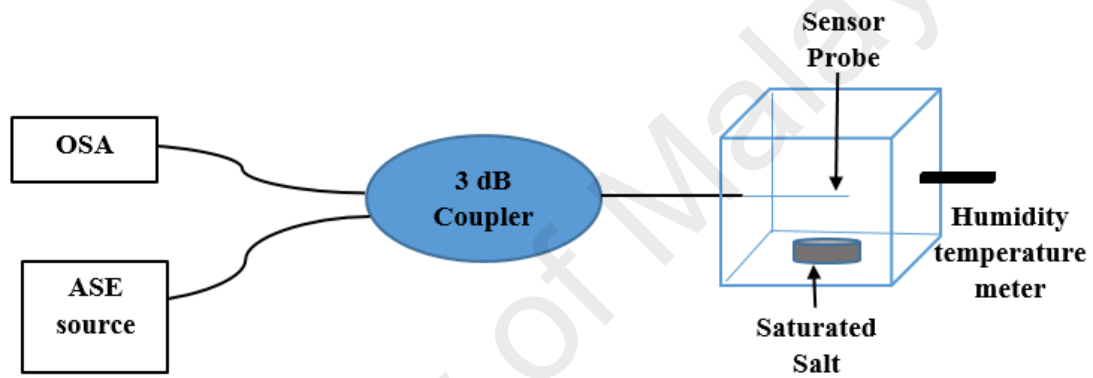


Figure 4.13: The experimental setup for the proposed dumbbell shape MZI based sensor to detect change in RH

4.4.2 Performance of the inline dumbbell shaped MZI based RH sensor

It is observed that both sensor probes generate a comb like reflected spectrum as a broadband ASE is launched into the device. This is attributed to the optical phase difference (OPD) between cladding and core modes, which produces an interference pattern in the MZI. To reduce the influence of vibration on the sensor caused by air-flow, we used saturated salt to change the RH in the testing chamber. The RH in the chamber was varied between 10% and 80% RH under a room temperature of 22°C. At the start of experiment, we use silica gel into the chamber in order to decrease the humidity to 10%.

As the humidity level increased, the transmission spectrum of the probe was recorded by using the OSA. Figure 4.14 shows several measured spectra under different RH levels for the RH sensor configured with the MZI fiber probe. It can be seen that resonant wavelengths of probe red-shifted when the level of relative humidity increased. For instance, the resonant dip wavelength for MZI dumbbell shape increases from 1555.76 to 1556.34 nm as the RH increases from 10 to 80%.

We use a combination of HEC and PVDF as a sensitive material for our probe. This mixture turns into a gel-like material after a long period of agitation, and finally stabilizes and forms into three-dimensional structure of the mesh gel after being coated onto the sensor probe. The mesh gel has a good absorption of water in the air. The response of the sensor to humidity change can be explained as follows. The HEC/PVDF composite in the form of mesh gel absorbs water molecules in its body. The absorbed water molecules increase the average density of the composite that results in an increase of its refractive index. The change of refractive index with different humidity or precipitation of moisture has good reproducibility. As a result, the resonant wavelengths of both sensors coated with the HEC/PVDF shift with RH level change. This is opposed to the trend demonstrated by the uncoated structure where its output spectrum remains constant despite the increase in relative humidity. Similar experimental results are expected if another peak wavelength is used as reference.

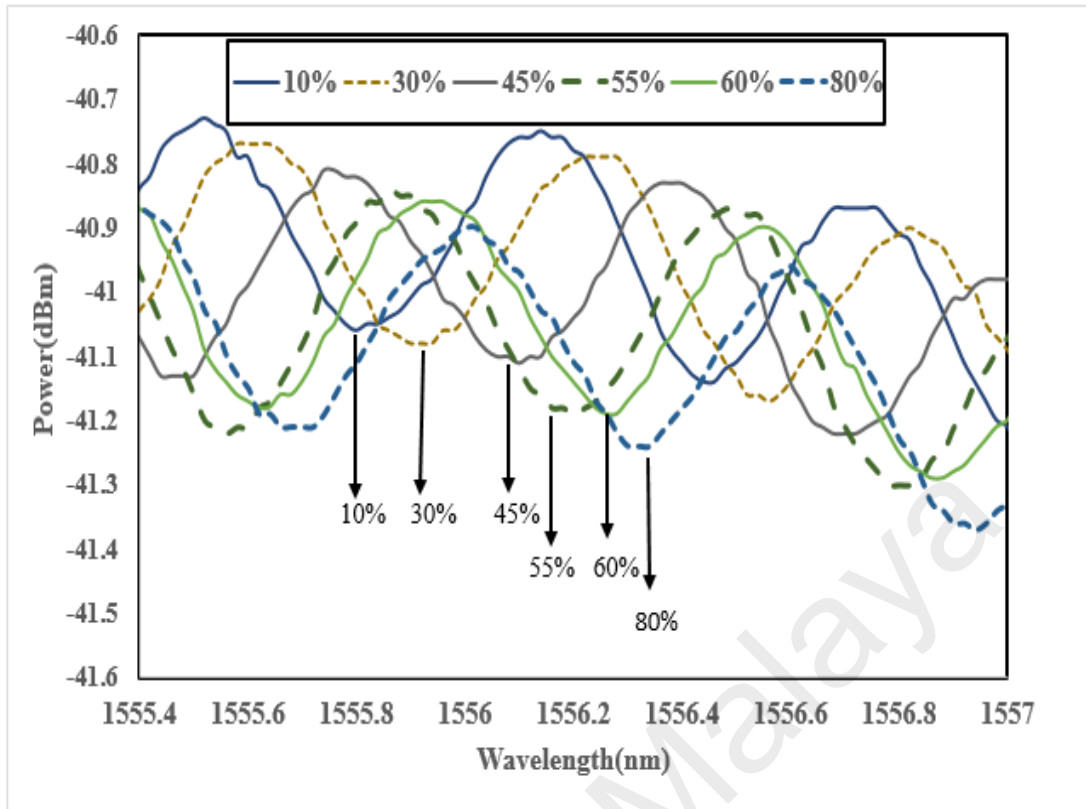


Figure 4. 14: The variation of spectra under different RH levels

Figure 4.15 shows the sensor response to RH measured, which indicates that the resonant wavelength shifts to a longer wavelength as the RH increases. We find that the wavelength increases in a slight quadratic manner with the increase in RH. The square regression coefficient value, which indicates a measure the goodness for the fitting, is 0.973. The considerably high value of the coefficient allows the prediction of unknown relative humidity by the model.

Figure 4.16 shows the linear relationship between humidity and resonant wavelength shift for the sensor. The sensor demonstrated a linear shift from 20 to 45%. It is found that the MZI-based sensor has a sensitivity of 0.0123nm/% with a linearity of 99.88% and limit of detection of 0.44%. The small limit of detection indicates that the dumbbell structure based sensor system has a good efficiency. The sensitivity of the proposed RH sensor is relatively higher than that of the one previously reported RH sensor (Zheng et al., 2013). For instance, the dumbbell structured probe achieves a

sensitivity of 12.3 pm/% RH, which is approximately 7 times more sensitive than the one in (Zheng et al., 2013) with a sensitivity of 1.8 pm/% RH. Compared to intensity based sensors (Batumalay et al., 2013), the proposed sensor is more reliable and practical since it is based on wavelength shift. Figure 4.17 shows the reversibility of MZI-based sensor for two different run. It shows that the proposed sensor is stable and reliable which the different between of two runs is less than $\pm 0.05\text{nm}$. The performance of the proposed dumbbell shaped MZI sensor can be further improved by further optimizing the dumbbell structure and dimension. The proposed sensor has a high potential for RH sensing as it has easy to fabricate, low fabrication cost, and compact size. However, the complete sensing system may require a high precision detector which may increase the overall cost.

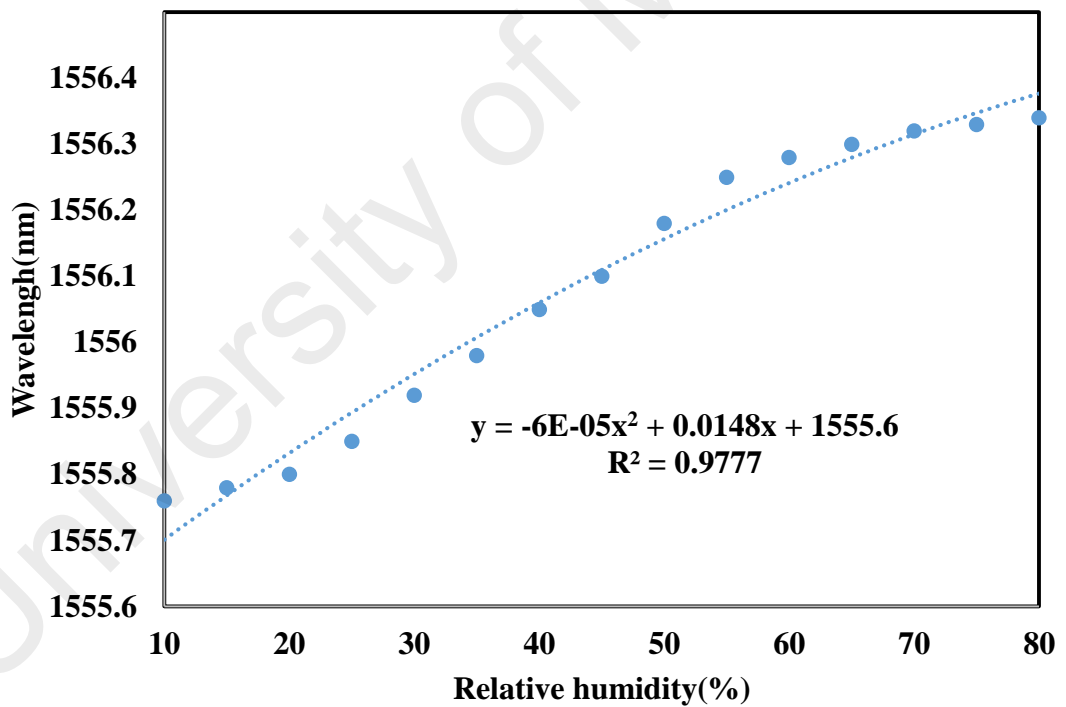


Figure 4.15 : The sensor response to humidity measured using resonant wavelength shift for MZI dumbbell structure.

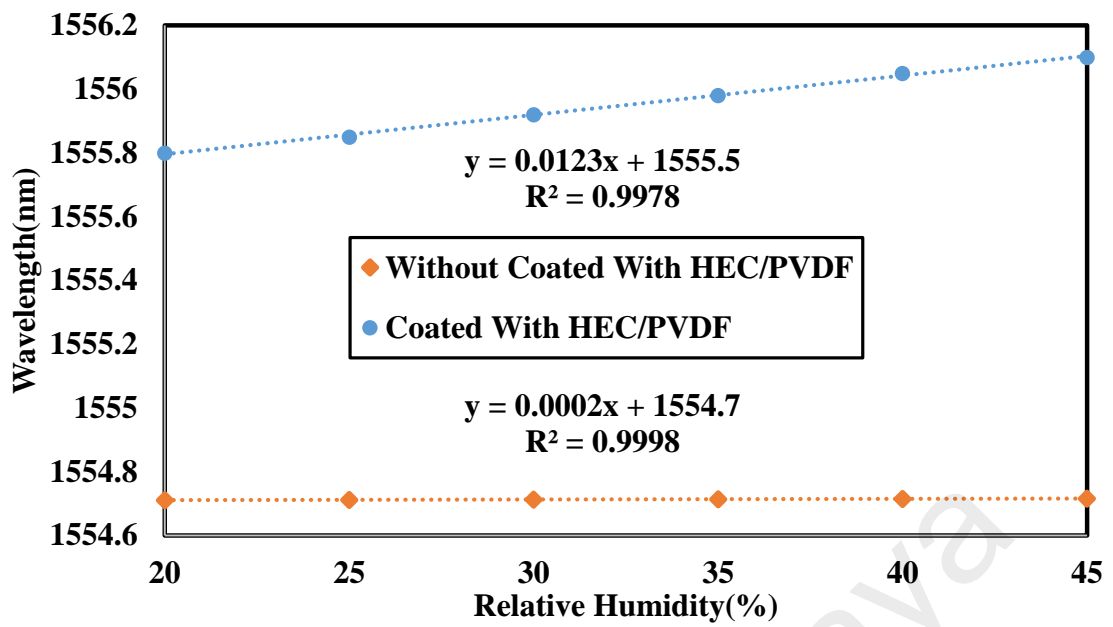


Figure 4.16: The linear relationship between humidity and resonant wavelength shift

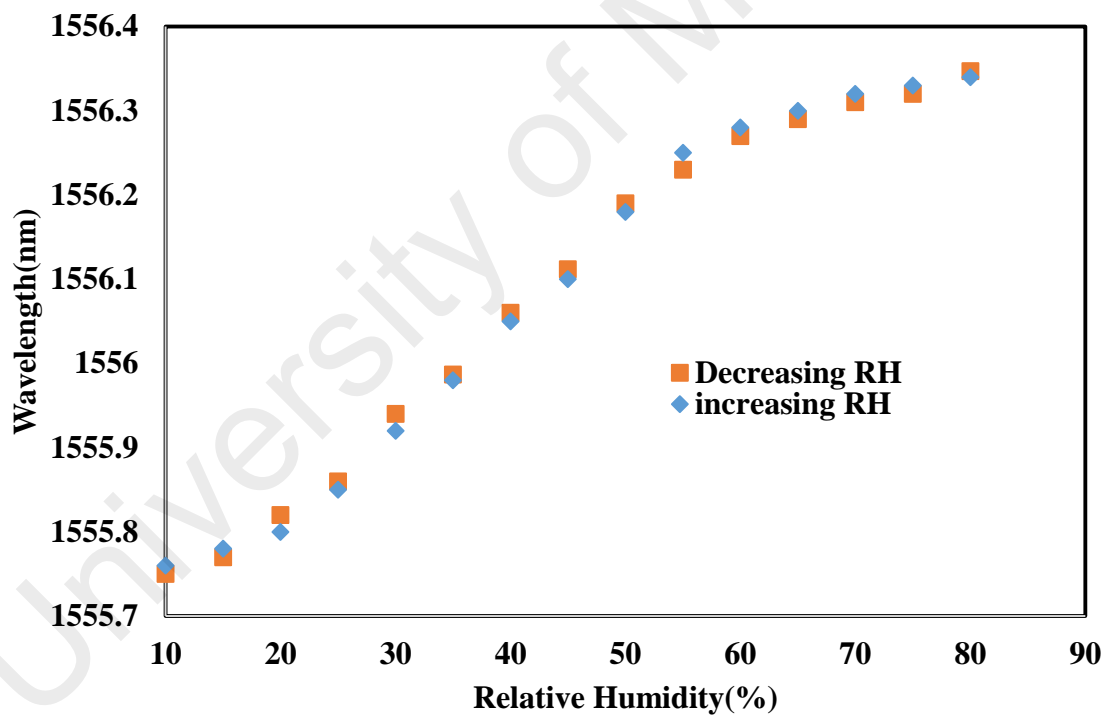


Figure 4.17: The reversibility of MZI-based sensor for two different runs

4.5 Dumbbell shape MZI for Bio-Chemical detection

Abnormal levels of glucose, sodium and uric acid in human serum and urine indicate several medical complications such as diabetes, high blood pressure, gout, dysfunctional kidney and cardiovascular diseases. Conventional methods developed to detect the levels of these bio-chemicals in human body include liquid chromatography (HPL)(Ferin et al., 2013; N. A. Rahman et al., 2008), enzymatic assay (Thakur & Sawant, 2013) and other electrochemical (Khan et al., 2013) processes. Of late, optical fiber sensors have also been used to detect physical parameters as well as chemical compounds (Gehrich et al., 1986; Mignani & Baldini, 1996). Optical fiber sensors offer many advantages since they are compact, highly sensitive, immune to electromagnetic interference, resistant to corrosion and placid to volatile surrounding.

Optical fiber has been widely used as a probe for various sensing applications such as in measuring refractive index, strain, humidity and temperature (Y. Li, Harris, Chen, & Bao, 2010; Lu et al., 2009; Y. Wang, Yang, Wang, Liu, & Lu, 2010). For instance, in the previous section, inline fiber MZI sensor has been used for monitoring changes in RH. In this section, inline MZI with a dumbbell-shaped structure is used for detecting the concentration of various bio-chemicals such as glucose, sodium and uric acid in distilled water. Compared to intensity-based sensors(Bariain et al., 2000; Malathy Batumalay et al., 2014), the proposed sensor is more reliable and practical since it is based on wavelength shift. It shows a high potential for bio-chemical sensing as it is cheap, simple and compact.

4.5.1 Experimental Set-up

Figure 4.18 shows the setup of the bio-chemical sensing experiment using a dumbbell-shaped MZI probe. The setup is almost similar with the RH sensor of Fig. 4.13, where the input signal from an ASE laser source is launched into the sensor probe via a 3 dB coupler. The reflected signal from the sensor is then routed into an OSA through the same coupler. When the input single mode light beam reaches the first bulge of the sensor probe, it is divided into two parts where the first part continues to propagate in the core, while the other part travels in the cladding of the SMF. Due to the OPD between the core and cladding mode, an interference pattern is established when the two output beams recombine at the output end of the second bulge. The interference pattern is strongly dependent on the refractive index of the surrounding medium.

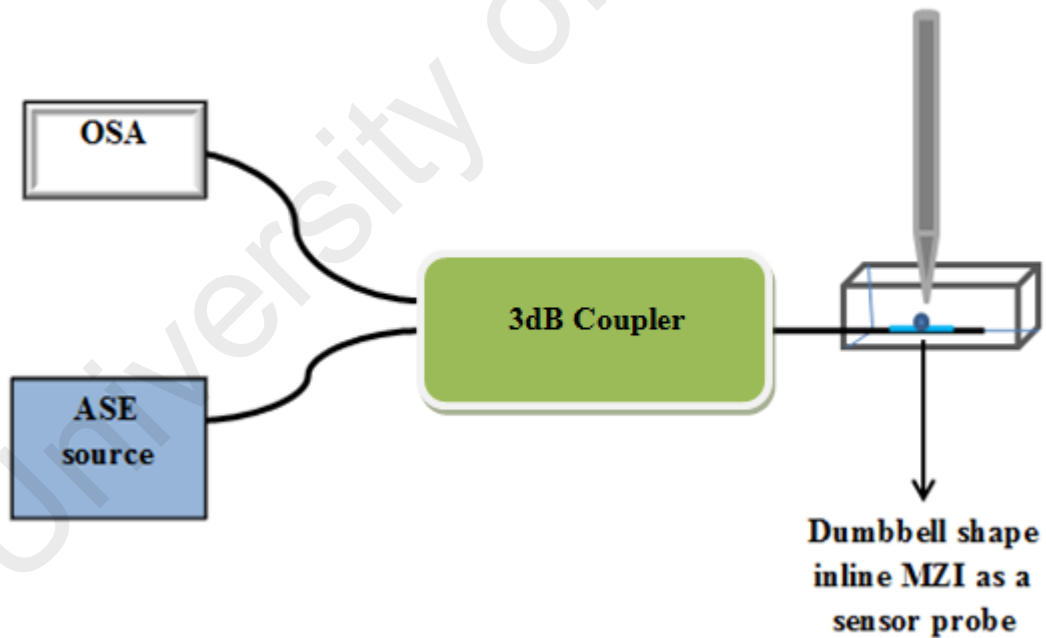


Figure 4.18: The experimental setup of the proposed biochemical sensors

At first, the dumbbell shaped MZI probe is immersed into glucose solution of different concentrations ranging from 0 to 12%. The solution was prepared by mixing glucose and distilled water with different proportions of 0%, 2%, 4%, 8%, 10% and 12%, which corresponds to mixtures with refractive indices of 1.333, 1.336, 1.339, 1.3425, 1.3461, 1.3494 and 1.353, respectively. The solution refractive index is measured using a refractometer. Due to the compact structure of the sensor, a single drop of the liquid solution is enough to surround the whole dumbbell shape. The MZI was cleansed with deionized water and compressed air after each measurement.

Figure 4.19 shows the reflected interference spectrum with the different glucose concentration as the surrounding material. The reflected spectrum is also measured with distilled water (0 % concentration) for comparison purpose. It could be seen that the interference spectrum is red-shifted in the increase of glucose concentration. This is attributed to the increase of the refractive index of the surrounding medium, which reduces the phase difference between the core and cladding modes. It is also observed that the output spectrum from the MZI probe produces an unsmooth curve due to the non-uniqueness of the cladding modes. While the inline MZI is placed in glucose solution, the difference of refractive index between the cladding and glucose solution is big enough to support several cladding modes in the dumbbell structure. All the non-uniqueness cladding modes interfere with the core mode while oscillating inside the dumbbell structure.

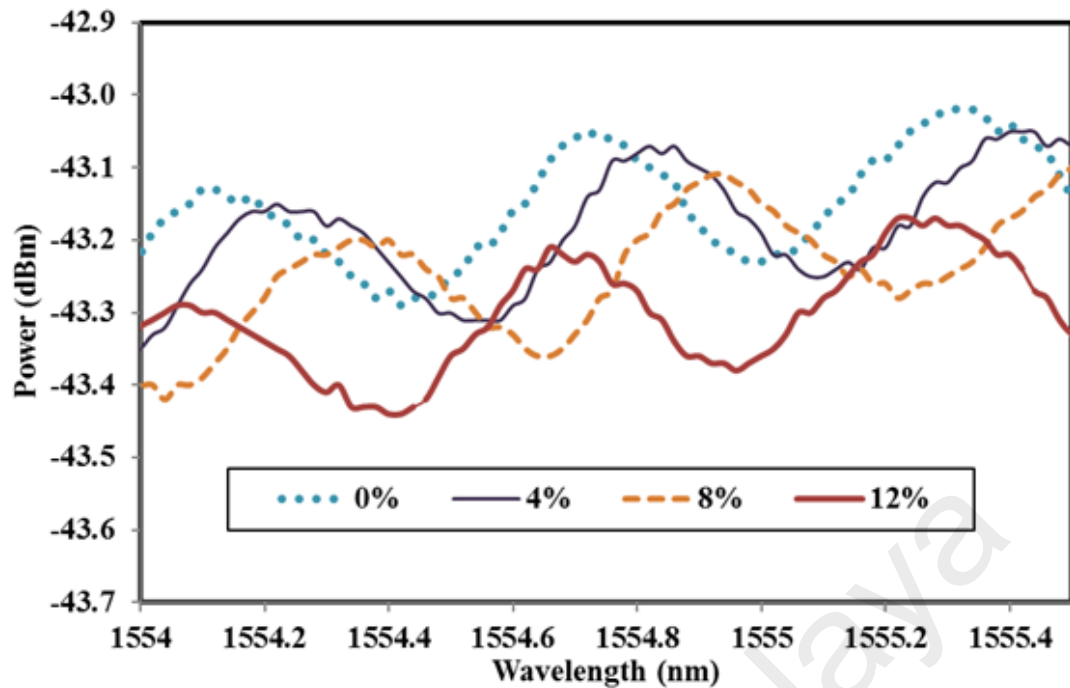


Figure 4.19: Reflected spectrum from the dumbbell shape MZI immersed into various glucose concentrations

The change in the transmission dip wavelength with the increase in glucose concentration is depicted in Figure 4.20. At first the result is fitted with a linear trend where the coefficient of determination is 0.9355. The coefficient presents the goodness of fit such that a high value enables a good prediction of unknown by the model. It is found that the sensor has a sensitivity of 0.04 nm/% with a linearity of 96.7% and the limit of detection of 4.5%. The value of the limit of detection is obtained by dividing the standard deviation of the data with the sensitivity of the sensor.

Since the coefficient of determination is relatively low, a quadratic trend is then added to the graph. We find that the wavelength increases in a slight quadratic manner with the increase in glucose concentration. The adjusted R-square value or the coefficient of determination is 0.9818, which is higher. This is possibly due to the refractive index of the solution, which is slightly quadratically related with the glucose concentration. As the glucose concentration increases from 0 to 12%, the dip wavelength increases from 1554.419 to 1554.939 nm.

The sensitivity and the limit of detection of the quadratic curve are calculated to be 0.0275 nm/% with a linearity of 99.78% and limit of detection of 3.87%.

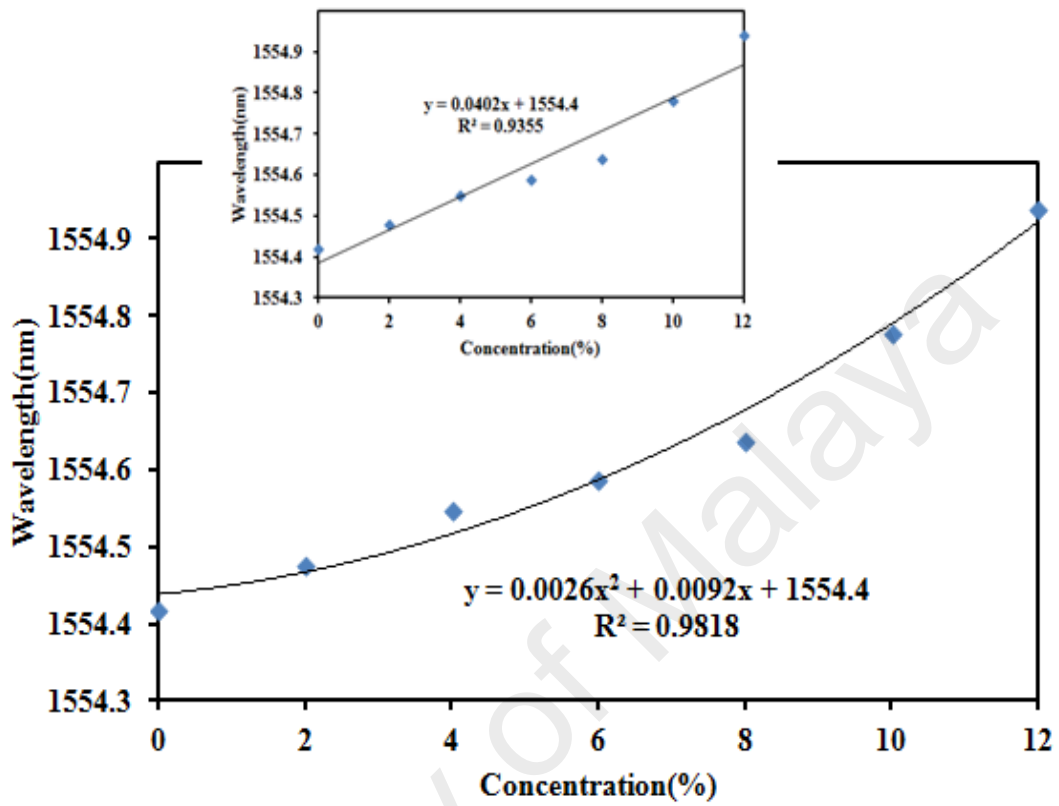


Figure 4.20: The relation between one of the measured dip wavelengths of the interference spectrum and the glucose concentration in distilled water

The experiment was then repeated on Sodium Chloride (NaCl) solutions with different concentrations ranging from 0 % to 12 %. The refractive indices of the solutions were 1.3325, 1.33511, 1.3382, 1.341, 1.3441, 1.3469, and 1.3499 for NaCl concentrations of 0 %, 2 %, 4 %, 8 %, 10 % and 12 %, respectively. Figure 4.21 shows the reflected output spectrum from the MZI at various NaCl concentrations. It can be seen that a change in NaCl concentration causes the interference spectrum of the reflected light to shift. For instance, an increase in the NaCl concentration results in the transmission peak/dip of the spectrum to red-shift due to a higher refractive index of the medium. This is because a higher refractive index reduces the phase difference between the core and cladding mode, resulting in a shift in the free-spectral range of the interference spectrum and subsequently increasing the transmission peak or dip wavelength of the comb spectrum.

Figure 4.22 show the operating wavelength of one of the transmission dips of the comb spectrum against different sodium chloride concentration. The sensitivity is obtained at 0.033 nm/% and the slope shows a good linearity of more than 99% for a 4.32% limit of detection. The results indicate a linear relationship between the signals reflected from the MZI as a function of the concentration of the sodium chloride. We may conclude that an increase in sodium chloride concentration can be detected by observing the shift in the comb spectrum due to the change of medium's refractive index, which increases as its concentration rises.

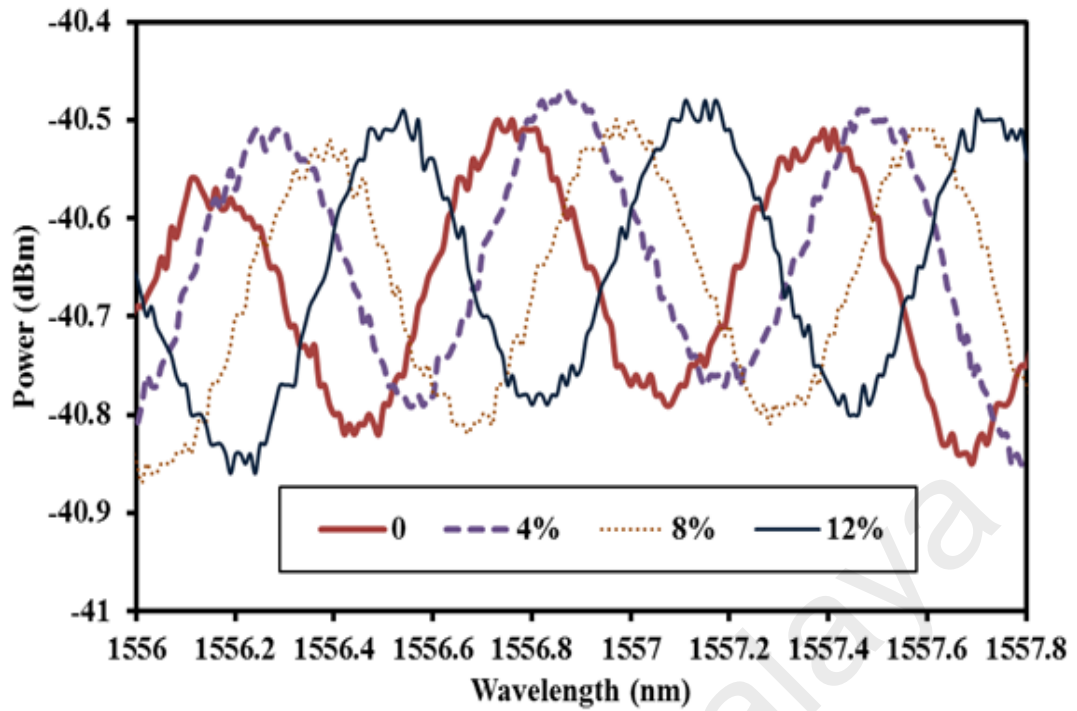


Figure 4.21: The measured dip wavelength of the interference spectrum against the sodium chloride concentration in distilled water

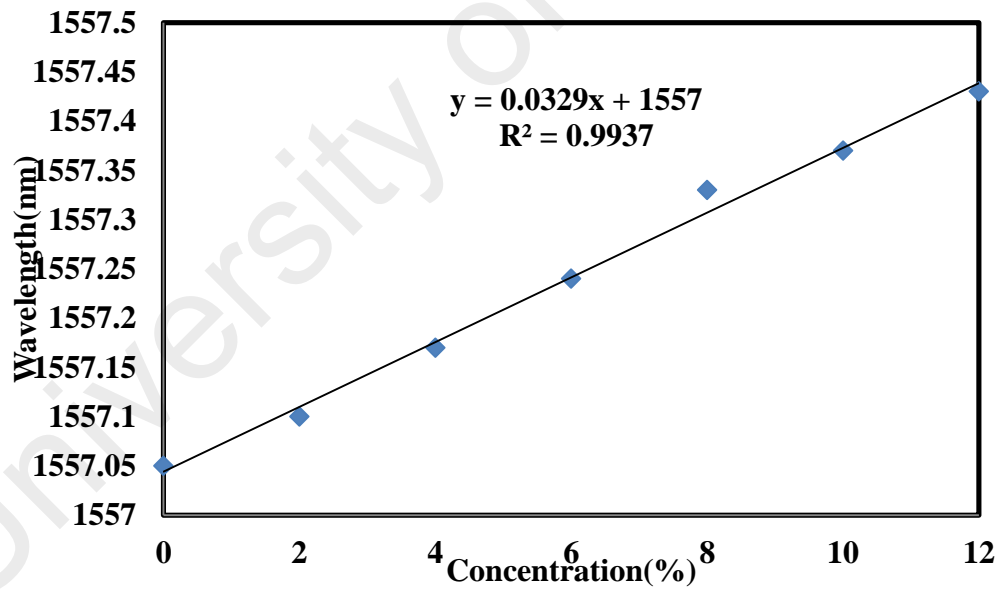


Figure 4.22: The measured dip wavelength of the interference spectrum against the glucose concentration in distilled water

Lastly, the experiment was repeated with uric acid of various concentrations ranging from 0 to 500 ppm. The refractive indices of the solutions were 1.333, 1.3331, 1.3332, 1.3334, 1.3335 and 1.3336 at concentrations of 0ppm, 100ppm, 200ppm, 300, 400ppm and 500ppm respectively. Figure 4.23 shows the output comb spectrum of the

sensor at various uric acid concentrations. As expected, the interference spectrum of the output is also red-shifted when the concentration of uric acid rises from 0 to 500 ppm. The wavelength change of one of the transmission dips with the increase in uric acid concentration is depicted in Figure 4.24. As observed, the dip-wavelength shift linearly increases as the concentration of the uric acid of the solution increases. The sensitivity is obtained at 0.0006 nm/% and the slope shows a good linearity of more than 99.48% for a 7.52% limit of detection.

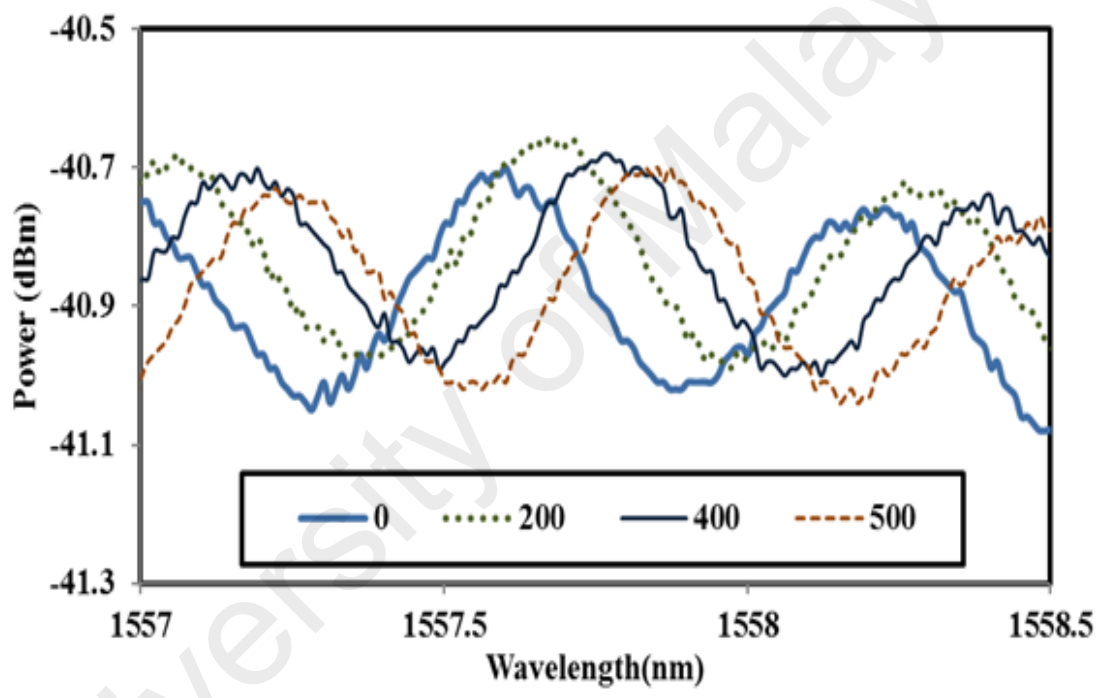


Figure 4.23: The output comb spectrum of the sensor at various uric acid concentrations in DI water solution

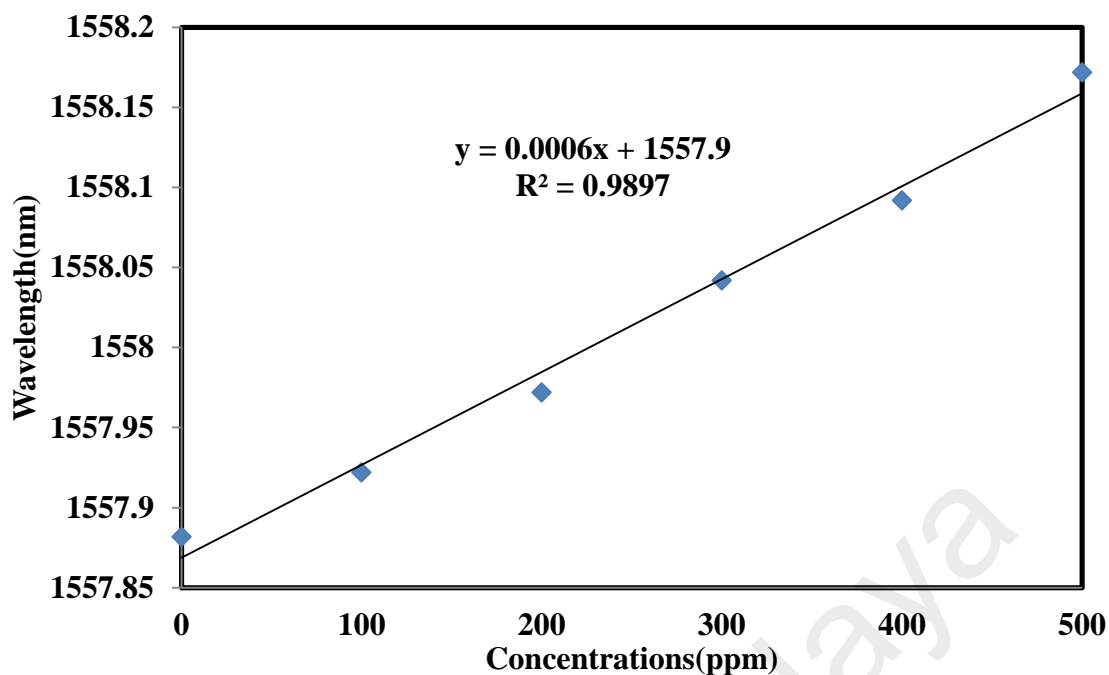


Figure 4.24: The wavelength change of one of the transmission dips with the increase in uric acid concentration

The sensor performance is then summarized in Table 4.2. Overall, the sensor is observed to be sufficiently stable with a standard deviation ranging from 3.87 to 7.52 % with a linearity of more than 99%. Throughout the experiment, a fixed quantity of liquid solution was placed in the petri dish and the corresponding dip wavelength was measured by using an OSA. The results show that the proposed sensor is applicable and useful for bio-chemical detection due to its ability to provide real time bio-chemical detection and control of various mixtures continuously. This preliminary results show that the proposed dumbbell shaped MZI probe can be used as a refractive index sensor.

Table 4.2: Performance of Bio-Chemical Sensors

Parameter	Glucose	NaCl	Uric Acid
Sensitivity	0.0402%	0.0329	0.0006
Linear Range	0-12%	0-12%	0-500ppm
Linearity	96.72%	99.68%	99.48%
Limit of Detection	4.5%	4.32%	7.52%

4.5.2 Effect of Temperature on Bio-Chemical Sensing

One of the factors that affect the performance of the sensor and the characteristic of the sensing medium is temperature. To investigate the effect of temperature on the sensor, an experiment was carried out where the glucose NaCl and uric acid concentrations were fixed at 6%, while the concentration of uric acid was fixed at 200 ppm. Then; the temperature was increased from 30⁰ C to 50⁰ C in 5⁰C step. The results of the experiment are shown Figures 4.25, 4.26 and 4.27 for glucose, NaCl and uric acid solutions, respectively. It is observed that the interference spectra of the output for all three chemical sensors are red-shifted as the temperature increases. The changes of transmission wavelength dip against the temperature are shown in Figure 4.28. It observed that for all cases the wavelength shift linearly increases with the temperature.

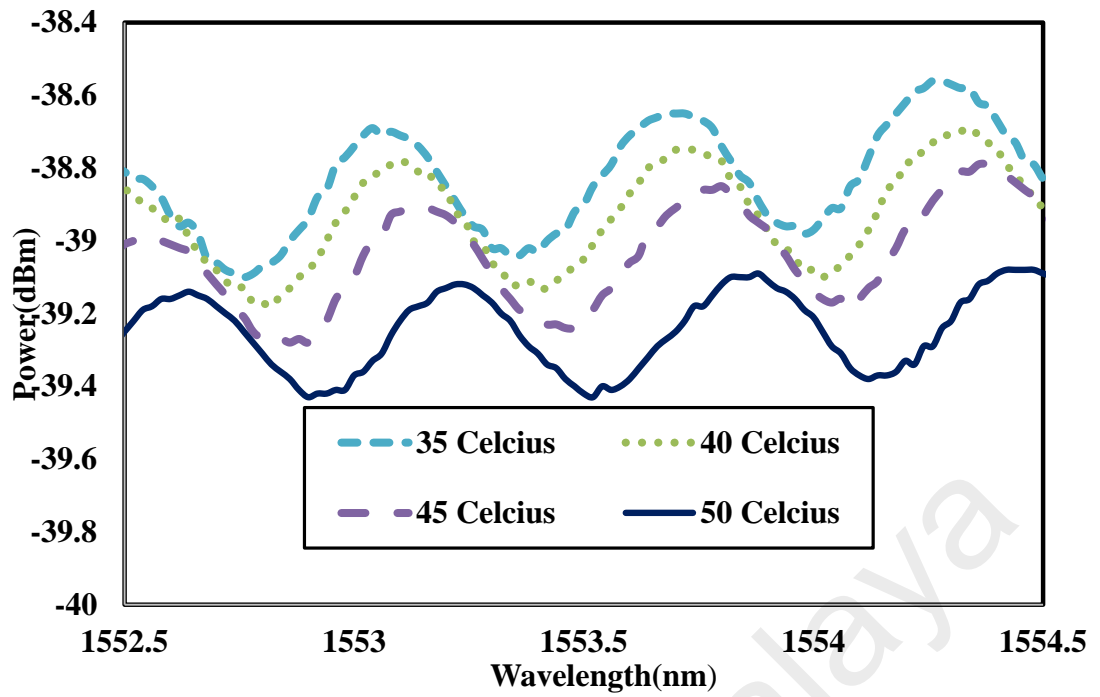


Figure 4.25: The effect of temperature on glucose solution

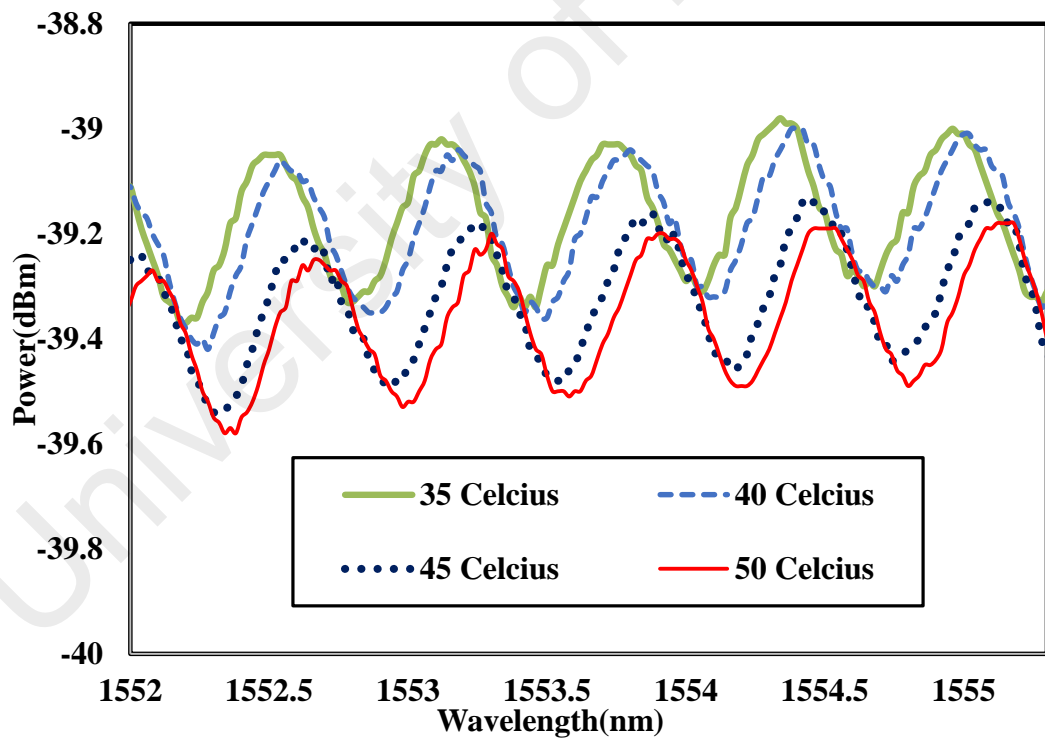


Figure 4.26: The effect of temperature on NaCl solution

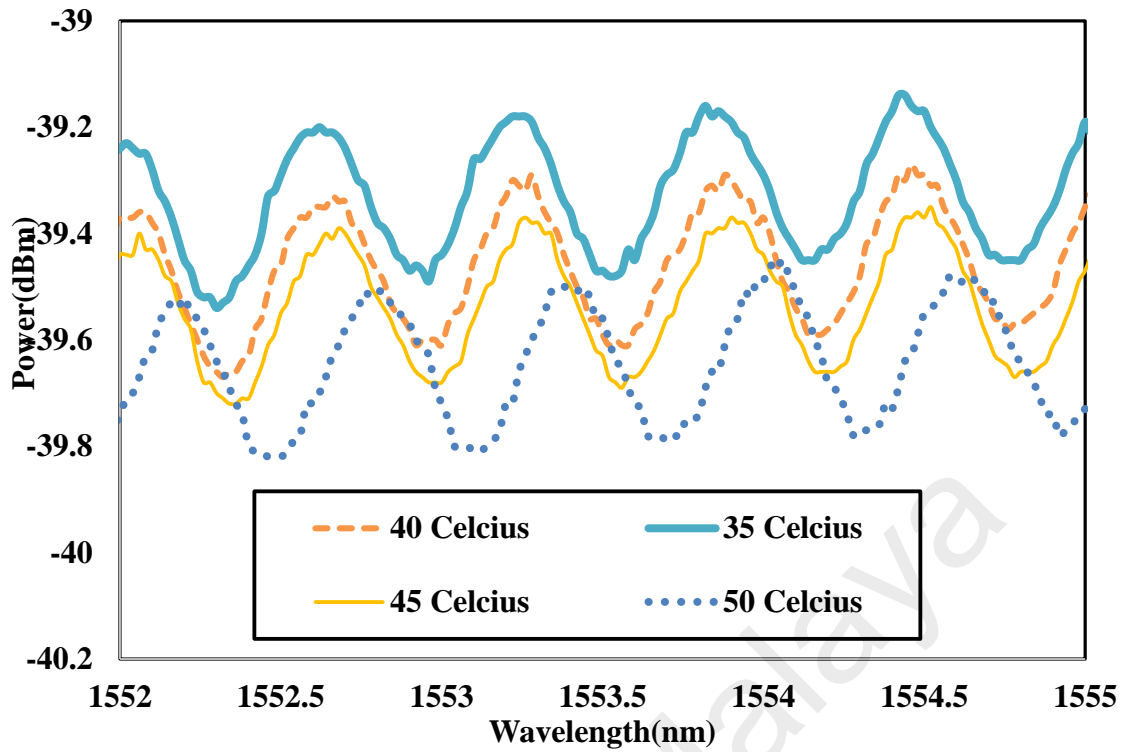


Figure 4.27: The effect of temperature on uric acid solution

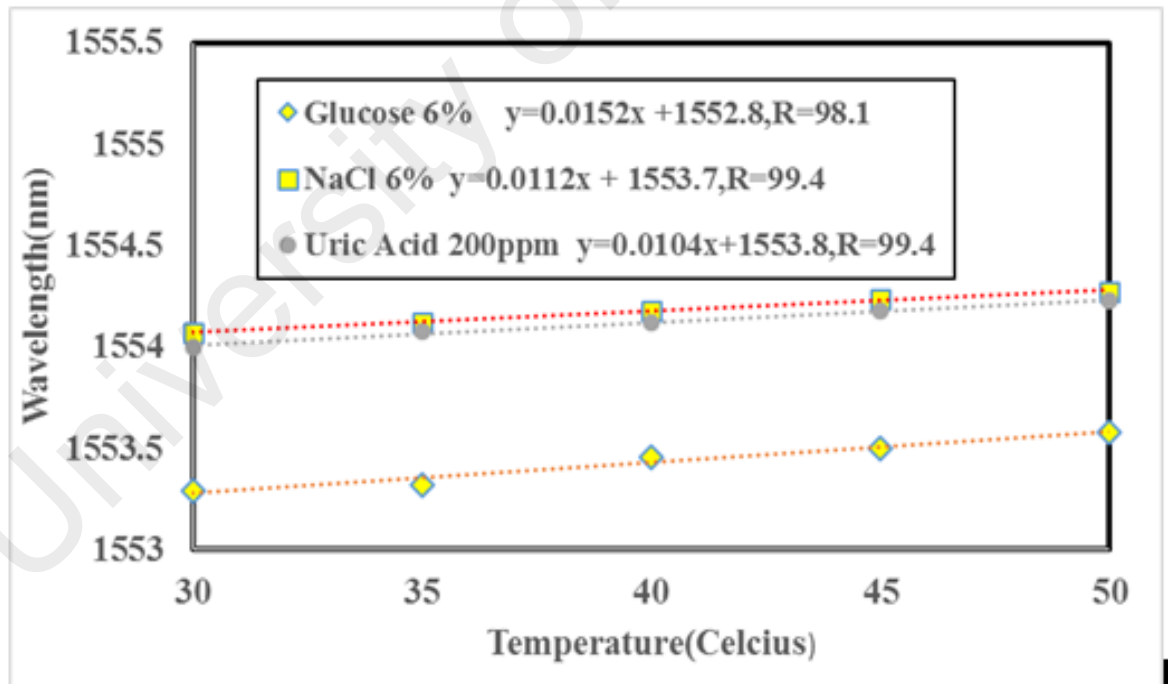


Figure 4.28: The wavelength change of one of the transmission dips with the increases of temperature

4.5.3 Multiple Linear Regression Analysis using SPSS Statistics software

Since the wavelength shift is linearly dependent on both concentration and temperature of bio-chemical solutions, a multiple linear regression (MLR) was used to combine them in single equation. The MLR analysis was performed by using SPSS Statistics software where the dependent variable is wavelength shift and the independent variables are the biochemical concentration and temperature. A general MLR model is normally written as:

$$y_i = \beta_0 + \beta_1 X_{i1} + \dots + \beta_n X_{in} \quad i=1,2,\dots,K \quad (4.5)$$

where y_i is the dependent variable, X_i are independent variables, β_0 is a constant, β_1 and β_n are coefficients of independent variables respectively. By analyzing the data, the β coefficient values are obtained. The models that relate the dip wavelength shift to biochemical concentration and temperature for glucose, NaCl and uric acid are given by equation 4.6, 4.7 and 4.8 respectively:

$$y_{glucose} = 0.046 + (0.040 \times \text{Concentration}) - (0.004 \times \text{Temperature}) \quad (4.6)$$

$$y_{NaCl} = 0.071 + (0.031 \times \text{Concentration}) - (0.004 \times \text{Temperature}) \quad (4.7)$$

$$y_{UricAcid} = 0.162 + (0.001 \times \text{Concentration}) - (0.004 \times \text{Temperature}) \quad (4.8)$$

Table 4.3 summarizes the result of the analysis. It is found that the P-value for all biochemical sensors are less than 0.05 significance level.

Table 4.3: The summary of test analysis

Dependent Variable	Bio Chemicals	Independent Variables	P-value
Wavelength shift(nm)	Glucose	Concentrations	0.000
		Temperatures	0.040
Wavelength shift(nm)	NaCl	Concentrations	0.000
		Temperatures	0.005
Wavelength shift(nm)	Uric acid	Concentrations	0.012
		Temperatures	0.042

4.6 Summary

A new dumbbell-shaped inline MZI has been successfully developed using an arcing process of a fusion splicer for RH measurement and detecting bio-chemical concentration in distilled water. The sensor probe consists of two bulges separated by a tapered waist that generates a good reflected interference spectrum. Since the two bulges act as a beam splitter and combiner, changes in their diameters (or thickness) lead to the change in output transmitted interference spectrum. It is observed that the bigger bulge diameter produced the higher ER, while the longer separation length produced the lower FSR. At first, a new evanescent wave based sensor is proposed and demonstrated using a dumbbell structure coated with HEC/PVDF composite for RH measurement. It is observed that the resonant dip wavelength for MZI dumbbell shape increases from 1555.76 to 1556.34 nm as the RH increases from 10 to 80%. This sensor demonstrated a linear shift especially within a range from 20 to 45% with a sensitivity of 0.0123nm/%, linearity of 99.88% and limit of detection of 0.44%. The inline MZI is also used for detecting bio-chemical concentration in distilled water. The interference spectrum is red-shifted with the increase of bio-chemical concentration due to the increase in the

refractive index of the surrounding, which reduces the phase difference between the core and cladding modes. For instance, as the glucose concentration increases from 0 to 12%, the dip wavelength is red-shifted from 1554.419 to 1554.939 nm in a quadratic manner with the coefficient of determination of 0.9818. It is also found that the sensor has a sensitivity of 0.0402nm/% with a linearity of 96.72% and limit of detection of 4.5%. For NaCl solution, the dip-wavelength shift is linearly proportional to the increase of the concentration of the sodium chloride solution or salinity. The sensitivity is obtained at 0.0329 nm/% and the slope shows a good linearity of more than 99.68% for a 4.32% limit of detection. Lastly, for uric acid, the sensitivity is obtained at 0.0006 nm/% and the slope shows a good linearity of more than 99.48% for a 7.52% limit of detection.

Additionally, to investigate the effect of temperature on the sensor, an experiment was carried out where the glucose NaCl and uric acid concentrations were fixed at 6%, while the concentration of uric acid was fixed at 200 ppm. Then the temperature was increased from 30⁰ C to 50⁰ C in 5⁰C step. It is observed that the interference spectra of the output for all three chemical sensors are red-shifted as the temperature increases. Also, it found that for all cases the wavelength shift linearly increases with the temperature. Since the wavelength shift is linearly dependent on both concentration and temperature of bio-chemical solutions, a multiple linear regression (MLR) was used to combine them in single equation. The MLR analysis was performed by using SPSS Statistics software. From statistical analysis, it is found that the P-value of all biochemical sensors are less than the specified significance level of 0.05. Thus, it can be concluded that both concentration and temperature influence the spectrum shift of the output. It can be concluded that the proposed dumbbell shape MZI sensor has a high potential for RH sensing and bio-chemical concentration detection as it has easy to fabricate, low fabrication cost, and compact size.

CHAPTER 5: INLINE MACH-ZEHNDER INTERFEROMETER (IMZI) WITH ZNO NANOWIRES COATING FOR THE MEASUREMENTS OF HUMIDITY AND URIC ACID CONCENTRATIONS

5.1 Introduction

Nanotechnology is a technology that involves with small structures or small sized materials. The typical dimension spans of the structure should be in a range from sub-nanometer to several hundred nanometers. The physical properties of materials in micrometer are mostly similar to those in bulk form. However materials in nanometer scale may exhibit physical properties that are distinctively different from those of bulk. Suitable control of the properties of nanometer-scale structures can lead to new science as well as a new devices and technologies. In general, nanotechnology could be defined as a technology of designing, fabricating and applying nanostructures. Nanotechnology also includes fundamental understanding of physical properties and phenomena of nanomaterial and nanostructures. Study on the fundamental relationships between physical properties, phenomena and material dimensions in the nanometer scale, is also referred to as nanoscience.

There has been an explosive growth of nanoscience and nanotechnology in the last few years, primarily because of the availability of new strategies for the synthesis of nanomaterial and new tools for characterization and manipulation. Several methods of synthesizing nanoparticles, nanowires and tubes, and their assemblies have been discovered. On the other side, a wide variety of nanostructures such as nanowires, nanotubes and nonporous material have also attracted a great interest to researchers due to its unique advantages (Arregui, 2009). Nanostructured materials are a new class of materials which provide one of the greatest potentials for improving performance and extending capabilities of products in a number of industrial sectors, including the

aerospace, tooling, automotive, recording, cosmetics, electric motor, duplication, and refrigeration industries.

The discovery of carbon nanotubes (CNTs) (Iijima, 1991) has generated great interest among researchers to develop high performance devices. Carbon is a unique material and can be good metallic conductor in the form of graphite, a wide band-gap semiconductor in the form of diamond or a polymer when reacted with hydrogen. The ongoing exploration on electrical, physical, chemical and mechanical properties contributes a wide range of applications such as nanoelectronics, sensors, field emission and electrodes. The electrical properties of CNTs are extremely sensitive to charge transfer and chemical doping effects by various molecules. Recently, Malathy et al (Malathy Batumalay et al., 2014) has demonstrated a tapered plastic optical fiber (POF) coated with single wall carbon nanotubes polyethylene oxide (SWCNT-PEO) composite for measurement of uric acid concentration. It was shown that the SWCNT-PEO coating has increased the conductance characteristic of the fiber and thus useful for applications such as electrical chemical sensors.

The discovery of nanostructures Zinc Oxide (ZnO) in 2001 has also generated a great interest in the development of various high performance devices such as nanoelectronics, sensors, field emission and electrodes (Gusatti et al., 2011). ZnO is a unique material that exhibits semiconducting, piezoelectric, and pyroelectric multiple properties. Using a solid-vapor phase thermal sublimation technique, ZnO nanocombs, nanorings, nanohelices/nanosprings, nanobows, nanobelts, nanowires, and nanocages have been synthesized under specific growth conditions (Liu et al., 2007; Viswanathan & Gupta, 2003; Yao et al., 2007). These nanostructures attracted great interest to researchers due to its unique advantages in combination with immobilized enzymes and can enhance the direct electron transfer between the enzyme's active sites and the electrons (Ali et al., 2012). In the previous work, ZnO nanowires grown on the surface of gold coated flexible

plastic substrate has been demonstrated as a good uric acid biosensor (Ali et al., 2011). Batumalay et al. (M Batumalay et al., 2014) has also demonstrated both humidity and uric acid biosensors by using tapered POF coated with ZnO nanorods,

Silica optical fiber has received much attention in recent years for sensing applications as described in the previous chapters. We have demonstrated various fiber based sensors for measuring humidity, refractive index (RI) and temperature in the previous chapters. Compared to conventional sensors based on mechanical and electrical properties, optical fiber sensors offer many advantages such as compactness, high sensitivity, immunity to electromagnetic interference and volatile surrounding and resistance to corrosion. In the previous chapters, various sensor probes based on inline Mach-Zehnder interferometer (IMZI) have been proposed and demonstrated. We have also coated the IMZI probe with HEC/PVDF to increase the sensitivity of our previous sensors such as humidity. In this chapter, the dumbbell shape IMZI coated with ZnO nanowires is demonstrated for both humidity and uric acid sensors. A new approach has been employed in the ZnO coating process to reduce the cost.

5.2 Synthesis of Zinc Oxide Nanostructure

ZnO is representative of II–VI semiconductor compounds, is a very versatile and important material. It has a unique position among semiconducting oxides due to its piezoelectric and transparent conducting properties. ZnO has a wide band gap (3.37 eV) and a large exciton binding energy (60 meV). A wide band gap has many benefits like enabling high temperature and power operations, reducing electronic noise, making sustenance in large electric fields possible and raising breakdown voltages. Recently, various synthesis techniques have been developed to fabricate ZnO nanocrystals with different shapes, which include metal-catalyzed vapour-liquid-solid (VLS) growth,

physical vapour deposition (PVD), chemical vapour deposition (CVD), metal-organic vapour-phase epitaxy, metal-organic CVD, template-assisted growth and oxidation method (Arregui, 2009; Subramanyam et al., 2000; Yawong et al., 2005). Many of these techniques however are complicated needing a high temperature for synthesis and also have a long reaction time. Apart from this, these techniques also utilize toxic components and require expensive experimental setup.

The oxidation method on the other hand is a simple low-cost technique and very commonly used for the synthesis of ZnO nanostructures. ZnO nanostructures have been successfully made by oxidizing Zn foils at 700°C in air without the presence of a catalyst and carrier gas (Kissinger, 1957). Sekar and co-workers (Sekar et al., 2005) reported that ZnO nanowires were grown on Si (100) substrates by oxidation of metallic Zn powder at 600°C. As shown in Figure 2.9, the synthesized ZnO materials have been found to have rod like, belt like, wire like and needle like morphologies. This route for synthesis of ZnO is inexpensive as it uses the oxygen from the air (Liu et al., 2007; Viswanathan & Gupta, 2003; Yao et al., 2007). Here an economical and environment friendly route has been used for the synthesis of ZnO by using a sol-gel immersion method.

Figure 5.1 shows a flow chart which explains the step by step procedure to prepare the ZnO composite. Firstly, aqueous solution of zinc nitrate hexahydrate ($\text{Zn}(\text{NO}_3)_2 \cdot 6\text{H}_2\text{O}$ (0.01 M) and hexamethylenetetramine (HMTA; $\text{C}_6\text{H}_{12}\text{N}_4$) (0.01 M) are prepared by mixing the powder with deionized (DI) water. Then, the mixture was stirred at 60°C for 2 hours to obtain a clear homogeneous ZnO aqueous solution and then, the solution was kept for 24 hours prior to fiber coating process (Figure 5.2).

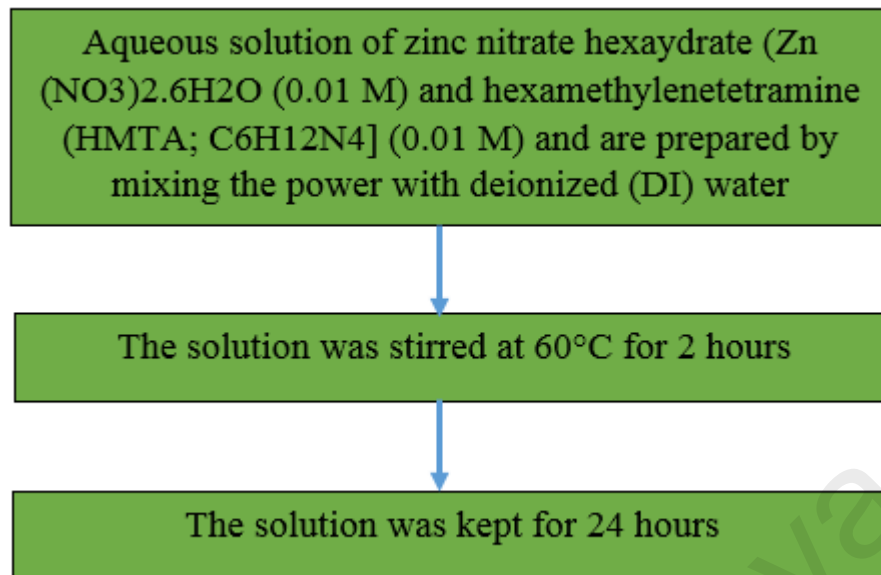


Figure 5.1: The procedure to prepare the ZnO composite



Figure 5.2: The ZnO solution was kept for 24 hours before use

Next, the IMZI structure was manually dipped into the ZnO solution and was dried at 60°C to evaporate the solvent and to remove organic residuals. This coating and drying method was repeated for five times to increase the thickness of the coating layer. The dumbbell shaped sensor probe was then characterized using Field Emission Scanning

Electron Microscope (FESEM) to investigate the morphology of the ZnO nanowires coat on the tapered waist. Figures 5.3 (a) and (b) show the microscope and FESEM images of the sensor probe respectively. As seen in the figure, high density of ZnO nanowires was grown on the tapered waist of the IMZI. The ZnO nanowires coating is expected to enhance the ability of the probe for sensing applications.

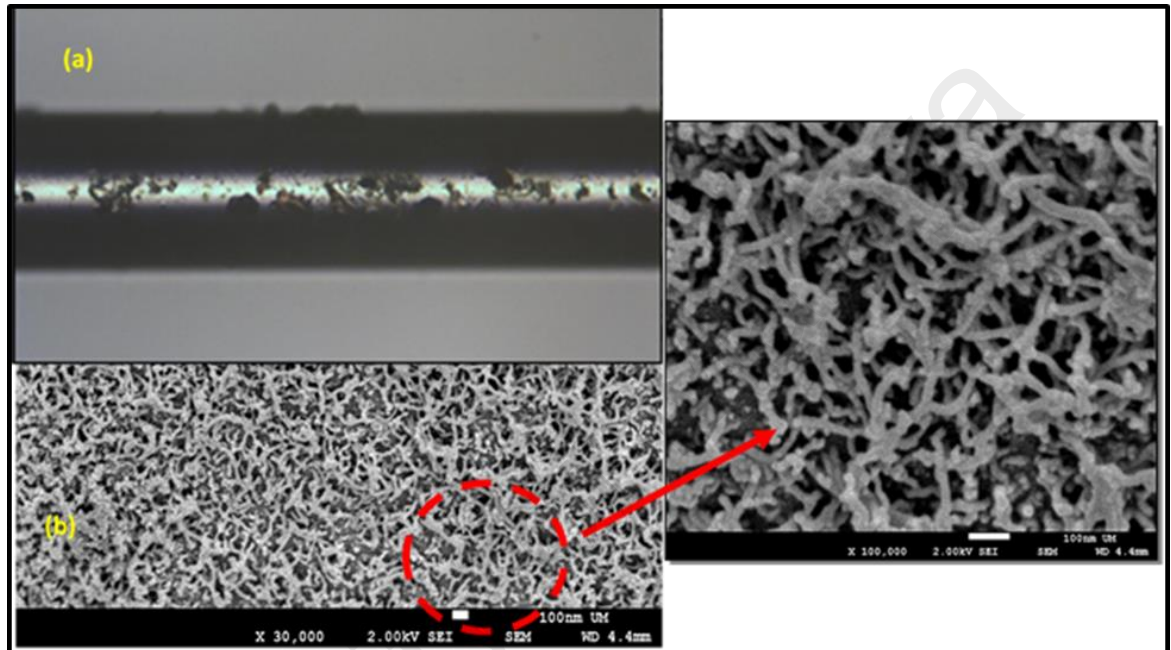


Figure 5.3: Microscope and FESEM images of the sensor probe coated with ZnO

5.3 Relative Humidity (RH) Sensor Based on Inline Mach Zehnde Interferometer with ZnO Nanowires Coating

Humidity monitoring is crucial in numerous industries like mining, chemical and biomedical plants as it may affect product quality and workers' health. It is also important in the prevention and control of corrosion in big structures such as bridges or planes (Sun et al., 2009). Therefore relative humidity (RH) measurement has been extensively studied and a great variety of humidity sensors have been developed and reported in many literatures. In fibre optic humidity sensors, light is guided in and modulated by the fiber core and the surrounding medium and then collected by a detector. Since humidity affects

the refractive index of the surrounding medium, changes in relative humidity affects the transmitted or reflected light that passes through or interacts with the medium.

In Chapter 3, two different approaches have been used in the fabrication of optical fibre humidity sensor probes; a tapered fiber and etched fiber Bragg grating (FBG). Both sensors are based on the interaction of evanescent wave with the surrounding. They are coated with a polymer blend of hydroxyethylcellulose/ polyvinylidene fluoride (HEC/PVDF) composite to increase the sensitivity. Then the same material was used using a dumbbell shape inline MZI coated with HEC/PVDF composite also for RH sensor in chapter 4. In this section, a new optical fiber RH sensor is proposed and demonstrated using a similar structure, but the sensor is coated with ZnO nanowires to improve its sensitivity. The operation of the sensor is based on the interferometric technique where the transmission spectrum of the reflected light is investigated with respect to changes in RH.

Figure 5.4 shows the microscopic image of the IMZI sensor probe used in this experiment. As shown in the figure, it consists of two bulges connected by a tapered waist. In the experiment, a commercial fusion splicer (Sumitomo, Type 39C) was employed to fabricate the bulges on the uncoated standard single mode fiber (SMF). The specific fabrication process was explained in detail in Chapter 4. The pre-fusion and discharge current were kept at default. The pre-fusion and fusion time were set at 0.05s and 1.65 s in the experiments and a large “overlap” parameter of 80 μm was chosen for fusion splicing. The overlap parameter was related to the fiber length fed to the fusion splicing point from both sides to form a bulge. At the splicing point the fiber ends were heated by arc discharge and fused. An enlarged bulge was formed due to repeated fusion of the softened fiber at the same splicing point. By concatenating two such bulges, a dumbbell shaped IMZI was constructed. As shown in Figure 5.4, the fabricated bulges have center waist diameters of 198 and 196 μm with a tapered waist diameter of 95 μm . The distance

of the two bulges is about 1000 μm . The dimensions of the dumbbell shaped structure are controlled precisely by the fusion splicer program, thus repeatability of fabricating the bulges can be guaranteed.

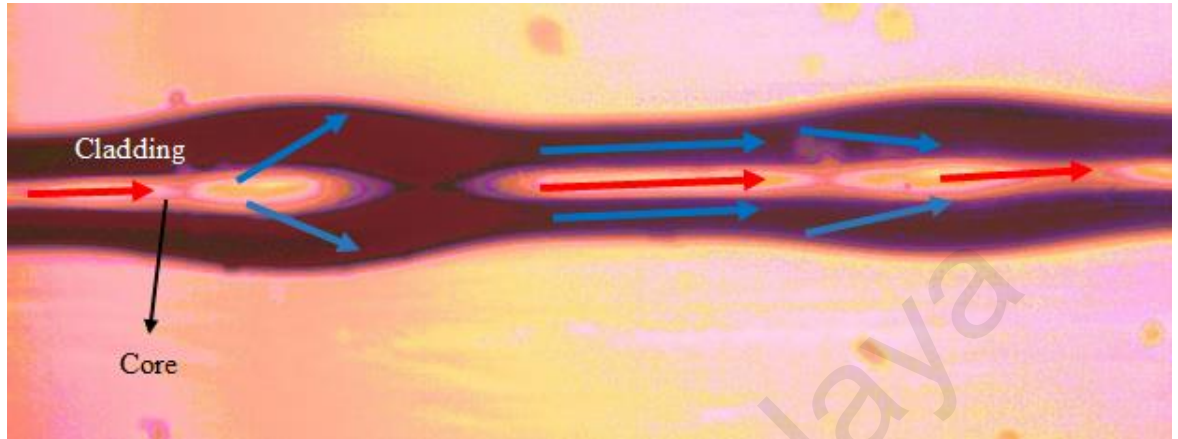


Figure 5.4: The microscope image of the fabricated dumbbell shaped IMZI

The operating principle of the proposed sensor is based on the signal interference between core and cladding modes inside the dumbbell structure. The two bulges act as the beam splitter and beam combiner. The cladding modes are excited by the first bulge and travel in the fiber cladding and surrounding coating layer. The rest of the light energy continues to propagate in the core. Part of the cladding modes are coupled back to the core of the SMF at the second bulge. Therefore, the IMZI is formed due to the optical phase difference between the core mode and the higher-order cladding modes. To utilize the IMZI as an RH sensor, we need to coat it with a suitable material. This material must be able to absorb and desorb water repeatedly. In the previous chapter, polymer blend of HEC/PVDF composite has been used for the coating. Here, we choose ZnO nanowires obtained by a sol-gel immersion method as the sensing material since this nanostructure has its own unique properties (Chen et al., 2012). The coating method and result were explained and reported in the previous section.

Figure 5.5 shows the experimental setup of the proposed sensor that detects changes in relative humidity of a sealed chamber or enclosure. The input signal from the

amplified spontaneous emission (ASE) laser source is launched into a sensor probe via a 3 dB coupler. A homemade ASE source was used from Erbium-doped fiber amplifier operating within a wavelength range from 1520 to 1565 nm in the experiment. The tip of the sensor probe is perpendicularly cleaved to allow 3-4% of the light to be reflected back into the system due to the Fresnel reflection. The reflected signal from the sensor is then routed to an optical spectrum analyzer (OSA, ANDO AQ6330) with resolution of 0.05 nm through the same coupler. The sensor probe is placed in the sealed chamber with a dish filled with saturated salt solution. Exposing the MZI-sensors to the RH variation inside the enclosure produces changes in reflection spectrum. In this experiment, the performance of the proposed sensor was investigated for various changes in relative humidity ranging from 35 to 60% RH using a humidity meter with a data logging capability.

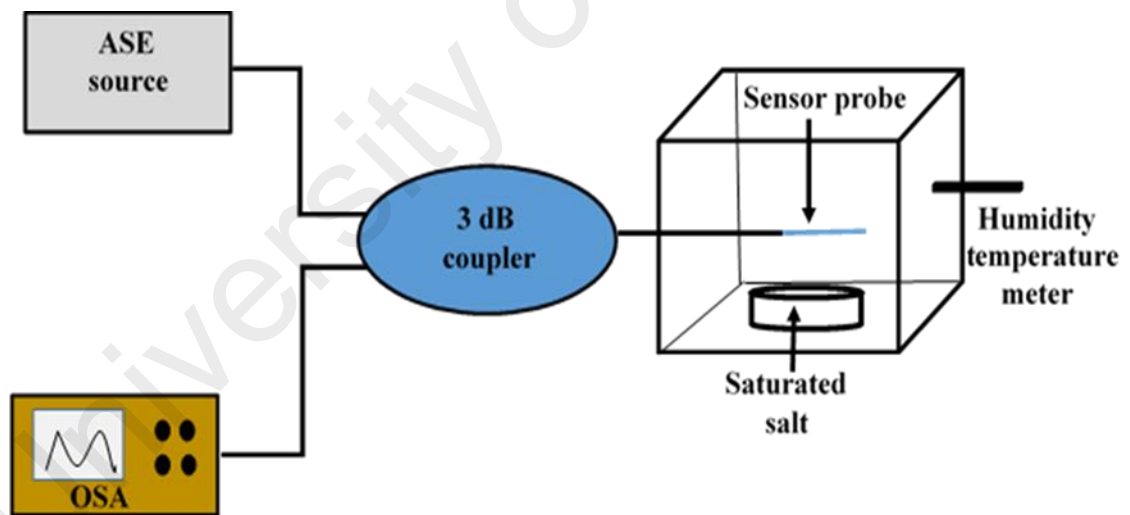


Figure 5.5: The experimental setup for the proposed RH sensor to detect change in RH using the fabricated inline dumbbell shaped MZI coated with ZnO nanowires.

It is observed that sensor probe generates a sinusoidal like reflected spectrum as a broadband ASE is launched into the device. This is attributed to the optical path difference (OPD) between cladding and core modes, which produces an interference pattern in the IMZI. Since the two bulges act as a beam splitter and combiner, changes in surrounding medium refractive index leads to the change in output of reflection spectra. To reduce the influence of vibration on the sensor caused by air-flow, saturated salt was used instead of an air dryer to alter the relative humidity in the testing chamber. The relative humidity in the chamber was varied between 35 %RH and 60% RH under a constant temperature of 22°C. As the humidity level increased, the transmission spectrum of the probe was recorded by an OSA.

Figure 5.6 shows the measured reflected spectra under different RH levels for the RH sensor configured with IMZI. It can be seen that resonant wavelengths of probe is red-shifted when the level of RH increased. For instance, the resonant wavelength of one of the peaks increased from 1553.715 to 1554.205 nm as the RH increases from 35%RH to 60%RH. This is attributed to the increase of the refractive index of the surrounding medium, which reduces the phase difference between the core and cladding modes. Figure 5.7 shows a linear relationship between humidity and resonant wavelength of a peak that is red-shifted for both sensors with and without the ZnO nanowires coating. It could be seen that the sensitivity of the IMZI based sensor improves from 0.0001nm/%RH to 0.0205nm/%RH with the introduction of ZnO nanowires coating on the sensor probe. The spectrum response of the sensor to humidity change can be explained as follows. When the ZnO nanowires is exposed to the high humidity surrounding, water molecules get trapped within the nanowires mesh due to the electrostatic force. Now, the nanowire mesh contains trapped water instead of air. Therefore, the effective refractive index of the ZnO nanowire coating changes linearly with the relative humidity of the ambience. This is due to the refractive index of water (1.333), which is larger than the refractive index of air (1.001). The change in refractive

index of the surrounding alters the path length difference between the core and cladding modes inside the IMZI, which in turn shifts the interference spectrum to a longer wavelength. The performance of the proposed sensor with and without the ZnO nanowire is summarized and compared in Table 5.1.

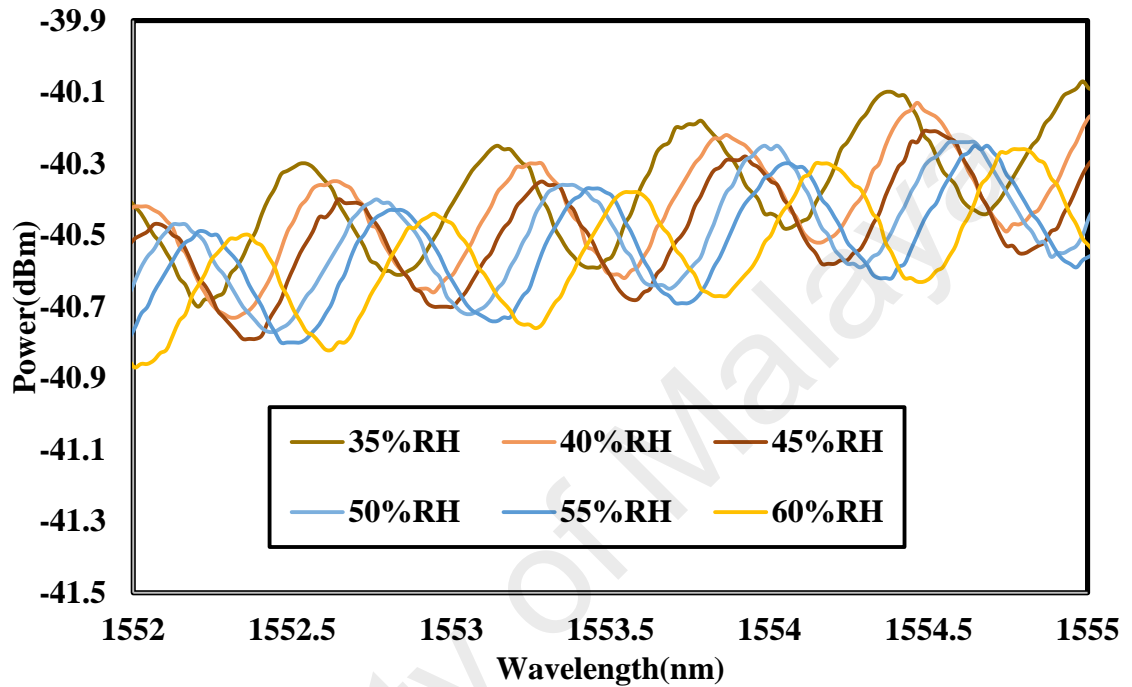


Figure 5.6: The variation of spectra under different RH levels for the RH sensor configured with IMZI fiber probe

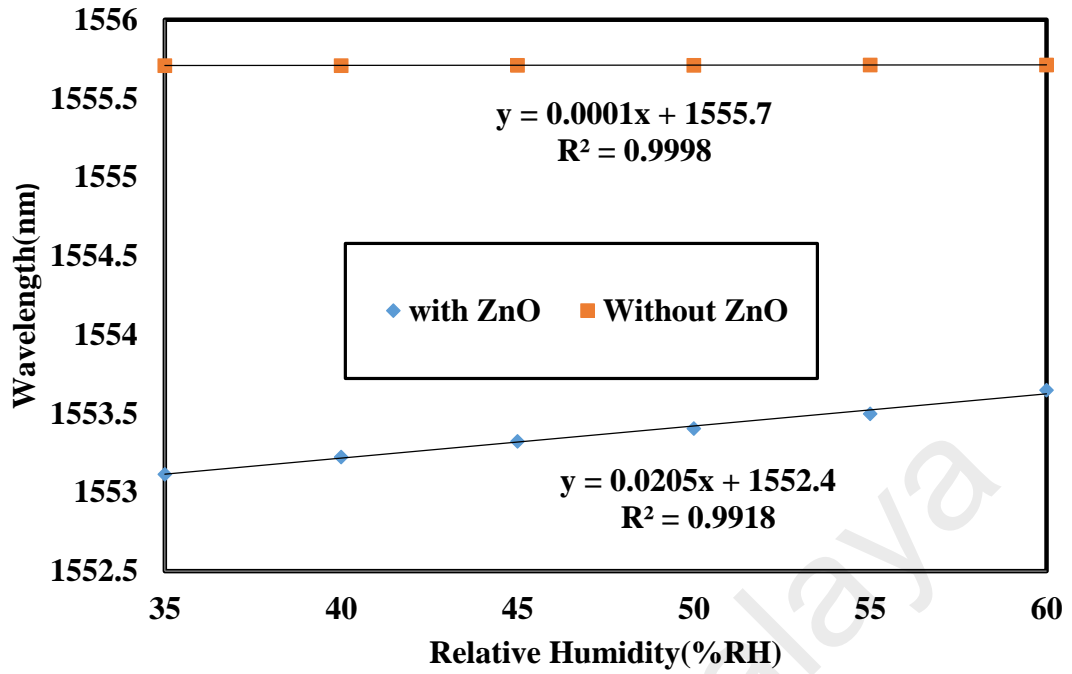


Figure 5.7: The linear relationship between humidity and resonant wavelength shift for with and without coated ZnO

Table 5. 1: The comparison of the proposed RH sensor

Parameter	Without ZnO	With ZnO
Sensitivity(nm/%RH)	0.0001	0.0205
Linear Range(%RH)	35-60	35-60
Linearity(%)	98.13	99.58
Limit of Detection(%)	11.55	0.02

Reversibility of the results is another important consideration in the operation of any sensor system. The results of spectrum shift as a function of RH are recorded in two different runs with increasing and decreasing RH as shown in Fig. 5.8. For the proposed IMZI sensor with ZnO coating, the wavelength shift response shows a good repeatability

with the maximum difference of output shift values between the two runs being ± 0.05 nm. Overall, the proposed sensor with ZnO coating is observed to be sufficiently stable with a standard deviation of 0.001nm. The time response of the sensor is estimated to be less than 5s and it is a function of the thickness of the ZnO coating. Compared to the conventional many methods for IMZI, the proposed sensor is easy to fabricate, cheap, and compact in size. Furthermore, we use the reflection approach for the measurement and thus this sensor probe is more practical in industry applications. However, it has also a minor drawback such as fragility of the fiber upon splicing process.

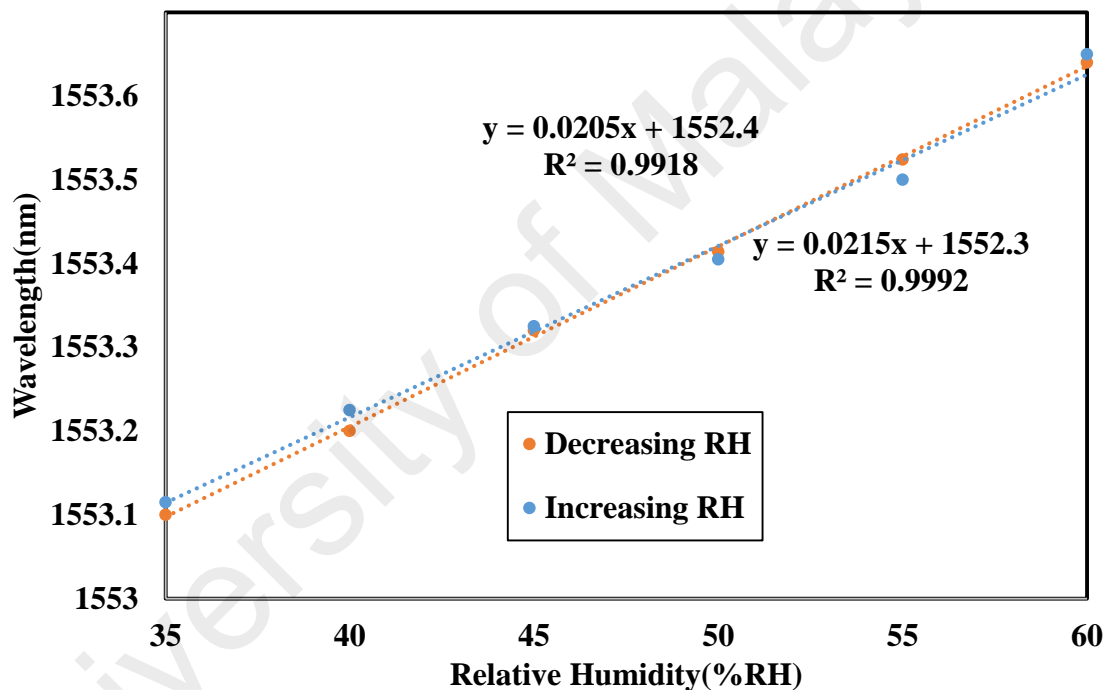


Figure 5.8: The reversibility of the results obtained for two different runs (relative humidity)

5.4 Inline Mach Zehnder Interferometer with ZnO Nanowires Coating for the measurement of uric acid concentrations

Most studies of optical-based chemical sensors have been based on the refractive index variation of the chemical under scrutiny (Khijwania & Gupta, 2000). However, the conductive nature of chemical solutions also plays a role in the output trend of the sensor (Lye, Boerkamp, Ernest, & Lamb, 2005). Chemicals can be classified as electrolytes and non-electrolytes depending on the dissociation of their ions in solution (Stokes & Robinson, 1966). An electrolyte is defined as a substance containing free ions that make the substance electrically conductive. A high proportion of solute dissociates to form free ions in strong electrolytes. Common types of electrolytes are group I and II salt solutions when in the form of ionic solution or molten. Electrolytes are important minerals in the human body which affect the amount of water in the body, blood acidify (pH), and muscle function (Zibaii et al., 2010).

Non-electrolytes are compounds composed of molecules that do not conduct electricity when dissolved in molten or aqueous solutions. They do not ionize in aqueous solution into positive and negative ions and hence fail to work as a conductor. They are normally covalent compounds and mainly organic in nature. Glucose, an example of a nonelectrolyte, is important to all cells from bacteria to humans as a primary source of energy, in photosynthesis, and as fuel for cellular respiration (Wolfbeis, 2008). Uric acid is another example of electrolyte, which consists of heterocyclic compound of carbon, nitrogen, oxygen, and hydrogen. Uric acid is a product of the metabolic break-down of purine nucleotides. Abnormal levels uric acid in human serum and urine are related to several medical complications such as gout, Lesh–Nyhan syndrome, and renal failure. Conventional methods that have been developed to detect the levels of these chemicals in human body include liquid chromatography (HPLC) (Ferin et al., 2013; N. A. Rahman et al., 2008), enzymatic assay (Thakur & Sawant, 2013) and other electrochemical (Khan

et al., 2013) processes. High level of serum uric acid is also considered as a risk factor for myocardial infarction and stroke (Chou, Lin, Lin, & Tsai, 2001; Iveković, Japac, Solar, & Živković, 2012). Therefore, the need for uric acid biosensors is tremendously increasing (Arora et al., 2014; Erden & Kılıç, 2013; Peng, 2013).

Conventional uric acid biosensors are based on amperometric principle which detects the oxygen consumption, chemiluminescence and fluoride ions (Iveković et al., 2012) This sensing method is complicated because it requires electrodes to be held at approximately 0.7V where other biological electro-active molecules react with the surface of the electrodes. Recently, Batumalay et al. (M Batumalay et al., 2014) has also demonstrated a fiber sensor for detecting uric acid concentration by using tapered Plastic Optical fiber (POF) coated with ZnO nanostructures using sol-gel immersion technique. The measurement is based on intensity modulation technique where the intensity of the transmitted light is measured for different uric acid concentration in distilled water. However, the intensity based sensor has many limitations that result in inaccuracy.

In the previous section, an inline IMZI with a dumbbell-shape structure was coated with ZnO nanowires to function as a probe in RH sensor. In this section, we demonstrate a new uric acid sensor based on the same sensor probe. The IMZI coated with ZnO nanowires is used to detect changes in uric acid concentrations in distilled water based on wavelength shift instead of intensity. The proposed MZI structure comprises two bulges connected by a tapered waist. The measurement is based on interferometric technique where the transmission spectrum of the reflected light is investigated with respect to different uric acid concentration in distilled water for with and without coated ZnO.

5.4.1 Experimental arrangement for uric acid sensing

Figure 5.9 shows the experimental setup used to detect different uric acid concentration using the IMZI as a probe. The input signal from an ASE laser source is launched into a sensor probe via a 3 dB coupler. The reflected signal from the sensor is then routed into an optical spectrum analyzer (OSA) through the same coupler. In this experiment, the dumbbell shaped MZI probe is immersed into uric solution of different concentrations ranging from 0 to 500 ppm. The solution was prepared by mixing uric acid and distilled water with different proportions of 0 ppm, 100 ppm, 200 ppm, 300 ppm, 400 ppm and 500 ppm, which corresponds to mixtures with refractive indices of 1.333, 1.3331, 1.3332, 1.3334, 1.3335 and 1.3336 respectively. Due to the compact structure of the sensor, a single drop of the liquid solution is enough to surround the whole dumbbell shape. The IMZI probe was cleansed with deionized water and compressed air after each measurement.

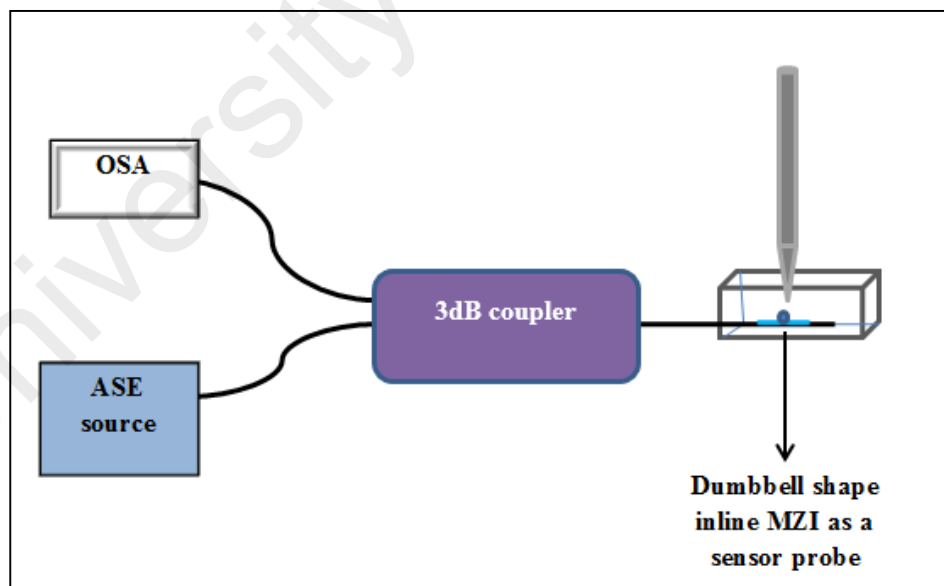


Figure 5.9 : The experimental setup used to detect different uric acid concentration using the inline MZI dumbbell structures

5.4.2 Performance of the proposed uric acid sensor

Figures 5.10 and 5.11 show the reflected spectrum at various uric acid concentrations in DI water, which were obtained from the sensor probe configured without and with the ZnO nanowires coating, respectively. It is observed that both sensor probes obtain a comb like reflected spectrum as a broadband ASE is launched into the device. This is attributed to the optical path difference (OPD) between cladding and core modes, which produces an interference pattern in both the dumbbell shaped IMZI structures. It is found that the interference spectra for both outputs are red-shifted when the concentration of uric acid rises from 0 to 500 ppm. The wavelength change of one of the transmission peaks with the increase in uric acid concentration is depicted in Figure 5.12 for both sensors. As observed, the peak-wavelength shift linearly increases as the concentration of the uric acid of the solution increases. The sensitivity for MZI coated with ZnO nanowires is obtained at 0.001nm/% and the slope shows a good linearity of more than 99.33 % for a 5.74 % limit of detection (LOD). On the other hand, the sensitivity of MZI-based sensor without coated ZnO is 0.0005 %/nm with a slope linearity of more than 99.81 and limit of detection is 8.55 %. LOD is calculated by dividing the standard deviation with the sensitivity, which indicates that the system is more efficient when the value of LOD is lower. Based on these results, it is found that the sensitivity of MZI-coated with ZnO is higher than without coated. This is due to the uric acid is an electrolyte, a substance containing free ions that make the substance electrically conductive. The MZI coated with ZnO nanowires interact with uric acid due to strong

electrostatic interaction and improve the sensing response with the increasing uric acid concentration.

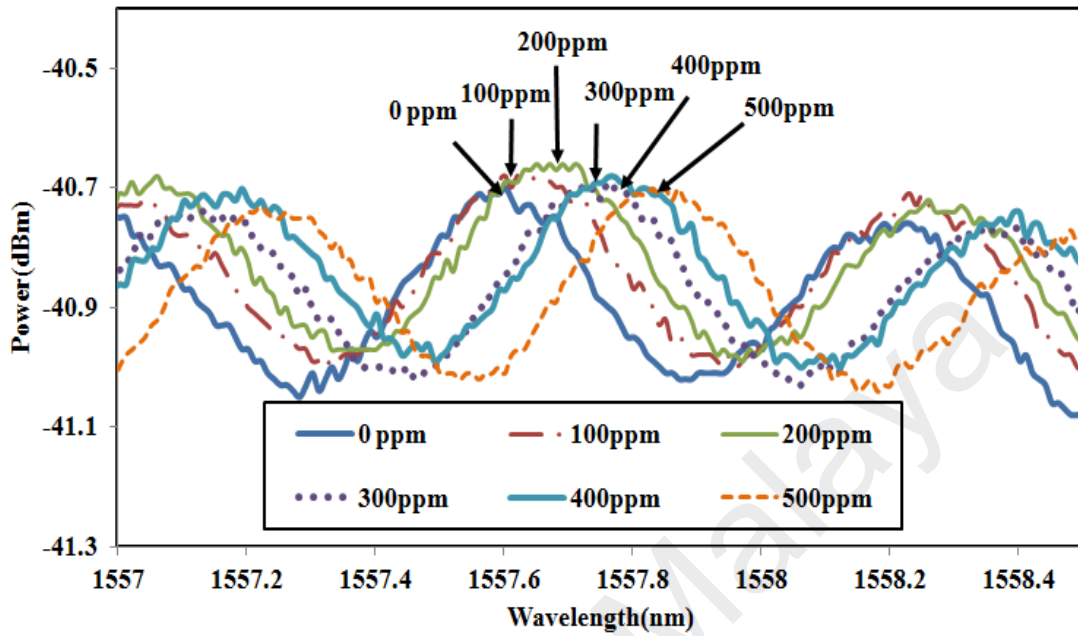


Figure 5.10: An interference pattern for without ZnO composite

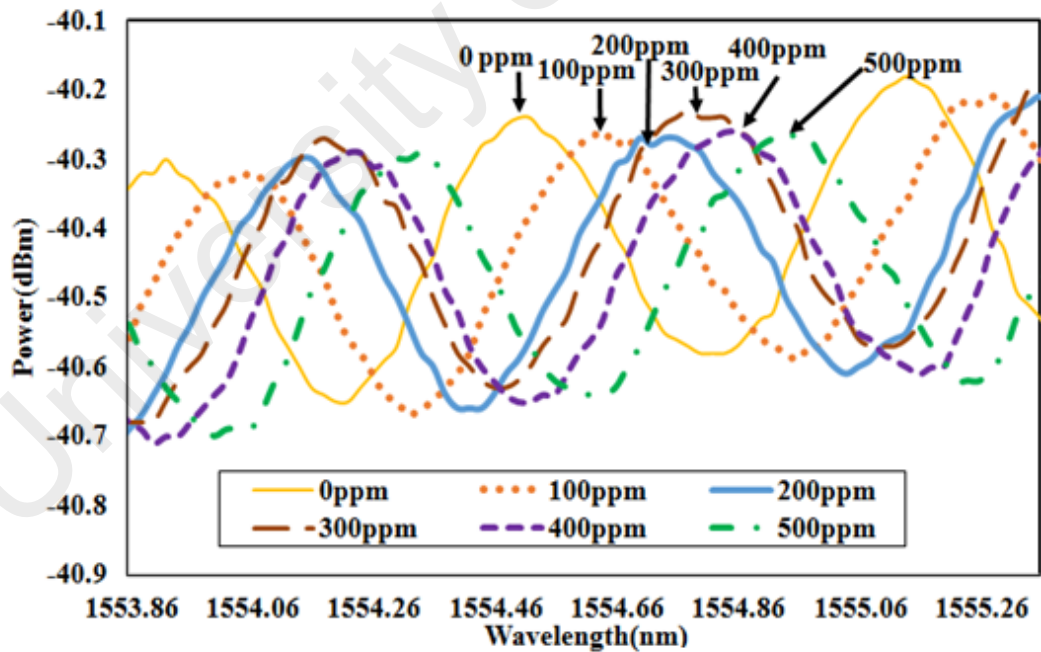


Figure 5.11: An interference pattern for with ZnO composite

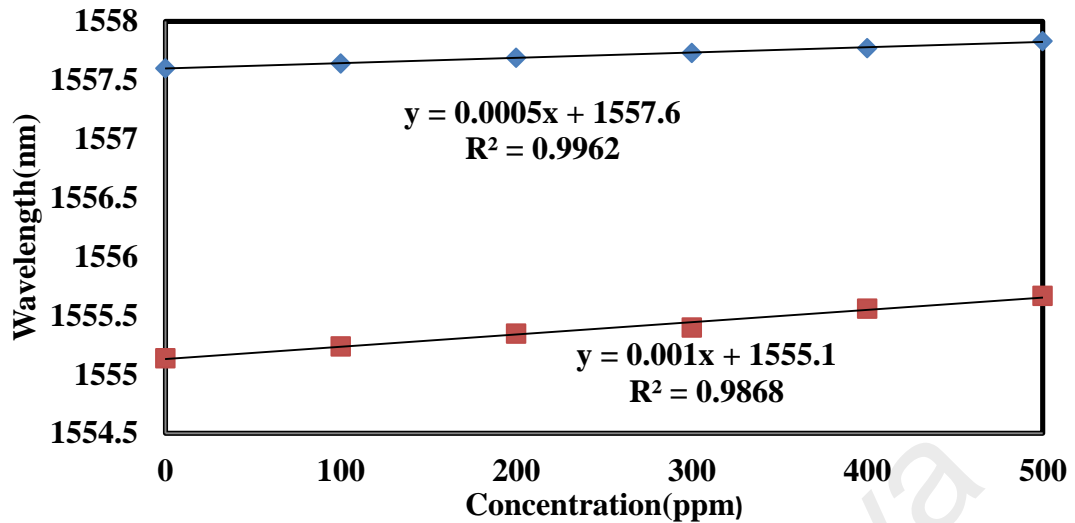


Figure 5.12: The wavelength change of one of the transmission peaks with the increase in uric acid concentration

Reversibility is an important factor to consider in the test of any sensing system. The results of the output measurement as a function of concentration are recorded for two different test runs and the outputs are compared for the inline MZI-sensor with ZnO nanowires. In Figure 5.13, the maximum difference between the two runs is about ± 0.05 nm, which is acceptable for a full-scale output of 1555 nm. These results indicate that the proposed sensor is reliable and useful for the detection of bio-molecular concentrations such as uric acid, glucose and sodium chloride. The performance of the uric acid sensing using the proposed inline MZI probe is summarized in Table 5.3.

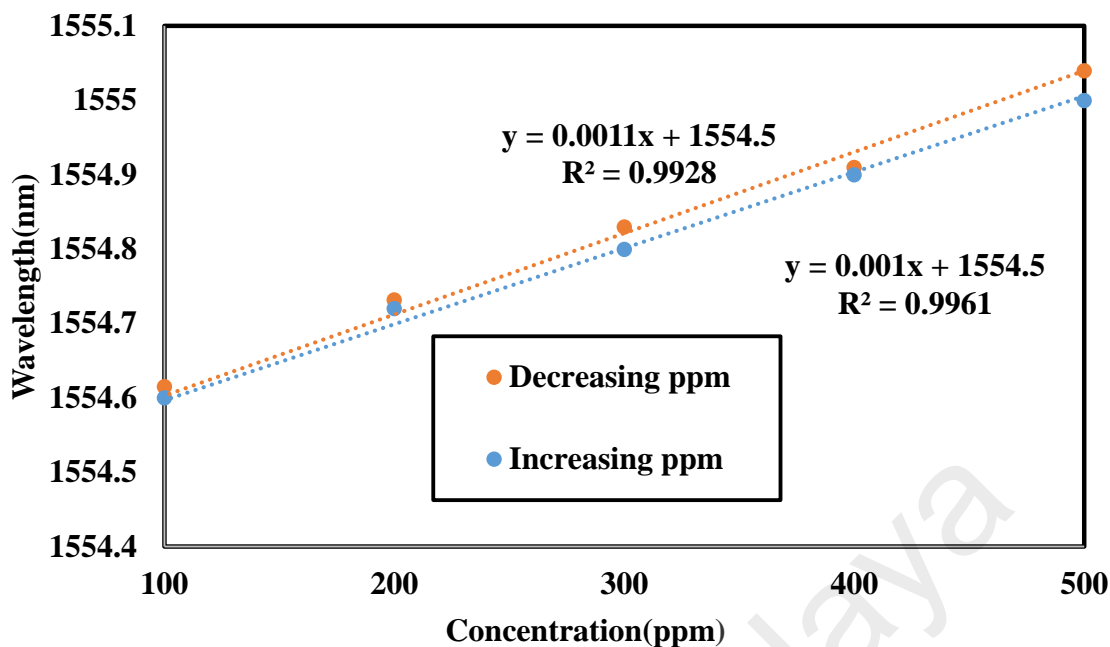


Figure 5.13: The reversibility of the results obtained for two different runs

Table 5.2: The performance of the proposed uric acid detection sensor

Parameter	Without ZnO	With ZnO
Sensitivity(nm/ppm)	0.0005	0.001
Linear Range(%)	0-500	0-500
Linearity(%)	99.81	99.8
Limit of Detection(%)	8.05	5.74

5.5 Summary

A simple IMZI with a dumbbell-shaped structure is proposed as a sensor probe for both RH and uric acid concentration measurements. Both measurements are based on interferometric technique where the transmission spectrum of the reflected light is

investigated with respect to the change in the surrounding refractive index. The performance of both sensors is investigated for the probe with and without ZnO nanowires coating. For the RH sensor, it can be seen that the output spectrum is red-shifted when the level of surrounding RH increases. For instance, the resonant peak wavelength increases from 1553.715 to 1554.205 nm as the RH increases from 35 to 60%RH. It is found that the sensitivity of IMZI based sensor significantly improves with the ZnO coating. The sensitivity of the sensor is approximately 0.0205 nm/%RH with a slope linearity of more than 99.58 and limit of detection of 0.02%. For uric acid sensor, it is observed that the interference spectrum is also red-shifted when the concentration of uric acid rises from 0 to 500 ppm. The peak-wavelength shift linearly increases as the concentration of the uric acid of the solution increases. The sensitivity for MZI coated with ZnO is obtained at 0.001nm/% and the slope shows a good linearity of more than 99.33% for a 5.74% limit of detection (LOD). On the other hand, the sensitivity of MZI-based sensor without coated ZnO is 0.0005%/nm with a slope linearity of more than 99.81 and LOD is 8.55%. LOD is calculated by dividing the standard deviation with the sensitivity, which indicates that the system is more efficient when the value of LOD is lower. It can be concluded that the sensitivity of MZI-coated with ZnO is higher than the one without. This is due to the uric acid being an electrolyte, a substance containing free ions that makes the substance electrically conductive. The MZI coated with ZnO nanostructures interact with uric acid due to strong electrostatic interaction and response with increasing concentration. These results show that the proposed sensor is applicable and useful for the detection of biomolecular concentration such as uric acid, glucose and fructose. The proposed probe for both sensors is easy to fabricate, cheap, and compact in size.

CHAPTER 6: CONCLUSION AND FUTURE WORK

6.1 Conclusion

Compact in-line fiber optic core cladding mode interferometers (CCMIs) are attractive for chemical, physical, and biological sensing applications. The CCMIs operate by exploiting the coupling and re-coupling between the modes of the fiber core and cladding. The core mode is guided by the core-cladding interface of the fiber and the cladding mode is guided by the cladding-ambient interface. Due to the phase difference between the core and cladding modes, CCMIs are able to measure the parameters of the surrounding environment. In a Mach Zehnder Interferometer (MZI), the core and cladding modes are split and then recombined. Due to the optical phase difference (OPD) between cladding and core modes, an interference pattern is observed in the output. The main objective of this thesis is to develop an inline Mach Zehnder Interferometer (IMZI) with a dumbbell shape which is easy to fabricate, compact and simple. Since the in-line interferometric sensor is made of normal single mode fibers (SMFs), it should be cheap to produce. The IMZIs are used as a sensor probe to measure relative humidity and the concentration of various biochemicals in distilled water.

Research works that have been carried out are reported in three main chapters of the thesis. In Chapter 3, two sensing methods for RH measurement using tapered fiber are investigated and they are intensity modulation and interferometric techniques. On top of that, a mixture of HEC and PVDF is introduced as a coating material for the tapered fiber. HEC and PVD was prepared by dissolving 1g of PVDF powder ($M_w = 275,000$) in 120 ml dimethyl sulfoxide (DMSO) and 100ml distilled water at 90°C in water bath. Then the solution of PVDF is cooled down to room temperature and 4 g of HEC is added and continuously stirred at room temperature for about 10 hours to generate a three-dimensional structure of the mesh gel (hydrogel). The resulting polymer gel has a good absorption of water in the air. The hydrogel coating acts as an inner cladding whose

refractive index decreases with the rise in humidity and thus allows more lights to be transmitted in humid state. A difference of up to 0.89 dB in the transmitted optical power is observed when RH changes from 50 to 80%. The proposed sensor has a sensitivity of about 0.030 dB/%RH with a slope linearity of more than 99.5 %.

Then, another humidity sensor based on tapered non-adiabatic SMF coated with a mixed polymer composite HEC/PVDF is tested using interferometric technique. The tapered fiber, coated with a humidity-sensitive cladding creates intermodal interference which enables the detection of humidity change. The sensitivity of the sensor is 0.0041nm/% within the RH range from 20 to 45 % at the optimum tapered fiber diameter of 50 μm . The performance of the sensor based on the reflected light from the sensor probe is also studied. It is observed that the resonant dip wavelength increases from 1554.58 to 1554.85 nm as the RH increases from 10 to 80%. Finally, an innovative RH sensor in the form of an FBG coated with HEC/PVDF composite is introduced. The reflected wavelength of the FBG is red-shifted as the relative humidity increases from 10% to 80%. This is attributed to the changes in RH that alters the physical and optical properties of the coating thereby influencing the evanescent waves that travels within. The sensitivity of the sensor is 0.0011 nm/% within an RH range from 20 % to 45 %. The performance of the interferometric based RH sensor is summarized in Table 6.1.

Table 6.1 : The performance of humidity sensor using interferometric technique

Parameter	SMF (Transmission)	SMF (Reflected)	FBG
Sensitivity (nm/%)	0.004	0.0074	0.0011
Linear Range (%)	20-45	20-45	20-45
Linearity (%)	99.1	98.85	98.05

The results show that all the tested sensors can potentially be applied for RH measurement as they are easy to fabricate and configured. However, the accuracy of both tapered fiber and etched FBG structures are susceptible to air turbulence and dust or moisture contamination. Dust or moisture that accumulates on the tapered or etched fiber may interfere with the light transmission. Furthermore, although easy to construct, repeatability of the sensor fabrication is not guaranteed since the chemical etching technique is always influenced by external factors such as vibration, temperature change and impurity in etching solution. Finally, in order to manufacture an FBG, a special equipment is needed which may increase the fabrication cost.

In Chapter 4, a new sensor is introduced to improve the sensitivity of the previous sensor. A new dumbbell-shaped inline MZI is successfully developed using an arcing process of a fusion splicer. The sensor is tested for measuring RH of the environment and bio-chemical concentration in distilled water. The sensor probe consists of two bulges separated by a tapered waist that generates a good reflected interference spectrum. Since the two bulges act as a beam splitter and combiner, changes in their diameters influence the output interference spectrum. It is observed that bigger bulge diameter generates higher the ER, and longer separation length produces lower FSR. First, a new evanescent wave based sensor is proposed using a dumbbell structure coated with HEC/PVDF composite for RH measurement. It is observed that the resonant dip wavelength for MZI dumbbell shape increases from 1555.76 to 1556.34 nm as the RH increases from 10 to

80%. The sensor exhibits a linear shift especially within the range from 20 to 45% with a sensitivity of 0.0123nm/%. Its linearity is 99.88% and its limit of detection is 0.44%. The inline MZI is also used for detecting bio-chemical concentration in distilled water. Its interference spectrum red-shifts with the increase in bio-chemical concentration due to the rise in the refractive index of the surrounding, which reduces the phase difference between the core and cladding modes. For instance, as the glucose concentration increases from 0 to 12%, the dip wavelength red-shifts from 1554.419 to 1554.939 nm in a quadratic manner with a coefficient of determination of 0.9818. It is also found that the sensor has a sensitivity of 0.0402nm/% with a linearity of 96.72% and limit of detection of 4.5%. For NaCl solution, the dip-wavelength shift is linearly proportional to the increase in the concentration of the sodium chloride solution or salinity. The sensitivity is obtained at 0.0329 nm/%. The slope has a good linearity of more than 99.68% for a 4.32% limit of detection. Lastly, for uric acid, the sensitivity is obtained at 0.0006 nm/% and the slope shows a good linearity of more than 99.48% for a 7.52% limit of detection.

Additionally, to investigate the effect of temperature on the sensor, an experiment is performed where glucose and NaCl concentrations are fixed at 6%, while the concentration of uric acid is fixed at 200 ppm. Then the temperature is increased from 30⁰ C to 50⁰ C in 5⁰ C step. It is observed that the interference spectra of the output for all three chemical sensors are red-shifted as temperature increases. Also, for all cases the wavelength shift is linear with temperature increase. Since wavelength shift is linearly dependent on both concentration and temperature of bio-chemical solutions, a multiple linear regression (MLR) analysis is used to combine the variables in a single equation. The MLR analysis is performed using SPSS Statistics software. From the analysis, it is found that the P-value of all biochemical sensors are less than the specified significance level of 0.05. Thus, it can be concluded that both concentration and temperature influence the spectrum shift of the output.

Lastly, in chapter 5, Zinc Oxide (ZnO) nanowires structure is developed as a coating sensitive material for the sensor. ZnO can be synthesized by aqueous solution of zinc nitrate hexahydrate ($\text{Zn}(\text{NO}_3)_2 \cdot 6\text{H}_2\text{O}$ (0.01 M) and hexamethylenetetramine (HMTA; $\text{C}_6\text{H}_{12}\text{N}_4$) (0.01 M) in deionized (DI) water. The mixture is stirred at 60°C for 2 hours to obtain a clear homogeneous ZnO aqueous solution and then, the solution is kept for 24 hours prior to fiber coating process. Subsequently, the IMZI structure is dipped into the ZnO solution and let dry at 60°C to evaporate the solvent and to remove organic residuals. This coating and drying method is repeated five times to increase the thickness of the coating layer. The IMZI with a dumbbell-shaped structure is used as a sensor probe for both RH and uric acid concentration measurements. Both measurements are based on interferometric technique where the transmission spectrum of the reflected light is investigated with respect to the change in surrounding refractive index. For comparison, the performance of the coated sensor is compared against the one without ZnO nanowires coating. For the RH sensor, it can be seen that the output spectrum is red-shifted when the RH level increases. For instance, the resonant peak wavelength increases from 1553.715 to 1554.205 nm as the RH increases from 35 to 60%RH. It is found that the sensitivity of IMZI sensor significantly improves with the ZnO coating. The sensitivity of the sensor is approximately 0.0205 nm/%RH with a slope linearity of more than 99.58 and limit of detection of 0.02%.

For uric acid sensing, the interference spectrum is also red-shifted when the concentration of uric acid rises from 0 to 500 ppm. The peak-wavelength shift, linearly increases as the concentration of the uric acid of the solution increases. The sensitivity of MZI coated with ZnO is 0.001nm/% and the slope linearity is more than 99.33% for a 5.74% limit of detection (LOD). On the other hand, the sensitivity of MZI-based sensor without ZnO coating is 0.0005%/nm with a slope linearity of more than 99.81 and LOD of 8.55%. LOD is calculated by dividing the standard deviation with the sensitivity. A system is more efficient when its LOD is lower. In summary, the sensitivity of MZI-

coated with ZnO is higher than the one without. This is due to the uric acid being an electrolyte, a substance containing free ions that makes it electrically conductive. The free ions attach to the structures on the surface of the sensor due to strong electrostatic interaction. This enables the structure to trap more water molecules as the concentration of the uric acid increases, thereby changing the refractive index of the coating. The results show that the proposed sensor is able to measure the RH of its surrounding and the concentration of uric acid, glucose and fructose. Overall, the proposed dumbbell shape MZI sensor has a high potential for RH sensing and bio-chemical concentration measurement as it is easy to fabricate, low in cost, and compact in size.

6.2 Future Work

Future work should focus on improving the manufacturing method of the IMZI in order to smoothen the uneven surface of the structure. CO₂ laser and fiber heater could be used in this new development. A new coating sensitive material such as Aluminum doped ZnO should also be explored to enhance the sensitivity of the sensor. Of course, the most important thing is to find new applications for the IMZI particularly in laser generation.

REFERENCES

- Ali, S. M. U., Alvi, N., Ibupoto, Z., Nur, O., Willander, M., & Danielsson, B. (2011). Selective potentiometric determination of uric acid with uricase immobilized on ZnO nanowires. *Sensors and Actuators B: Chemical*, 152(2), 241-247.
- Ali, S. M. U., Ibupoto, Z. H., Kashif, M., Hashim, U., & Willander, M. (2012). A potentiometric indirect uric acid sensor based on ZnO nanoflakes and immobilized uricase. *Sensors*, 12(3), 2787-2797.
- Arora, K., Tomar, M., & Gupta, V. (2014). Reagentless uric acid biosensor based on Ni microdiscs-loaded NiO thin film matrix. *Analyst*, 139(18), 4606-4612.
- Arregui, F. J. (2009). *Sensors based on nanostructured materials*: Springer.
- Batumalay, M., Ahmad, F., Lokman, A., Jasim, A., Wadi Harun, S., & Ahmad, H. (2014). Tapered plastic optical fiber coated with single wall carbon nanotubes polyethylene oxide composite for measurement of uric acid concentration. *Sensor Review*, 34(1), 75-79.
- Batumalay, M., Harith, Z., Rafaie, H., Ahmad, F., Khasanah, M., Harun, S., . . . Ahmad, H. (2014). Tapered plastic optical fiber coated with ZnO nanostructures for the measurement of uric acid concentrations and changes in relative humidity. *Sensors and Actuators A: Physical*, 210, 190-196.
- Chou, P., Lin, K.-C., Lin, H.-Y., & Tsai, S.-T. (2001). Gender differences in the relationships of serum uric acid with fasting serum insulin and plasma glucose in patients without diabetes. *The Journal of rheumatology*, 28(3), 571-576.
- Erden, P. E., & Kılıç, E. (2013). A review of enzymatic uric acid biosensors based on amperometric detection. *Talanta*, 107, 312-323.
- Ferin, R., Pavão, M. L., & Baptista, J. (2013). Rapid, sensitive and simultaneous determination of ascorbic and uric acids in human plasma by ion-exclusion HPLC-UV. *Clinical biochemistry*, 46(7), 665-669.
- Iijima, S. (1991). Helical microtubules of graphitic carbon. *nature*, 354(6348), 56-58.
- Iveković, D., Japec, M., Solar, M., & Živković, N. (2012). Amperometric uric acid biosensor with improved analytical performances based on alkaline-stable H₂O₂ transducer. *Int. J. Electrochem. Sci*, 7, 3252-3264.
- Khan, M. M. I., Haque, A.-M. J., & Kim, K. (2013). Electrochemical determination of uric acid in the presence of ascorbic acid on electrochemically reduced graphene oxide modified electrode. *Journal of Electroanalytical Chemistry*, 700, 54-59.
- Khijwania, S., & Gupta, B. (2000). Maximum achievable sensitivity of the fiber optic evanescent field absorption sensor based on the U-shaped probe. *Optics Communications*, 175(1), 135-137.
- Kissinger, H. E. (1957). Reaction kinetics in differential thermal analysis. *Analytical chemistry*, 29(11), 1702-1706.
- Liu, Y., Jian-er, Z., Larbot, A., & Persin, M. (2007). Preparation and characterization of nano-zinc oxide. *Journal of Materials Processing Technology*, 189(1), 379-383.

- Lye, P., Boerkamp, M., Ernest, A., & Lamb, D. (2005). *Investigating the sensitivity of PMMA optical fibres for use as an evanescent field absorption sensor in aqueous solutions*. Paper presented at the Journal of Physics: Conference Series.
- Peng, Y. (2013). A Novel Sensor for Uric Acid Based on an Electropolymerization Technique. *AMERICAN LABORATORY*, 45(8), 26-28.
- Rahman, N. A., Hasan, M., Hussain, M., & Jahim, J. (2008). Determination of glucose and fructose from glucose isomerization process by high performance liquid chromatography with UV detection. *Modern Applied Science*, 2(4), p151.
- Sekar, A., Kim, S., Umar, A., & Hahn, Y. (2005). Catalyst-free synthesis of ZnO nanowires on Si by oxidation of Zn powders. *Journal of Crystal Growth*, 277(1), 471-478.
- Stokes, R., & Robinson, R. (1966). Interactions in aqueous nonelectrolyte solutions. I. Solute-solvent equilibria. *The Journal of Physical Chemistry*, 70(7), 2126-2131.
- Subramanyam, T., Srinivasulu Naidu, B., & Uthanna, S. (2000). Physical properties of zinc oxide films prepared by dc reactive magnetron sputtering at different sputtering pressures. *Crystal Research and Technology*, 35(10), 1193-1202.
- Sun, A., Li, Z., Wei, T., Li, Y., & Cui, P. (2009). Highly sensitive humidity sensor at low humidity based on the quaternized polypyrrole composite film. *Sensors and Actuators B: Chemical*, 142(1), 197-203.
- Thakur, B., & Sawant, S. N. (2013). Polyaniline/Prussian-Blue-Based Amperometric Biosensor for Detection of Uric Acid. *ChemPlusChem*, 78(2), 166-174.
- Viswanathan, R., & Gupta, R. B. (2003). Formation of zinc oxide nanoparticles in supercritical water. *The Journal of supercritical fluids*, 27(2), 187-193.
- Wolfbeis, O. S. (2008). Fiber-optic chemical sensors and biosensors. *Analytical chemistry*, 80(12), 4269-4283.
- Yao, C., Wu, H., Ge, M., Yang, L., Zeng, Y., Wang, Y., & Jiang, J. (2007). Triangle-shape ZnO prepared by thermal decomposition. *Materials Letters*, 61(16), 3416-3420.
- Yawong, O., Choopun, S., Mangkorntong, P., Mangkorntong, N., & Chiang, M. (2005). Zinc Oxide Nanostructure by Oxidization of Zinc Thin Films. *University Journal Special Issue on Nanotechnology 4 (1)*.
- Zibaii, M. I., Kazemi, A., Latifi, H., Azar, M. K., Hosseini, S. M., & Ghezelaigh, M. H. (2010). Measuring bacterial growth by refractive index tapered fiber optic biosensor. *Journal of Photochemistry and Photobiology B: Biology*, 101(3), 313-320.
- Allsop, T., Reeves, R., Webb, D. J., Bennion, I., & Neal, R. (2002). A high sensitivity refractometer based upon a long period grating Mach-Zehnder interferometer. *Review of scientific instruments*, 73(4), 1702-1705.

- Bariain, C., Matías, I. R., Arregui, F. J., & Lopez-Amo, M. (2000). Optical fiber humidity sensor based on a tapered fiber coated with agarose gel. *Sensors and Actuators B: Chemical*, 69(1), 127-131.
- Batimalay, M., Lokman, A., Ahmad, F., Arof, H., Ahmad, H., & Harun, S. W. (2013). Tapered plastic optical fiber coated with HEC/PVDF for measurement of relative humidity. *Sensors Journal, IEEE*, 13(12), 4702-4705.
- Brambilla, G., Jung, Y., & Renna, F. (2010). Optical fiber microwires and nanowires manufactured by modified flame brushing technique: properties and applications. *Frontiers of Optoelectronics in China*, 3(1), 61-66.
- Corres, J. M., Matias, I. R., & Arregui, F. J. (2008). Optical Fibre Humidity Sensors Using Nano-films *Sensors* (pp. 153-177): Springer.
- Ferin, R., Pavão, M. L., & Baptista, J. (2013). Rapid, sensitive and simultaneous determination of ascorbic and uric acids in human plasma by ion-exclusion HPLC-UV. *Clinical biochemistry*, 46(7), 665-669.
- Fu, H., Tam, H., Shao, L.-Y., Dong, X., Wai, P., Lu, C., & Khijwania, S. K. (2008). Pressure sensor realized with polarization-maintaining photonic crystal fiber-based Sagnac interferometer. *Applied optics*, 47(15), 2835-2839.
- Gehrich, J. L., Lübbers, D. W., Opitz, N., Hansmann, D. R., Miller, W. W., Tusa, J. K., & Yafuso, M. (1986). Optical fluorescence and its application to an intravascular blood gas monitoring system. *Biomedical Engineering, IEEE Transactions on*(2), 117-132.
- Hernández, G. (1988). *Fabry-Perot Interferometers* (Vol. 3): Cambridge University Press.
- Huang, Z., Zhu, Y., Chen, X., & Wang, A. (2005). Novel intrinsic Fabry-Perot fiber sensor using single mode-multimode-single mode structure. *IEEE Photon. Technol. Lett*, 17, 2403-2405.
- Jiang, M., & Gerhard, E. (2001). A simple strain sensor using a thin film as a low-finesse fiber-optic Fabry-Perot interferometer. *Sensors and Actuators A: Physical*, 88(1), 41-46.
- Khan, M. M. I., Haque, A.-M. J., & Kim, K. (2013). Electrochemical determination of uric acid in the presence of ascorbic acid on electrochemically reduced graphene oxide modified electrode. *Journal of Electroanalytical Chemistry*, 700, 54-59.
- Li, Y., Harris, E., Chen, L., & Bao, X. (2010). Application of spectrum differential integration method in an in-line fiber Mach-Zehnder refractive index sensor. *Optics Express*, 18(8), 8135-8143.
- Lu, P., Men, L., Sooley, K., & Chen, Q. (2009). Tapered fiber Mach-Zehnder interferometer for simultaneous measurement of refractive index and temperature. *Applied Physics Letters*, 94(13), 131110.

- Machavaram, V., Badcock, R., & Fernando, G. (2007). Fabrication of intrinsic fibre Fabry–Perot sensors in silica fibres using hydrofluoric acid etching. *Sensors and Actuators A: Physical*, 138(1), 248-260.
- Mignani, A. G., & Baldini, F. (1996). Biomedical sensors using optical fibres. *Reports on Progress in Physics*, 59(1), 1.
- Moon, D. S., Kim, B. H., Lin, A., Sun, G., Han, Y.-G., Han, W.-T., & Chung, Y. (2007). The temperature sensitivity of Sagnac loop interferometer based on polarization maintaining side-hole fiber. *Optics Express*, 15(13), 7962-7967.
- Rahman, N. A., Hasan, M., Hussain, M., & Jahim, J. (2008). Determination of glucose and fructose from glucose isomerization process by high performance liquid chromatography with UV detection. *Modern Applied Science*, 2(4), p151.
- Sumetsky, M., Dulashko, Y., Fini, J., Hale, A., & DiGiovanni, D. (2006). The microfiber loop resonator: Theory, experiment, and application. *Lightwave Technology, Journal of*, 24(1), 242-250.
- Swart, P. L. (2004). Long-period grating Michelson refractometric sensor. *Measurement Science and Technology*, 15(8), 1576.
- Thakur, B., & Sawant, S. N. (2013). Polyaniline/Prussian-Blue-Based Amperometric Biosensor for Detection of Uric Acid. *ChemPlusChem*, 78(2), 166-174.
- Tong, L. (2010). Brief introduction to optical microfibers and nanofibers. *Frontiers of Optoelectronics in China*, 3(1), 54-60.
- Wang, Y., Yang, M., Wang, D., Liu, S., & Lu, P. (2010). Fiber in-line Mach-Zehnder interferometer fabricated by femtosecond laser micromachining for refractive index measurement with high sensitivity. *JOSA B*, 27(3), 370-374.
- Wang, Z., Shen, F., Song, L., Wang, X., & Wang, A. (2007). Multiplexed fiber Fabry–Perot interferometer sensors based on ultrashort Bragg gratings. *Photonics Technology Letters, IEEE*, 19(8), 622-624.
- Wei, T., Han, Y., Tsai, H.-L., & Xiao, H. (2008). Miniaturized fiber inline Fabry-Perot interferometer fabricated with a femtosecond laser. *Optics letters*, 33(6), 536-538.
- Zheng, Y., Dong, X., Zhao, C., Li, Y., Shao, L., & Jin, S. (2013). Relative humidity sensor based on microfiber loop resonator. *Advances in Materials Science and Engineering*, 2013.
- Abrate, S. (2002). Structural Monitoring with Fiber Optic Technology. *Applied Mechanics Reviews*, 55, 10.
- Alvarez-Herrero, A., Guerrero, H., & Levy, D. (2004). High-sensitivity sensor of low relative humidity based on overlay on side-polished fibers. *Sensors Journal, IEEE*, 4(1), 52-56.
- Ansari, F. (2005). *Sensing issues in civil structural health monitoring* (Vol. 10): Springer.

- Balta, J., Bosia, F., Michaud, V., Dunkel, G., Botsis, J., & Månson, J. (2005). Smart composites with embedded shape memory alloy actuators and fibre Bragg grating sensors: activation and control. *Smart materials and structures*, *14*(4), 457.
- Bariain, C., Matías, I. R., Arregui, F. J., & Lopez-Amo, M. (2000). Optical fiber humidity sensor based on a tapered fiber coated with agarose gel. *Sensors and Actuators B: Chemical*, *69*(1), 127-131.
- Batumalay, M., & Harun, S. W. (2013). *Relative humidity measurement using tapered plastic fiber coated with HEC/PVDF*. Paper presented at the Technology, Informatics, Management, Engineering, and Environment (TIME-E), 2013
- Batumalay, M., Lokman, A., Ahmad, F., Arof, H., Ahmad, H., & Harun, S. W. (2013). Tapered plastic optical fiber coated with HEC/PVDF for measurement of relative humidity. *Sensors Journal, IEEE*, *13*(12), 4702-4705.
- Clark, A. H., & Ross-Murphy, S. B. (1987). Structural and mechanical properties of biopolymer gels *Biopolymers* (pp. 57-192): Springer.
- Corres, J. M., Arregui, F. J., & Matías, I. R. (2007). Sensitivity optimization of tapered optical fiber humidity sensors by means of tuning the thickness of nanostructured sensitive coatings. *Sensors and Actuators B: Chemical*, *122*(2), 442-449.
- Dawood, T., Sheno, R., & Sahin, M. (2007). A procedure to embed fibre Bragg grating strain sensors into GFRP sandwich structures. *Composites Part A: Applied Science and Manufacturing*, *38*(1), 217-226.
- Del Villar, I., Zamarreño, C. R., Hernaez, M., Arregui, F. J., & Matias, I. R. (2010). Resonances in coated long period fiber gratings and cladding removed multimode optical fibers: a comparative study. *Optics Express*, *18*(19), 20183-20189.
- Doliba, N. M., Wehrli, S. L., Babsky, A. M., Doliba, N. M., & Osbakken, M. D. (1998). Encapsulation and perfusion of mitochondria in agarose beads for functional studies with ³¹P-NMR spectroscopy. *Magnetic resonance in medicine*, *39*(5), 679-684.
- Estella, J., de Vicente, P., Echeverría, J. C., & Garrido, J. J. (2010). A fibre-optic humidity sensor based on a porous silica xerogel film as the sensing element. *Sensors and Actuators B: Chemical*, *149*(1), 122-128.
- Hassan, M. R. A., Bakar, M. H. A., Dambul, K., & Adikan, F. R. M. (2012). Optical-based sensors for monitoring corrosion of reinforcement rebar via an etched cladding Bragg grating. *Sensors*, *12*(11), 15820-15826.
- Iglesias, O., Garcia, A., Roques, M., & Bueno, J. (1993). Drying of water gels: determination of the characteristic curve of agar-agar. *Drying technology*, *11*(3), 571-587.

- Kurihara, H., Torigoe, S., Omura, M., Saito, K., Kurihara, M., & Matsubara, S. (1998). DNA fragmentation induced by a cytoplasmic extract from irradiated cells. *Radiation research*, 150(3), 269-274.
- Miao, Y., Liu, B., Zhang, H., Li, Y., Zhou, H., Sun, H., . . . Zhao, Q. (2009). Relative humidity sensor based on tilted fiber Bragg grating with polyvinyl alcohol coating. *Photonics Technology Letters, IEEE*, 21(7), 441-443.
- Morisawa, M., Amemiya, Y., Kohzu, H., Liang, C. X., & Muto, S. (2001). Plastic optical fibre sensor for detecting vapour phase alcohol. *Measurement Science and Technology*, 12(7), 877.
- Muhammad, M., Jasim, A., Ahmad, H., Arof, H., & Harun, S. (2013). Non-adiabatic silica microfiber for strain and temperature sensors. *Sensors and Actuators A: Physical*, 192, 130-132.
- Müller, M. S., Buck, T. C., & Koch, A. W. (2009). *Fiber Bragg grating-based acceleration sensor*. Paper presented at the Optomechatronic Technologies, 2009. ISOT 2009. International Symposium on.
- Muto, S., Suzuki, O., Amano, T., & Morisawa, M. (2003). A plastic optical fibre sensor for real-time humidity monitoring. *Measurement Science and Technology*, 14(6), 746.
- Qi, Z.-m., Honma, I., & Zhou, H. (2006). Humidity sensor based on localized surface plasmon resonance of multilayer thin films of gold nanoparticles linked with myoglobin. *Optics letters*, 31(12), 1854-1856.
- Rahman, H., Harun, S., Yasin, M., Phang, S., Damanhuri, S., Arof, H., & Ahmad, H. (2011). Tapered plastic multimode fiber sensor for salinity detection. *Sensors and Actuators A: Physical*, 171(2), 219-222.
- Srimannarayana, K., Shankar, M., Prasad, R. L. S., Mohan, T. K., Ramakrishna, S., Srikanth, G., & Rao, S. R. P. (2008). Fiber Bragg grating and long period grating sensor for simultaneous measurement and discrimination of strain and temperature effects. *Optica applicata*, 38(3), 601-608.
- Sun, A., Li, Z., Wei, T., Li, Y., & Cui, P. (2009). Highly sensitive humidity sensor at low humidity based on the quaternized polypyrrole composite film. *Sensors and Actuators B: Chemical*, 142(1), 197-203.
- Wang, P., Liu, J., Li, C., Chen, W., & Zhao, H. (2011). *Temperature sensing experiment of fiber Bragg grating packaged by copper capillary without strain*. Paper presented at the Optoelectronics and Microelectronics Technology (AISOMT)
- Wu, Q., Semenova, Y., Wang, P., & Farrell, G. (2011). High sensitivity SMS fiber structure based refractometer—analysis and experiment. *Optics Express*, 19(9), 7937-7944.
- Zhang, N., Chen, W., Zheng, X., Hu, W., & Gao, M.-L. (2013). Optical sensor for steel corrosion monitoring based on etched fiber Bragg grating sputtered with iron film.

- Abdelghani, A., Chovelon, J., Jaffrezic-Renault, N., Veilla, C., & Gagnaire, H. (1997). Chemical vapour sensing by surface plasmon resonance optical fibre sensor coated with fluoropolymer. *Analytica Chimica Acta*, 337(2), 225-232.
- Abrate, S. (2002). Structural Monitoring with Fiber Optic Technology. *Applied Mechanics Reviews*, 55, 10.
- Ali, S. M. U., Alvi, N., Ibupoto, Z., Nur, O., Willander, M., & Danielsson, B. (2011). Selective potentiometric determination of uric acid with uricase immobilized on ZnO nanowires. *Sensors and Actuators B: Chemical*, 152(2), 241-247.
- Ali, S. M. U., Ibupoto, Z. H., Kashif, M., Hashim, U., & Willander, M. (2012). A potentiometric indirect uric acid sensor based on ZnO nanoflakes and immobilized uricase. *Sensors*, 12(3), 2787-2797.
- Allsop, T., Reeves, R., Webb, D. J., Bennion, I., & Neal, R. (2002). A high sensitivity refractometer based upon a long period grating Mach-Zehnder interferometer. *Review of scientific instruments*, 73(4), 1702-1705.
- Alvarez-Herrero, A., Guerrero, H., & Levy, D. (2004). High-sensitivity sensor of low relative humidity based on overlay on side-polished fibers. *Sensors Journal, IEEE*, 4(1), 52-56.
- Ameduri, B., & Boutevin, B. (2005). Update on fluoroelastomers: from perfluoroelastomers to fluorosilicones and fluorophosphazenes. *Journal of fluorine chemistry*, 126(2), 221-229.
- Ansari, F. (2005). *Sensing issues in civil structural health monitoring* (Vol. 10): Springer.
- Arora, K., Tomar, M., & Gupta, V. (2014). Reagentless uric acid biosensor based on Ni microdiscs-loaded NiO thin film matrix. *Analyst*, 139(18), 4606-4612.
- Arregui, F. J. (2009). *Sensors based on nanostructured materials*: Springer.
- Azamian, B. R., Davis, J. J., Coleman, K. S., Bagshaw, C. B., & Green, M. L. (2002). Bioelectrochemical single-walled carbon nanotubes. *Journal of the American Chemical Society*, 124(43), 12664-12665.
- Balta, J., Bosia, F., Michaud, V., Dunkel, G., Botsis, J., & Månson, J. (2005). Smart composites with embedded shape memory alloy actuators and fibre Bragg grating sensors: activation and control. *Smart materials and structures*, 14(4), 457.
- Bariain, C., Matías, I. R., Arregui, F. J., & Lopez-Amo, M. (2000). Optical fiber humidity sensor based on a tapered fiber coated with agarose gel. *Sensors and Actuators B: Chemical*, 69(1), 127-131.
- Batimalay, M., Ahmad, F., Lokman, A., Jasim, A., Wadi Harun, S., & Ahmad, H. (2014). Tapered plastic optical fiber coated with single wall carbon nanotubes polyethylene oxide composite for measurement of uric acid concentration. *Sensor Review*, 34(1), 75-79.
- Batimalay, M., Harith, Z., Rafaie, H., Ahmad, F., Khasanah, M., Harun, S., . . . Ahmad, H. (2014). Tapered plastic optical fiber coated with ZnO nanostructures for the measurement of uric acid concentrations and changes in relative humidity. *Sensors and Actuators A: Physical*, 210, 190-196.

- Batumalay, M., & Harun, S. W. (2013). *Relative humidity measurement using tapered plastic fiber coated with HEC/PVDF*. Paper presented at the Technology, Informatics, Management, Engineering, and Environment (TIME-E), 2013 International Conference on.
- Batumalay, M., Lokman, A., Ahmad, F., Arof, H., Ahmad, H., & Harun, S. W. (2013). Tapered plastic optical fiber coated with HEC/PVDF for measurement of relative humidity. *Sensors Journal, IEEE, 13*(12), 4702-4705.
- Bergström, J., & Hilbert, L. (2005). A constitutive model for predicting the large deformation thermomechanical behavior of fluoropolymers. *Mechanics of Materials, 37*(8), 899-913.
- Blake, J. N. (1997). Fiber optic interferometric circuit and magnetic field sensor: Google Patents.
- Bradley, K., Cumings, J., Star, A., Gabriel, J.-C. P., & Grüner, G. (2003). Influence of mobile ions on nanotube based FET devices. *Nano Letters, 3*(5), 639-641.
- Brambilla, G., Jung, Y., & Renna, F. (2010). Optical fiber microwires and nanowires manufactured by modified flame brushing technique: properties and applications. *Frontiers of Optoelectronics in China, 3*(1), 61-66.
- Brambilla, G., Xu, F., & Feng, X. (2006). Fabrication of optical fibre nanowires and their optical and mechanical characterisation. *Electronics Letters, 42*(9), 517-519.
- Chen, L. H., Li, T., Chan, C. C., Menon, R., Balamurali, P., Shailender, M., . . . Wong, W. C. (2012). Chitosan based fiber-optic Fabry–Perot humidity sensor. *Sensors and Actuators B: Chemical, 169*, 167-172.
- Choi, H. Y., Kim, M. J., & Lee, B. H. (2007). All-fiber Mach-Zehnder type interferometers formed in photonic crystal fiber. *Optics Express, 15*(9), 5711-5720.
- Chou, P., Lin, K.-C., Lin, H.-Y., & Tsai, S.-T. (2001). Gender differences in the relationships of serum uric acid with fasting serum insulin and plasma glucose in patients without diabetes. *The Journal of rheumatology, 28*(3), 571-576.
- Clark, A. H., & Ross-Murphy, S. B. (1987). Structural and mechanical properties of biopolymer gels *Biopolymers* (pp. 57-192): Springer.
- Corres, J. M., Arregui, F. J., & Matías, I. R. (2007). Sensitivity optimization of tapered optical fiber humidity sensors by means of tuning the thickness of nanostructured sensitive coatings. *Sensors and Actuators B: Chemical, 122*(2), 442-449.
- Corres, J. M., Matias, I. R., & Arregui, F. J. (2008). Optical Fibre Humidity Sensors Using Nano-films *Sensors* (pp. 153-177): Springer.
- Culshaw, B. (1984). *Optical fibre sensing and signal processing*: Peregrinus.
- Dawood, T., Shenoi, R., & Sahin, M. (2007). A procedure to embed fibre Bragg grating strain sensors into GFRP sandwich structures. *Composites Part A: Applied Science and Manufacturing, 38*(1), 217-226.

- Del Villar, I., Zamarreño, C. R., Hernaez, M., Arregui, F. J., & Matias, I. R. (2010). Resonances in coated long period fiber gratings and cladding removed multimode optical fibers: a comparative study. *Optics Express*, *18*(19), 20183-20189.
- Demathieu, C., Chehimi, M. M., & Lipskier, J.-F. (2000). Inverse gas chromatographic characterization of functionalized polysiloxanes. Relevance to sensors technology. *Sensors and Actuators B: Chemical*, *62*(1), 1-7.
- Ding, J.-F., Shao, L.-Y., Yan, J.-H., & He, S. (2005). Fiber-taper seeded long-period grating pair as a highly sensitive refractive-index sensor. *Photonics Technology Letters, IEEE*, *17*(6), 1247-1249.
- Ding, L., Belacel, C., Ducci, S., Leo, G., & Favero, I. (2010). Ultralow loss single-mode silica tapers manufactured by a microheater. *Applied optics*, *49*(13), 2441-2445.
- Doliba, N. M., Wehrli, S. L., Babsky, A. M., Doliba, N. M., & Osbakken, M. D. (1998). Encapsulation and perfusion of mitochondria in agarose beads for functional studies with ³¹P-NMR spectroscopy. *Magnetic resonance in medicine*, *39*(5), 679-684.
- Duan, D.-W., Rao, Y.-J., Xu, L.-C., Zhu, T., Deng, M., Wu, D., & Yao, J. (2011). In-Fiber Fabry-Perot and Mach-Zehnder interferometers based on hollow optical fiber fabricated by arc fusion splicing with small lateral offsets. *Optics Communications*, *284*(22), 5311-5314.
- Erden, P. E., & Kılıç, E. (2013). A review of enzymatic uric acid biosensors based on amperometric detection. *Talanta*, *107*, 312-323.
- Estella, J., de Vicente, P., Echeverría, J. C., & Garrido, J. J. (2010). A fibre-optic humidity sensor based on a porous silica xerogel film as the sensing element. *Sensors and Actuators B: Chemical*, *149*(1), 122-128.
- Fan, Y.-e., Zhu, T., Shi, L., & Rao, Y.-J. (2011). Highly sensitive refractive index sensor based on two cascaded special long-period fiber gratings with rotary refractive index modulation. *Applied optics*, *50*(23), 4604-4610.
- Fávero, F. C., Quintero, S. M., Martelli, C., Braga, A., Silva, V. V., Carvalho, I., . . . Valente, L. C. (2010). Hydrostatic pressure sensing with high birefringence photonic crystal fibers. *Sensors*, *10*(11), 9698-9711.
- Ferin, R., Pavão, M. L., & Baptista, J. (2013). Rapid, sensitive and simultaneous determination of ascorbic and uric acids in human plasma by ion-exclusion HPLC-UV. *Clinical biochemistry*, *46*(7), 665-669.
- Friedbacher, G., & Bubert, H. (2011). *Surface and Thin Film Analysis: A Compendium of Principles, Instrumentation, and Applications*: John Wiley & Sons.
- Fu, H., Tam, H., Shao, L.-Y., Dong, X., Wai, P., Lu, C., & Khijwania, S. K. (2008). Pressure sensor realized with polarization-maintaining photonic crystal fiber-based Sagnac interferometer. *Applied optics*, *47*(15), 2835-2839.
- Gehrich, J. L., Lübbers, D. W., Opitz, N., Hansmann, D. R., Miller, W. W., Tusa, J. K., & Yafuso, M. (1986). Optical fluorescence and its application to an intravascular

blood gas monitoring system. *Biomedical Engineering, IEEE Transactions on*(2), 117-132.

Golnabi, H. (2000). Simulation of interferometric sensors for pressure and temperature measurements. *Review of scientific instruments*, 71(4), 1608-1613.

Grattan, K. T., & Meggitt, B. (1995). *Optical fiber sensor technology* (Vol. 1): Springer.
Guisseppi-Elie, A., Lei, C., & Baughman, R. H. (2002). Direct electron transfer of glucose oxidase on carbon nanotubes. *Nanotechnology*, 13(5), 559.

Gusatti, M., Barroso, G. S., Campos, C. E. M. d., Souza, D. A. R. d., Rosário, J. d. A. d., Lima, R. B., . . . Kuhnen, N. C. (2011). Effect of different precursors in the chemical synthesis of ZnO nanocrystals. *Materials Research*, 14(2), 264-267.

Hariharan, P. (2003). *Optical interferometry*: Academic press.

Harun, S. W., Jasim, A., Rahman, H. A., Muhammad, M. Z., & Ahmad, H. (2013). Micro-ball lensed fiber-based glucose sensor. *Sensors Journal, IEEE*, 13(1), 348-350.

Hassan, M. R. A., Bakar, M. H. A., Dambul, K., & Adikan, F. R. M. (2012). Optical-based sensors for monitoring corrosion of reinforcement rebar via an etched cladding Bragg grating. *Sensors*, 12(11), 15820-15826.

Hernández, G. (1988). *Fabry-Perot Interferometers* (Vol. 3): Cambridge University Press.

Huang, Z., Zhu, Y., Chen, X., & Wang, A. (2005). Novel intrinsic Fabry-Perot fiber sensor using single mode-multimode-single mode structure. *IEEE Photon. Technol. Lett*, 17, 2403-2405.

Iglesias, O., Garcia, A., Roques, M., & Bueno, J. (1993). Drying of water gels: determination of the characteristic curve of agar-agar. *Drying technology*, 11(3), 571-587.

Iijima, S. (1991). Helical microtubules of graphitic carbon. *nature*, 354(6348), 56-58.

Iveković, D., Japćec, M., Solar, M., & Živković, N. (2012). Amperometric uric acid biosensor with improved analytical performances based on alkaline-stable H₂O₂ transducer. *Int. J. Electrochem. Sci*, 7, 3252-3264.

Jiang, M., & Gerhard, E. (2001). A simple strain sensor using a thin film as a low-finesse fiber-optic Fabry-Perot interferometer. *Sensors and Actuators A: Physical*, 88(1), 41-46.

Kasap, S. O. (2012). *Optoelectronics & Photonics: Principles & Practices*: Pearson Higher Ed.

Keiser, G. (2003). *Optical fiber communications*: Wiley Online Library.

Khan, M. M. I., Haque, A.-M. J., & Kim, K. (2013). Electrochemical determination of uric acid in the presence of ascorbic acid on electrochemically reduced graphene oxide modified electrode. *Journal of Electroanalytical Chemistry*, 700, 54-59.

Khijwania, S., & Gupta, B. (2000). Maximum achievable sensitivity of the fiber optic evanescent field absorption sensor based on the U-shaped probe. *Optics Communications*, 175(1), 135-137.

- Kim, D. W., Zhang, Y., Cooper, K. L., & Wang, A. (2005). In-fiber reflection mode interferometer based on a long-period grating for external refractive-index measurement. *Applied optics*, *44*(26), 5368-5373.
- Kissinger, H. E. (1957). Reaction kinetics in differential thermal analysis. *Analytical chemistry*, *29*(11), 1702-1706.
- Koehne, J., Chen, H., Li, J., Cassell, A. M., Ye, Q., Ng, H. T., . . . Meyyappan, M. (2003). Ultrasensitive label-free DNA analysis using an electronic chip based on carbon nanotube nanoelectrode arrays. *Nanotechnology*, *14*(12), 1239.
- Kurihara, H., Torigoe, S., Omura, M., Saito, K., Kurihara, M., & Matsubara, S. (1998). DNA fragmentation induced by a cytoplasmic extract from irradiated cells. *Radiation research*, *150*(3), 269-274.
- Lee, B. H., Kim, Y. H., Park, K. S., Eom, J. B., Kim, M. J., Rho, B. S., & Choi, H. Y. (2012). Interferometric fiber optic sensors. *Sensors*, *12*(3), 2467-2486.
- Li, B., Jiang, L., Wang, S., Zhou, L., Xiao, H., & Tsai, H.-L. (2011). Ultra-abrupt tapered fiber Mach-Zehnder interferometer sensors. *Sensors*, *11*(6), 5729-5739.
- Li, E., Wang, X., & Zhang, C. (2006). Fiber-optic temperature sensor based on interference of selective higher-order modes.
- Li, J., Lu, Y., Ye, Q., Cinke, M., Han, J., & Meyyappan, M. (2003). Carbon nanotube sensors for gas and organic vapor detection. *Nano Letters*, *3*(7), 929-933.
- Li, Y., Harris, E., Chen, L., & Bao, X. (2010). Application of spectrum differential integration method in an in-line fiber Mach-Zehnder refractive index sensor. *Optics Express*, *18*(8), 8135-8143.
- Lim, K., Harun, S., Damanhuri, S., Jasim, A., Tio, C., & Ahmad, H. (2011). Current sensor based on microfiber knot resonator. *Sensors and Actuators A: Physical*, *167*(1), 60-62.
- Liu, Y., Jian-er, Z., Larbot, A., & Persin, M. (2007). Preparation and characterization of nano-zinc oxide. *Journal of Materials Processing Technology*, *189*(1), 379-383.
- López-Higuera, J. M. (2002). *Handbook of optical fibre sensing technology*: Wiley.
- Love, J., Henry, W., Stewart, W., Black, R., Lacroix, S., & Gonthier, F. (1991). Tapered single-mode fibres and devices. Part 1: Adiabaticity criteria. *IEE Proceedings J (Optoelectronics)*, *138*(5), 343-354.
- Lu, P., Men, L., Sooley, K., & Chen, Q. (2009). Tapered fiber Mach-Zehnder interferometer for simultaneous measurement of refractive index and temperature. *Applied Physics Letters*, *94*(13), 131110.
- Lucki, M., Bohac, L., & Zeleny, R. (2014). *Fiber Optic and Free Space Michelson Interferometer—Principle and Practice*.
- Lye, P., Boerkamp, M., Ernest, A., & Lamb, D. (2005). *Investigating the sensitivity of PMMA optical fibres for use as an evanescent field absorption sensor in aqueous solutions*. Paper presented at the Journal of Physics: Conference Series.

- Machavaram, V., Badcock, R., & Fernando, G. (2007). Fabrication of intrinsic fibre Fabry–Perot sensors in silica fibres using hydrofluoric acid etching. *Sensors and Actuators A: Physical*, 138(1), 248-260.
- Miao, Y., Liu, B., Zhang, H., Li, Y., Zhou, H., Sun, H., . . . Zhao, Q. (2009). Relative humidity sensor based on tilted fiber Bragg grating with polyvinyl alcohol coating. *Photonics Technology Letters, IEEE*, 21(7), 441-443.
- Mignani, A. G., & Baldini, F. (1996). Biomedical sensors using optical fibres. *Reports on Progress in Physics*, 59(1), 1.
- Moon, D. S., Kim, B. H., Lin, A., Sun, G., Han, Y.-G., Han, W.-T., & Chung, Y. (2007). The temperature sensitivity of Sagnac loop interferometer based on polarization maintaining side-hole fiber. *Optics Express*, 15(13), 7962-7967.
- Morisawa, M., Amemiya, Y., Kohzu, H., Liang, C. X., & Muto, S. (2001). Plastic optical fibre sensor for detecting vapour phase alcohol. *Measurement Science and Technology*, 12(7), 877.
- Muhammad, M., Jasim, A., Ahmad, H., Arof, H., & Harun, S. (2013). Non-adiabatic silica microfiber for strain and temperature sensors. *Sensors and Actuators A: Physical*, 192, 130-132.
- Müller, M. S., Buck, T. C., & Koch, A. W. (2009). *Fiber Bragg grating-based acceleration sensor*. Paper presented at the Optomechatronic Technologies, 2009. ISOT 2009. International Symposium on.
- Muto, S., Suzuki, O., Amano, T., & Morisawa, M. (2003). A plastic optical fibre sensor for real-time humidity monitoring. *Measurement Science and Technology*, 14(6), 746.
- Nguyen, L. V., Hwang, D., Moon, S., Moon, D. S., & Chung, Y. (2008). High temperature fiber sensor with high sensitivity based on core diameter mismatch. *Optics Express*, 16(15), 11369-11375.
- Peng, Y. (2013). A Novel Sensor for Uric Acid Based on an Electropolymerization Technique. *AMERICAN LABORATORY*, 45(8), 26-28.
- Qi, Z.-m., Honma, I., & Zhou, H. (2006). Humidity sensor based on localized surface plasmon resonance of multilayer thin films of gold nanoparticles linked with myoglobin. *Optics letters*, 31(12), 1854-1856.
- Rahman, H., Harun, S., Yasin, M., Phang, S., Damanhuri, S., Arof, H., & Ahmad, H. (2011). Tapered plastic multimode fiber sensor for salinity detection. *Sensors and Actuators A: Physical*, 171(2), 219-222.
- Rahman, N. A., Hasan, M., Hussain, M., & Jahim, J. (2008). Determination of glucose and fructose from glucose isomerization process by high performance liquid chromatography with UV detection. *Modern Applied Science*, 2(4), p151.
- Scarselli, M., Castrucci, P., & De Crescenzi, M. (2012). Electronic and optoelectronic nano-devices based on carbon nanotubes. *Journal of Physics: Condensed Matter*, 24(31), 313202.

- Sekar, A., Kim, S., Umar, A., & Hahn, Y. (2005). Catalyst-free synthesis of ZnO nanowires on Si by oxidation of Zn powders. *Journal of Crystal Growth*, 277(1), 471-478.
- Silva, L. I., Rocha-Santos, T. A., & Duarte, A. (2008). Development of a fluorosiloxane polymer-coated optical fibre sensor for detection of organic volatile compounds. *Sensors and Actuators B: Chemical*, 132(1), 280-289.
- Srimannarayana, K., Shankar, M., Prasad, R. L. S., Mohan, T. K., Ramakrishna, S., Srikanth, G., & Rao, S. R. P. (2008). Fiber Bragg grating and long period grating sensor for simultaneous measurement and discrimination of strain and temperature effects. *Optica applicata*, 38(3), 601-608.
- Star, A., Gabriel, J.-C. P., Bradley, K., & Grüner, G. (2003). Electronic detection of specific protein binding using nanotube FET devices. *Nano Letters*, 3(4), 459-463.
- Stokes, R., & Robinson, R. (1966). Interactions in aqueous nonelectrolyte solutions. I. Solute-solvent equilibria. *The Journal of Physical Chemistry*, 70(7), 2126-2131.
- Subramanyam, T., Srinivasulu Naidu, B., & Uthanna, S. (2000). Physical properties of zinc oxide films prepared by dc reactive magnetron sputtering at different sputtering pressures. *Crystal Research and Technology*, 35(10), 1193-1202.
- Sumetsky, M., Dulashko, Y., Fini, J., Hale, A., & DiGiovanni, D. (2006). The microfiber loop resonator: Theory, experiment, and application. *Lightwave Technology, Journal of*, 24(1), 242-250.
- Sun, A., Li, Z., Wei, T., Li, Y., & Cui, P. (2009). Highly sensitive humidity sensor at low humidity based on the quaternized polypyrrole composite film. *Sensors and Actuators B: Chemical*, 142(1), 197-203.
- Swart, P. L. (2004). Long-period grating Michelson refractometric sensor. *Measurement Science and Technology*, 15(8), 1576.
- Thakur, B., & Sawant, S. N. (2013). Polyaniline/Prussian-Blue-Based Amperometric Biosensor for Detection of Uric Acid. *ChemPlusChem*, 78(2), 166-174.
- Tian, Z. (2008). In-line optical fiber interferometric refractive index sensors.
- Tian, Z., & Yam, S.-H. (2009). In-line abrupt taper optical fiber Mach-Zehnder interferometric strain sensor. *IEEE Photonics Technology Letters*, 3(21), 161-163.
- Tian, Z., Yam, S. S.-H., Barnes, J., Bock, W., Greig, P., Fraser, J. M., . . . Oleschuk, R. D. (2008). Refractive index sensing with Mach-Zehnder interferometer based on concatenating two single-mode fiber tapers. *Photonics Technology Letters, IEEE*, 20(8), 626-628.
- Tian, Z., Yam, S. S., & Loock, H.-P. (2008). Refractive index sensor based on an abrupt taper Michelson interferometer in a single-mode fiber. *Optics letters*, 33(10), 1105-1107.

- Tong, L. (2010). Brief introduction to optical microfibers and nanofibers. *Frontiers of Optoelectronics in China*, 3(1), 54-60.
- Tracey, P. M. (1991). Intrinsic fiber-optic sensors. *Industry Applications, IEEE Transactions on*, 27(1), 96-98.
- Udd, E., Michal, R. J., Watanabe, S. F., Theriault, J. P., & Cahill, R. F. (1988). Fiber optic sensor: Google Patents.
- Udd, E., & Spillman Jr, W. B. (2011). *Fiber optic sensors: an introduction for engineers and scientists*: John Wiley & Sons.
- Viswanathan, R., & Gupta, R. B. (2003). Formation of zinc oxide nanoparticles in supercritical water. *The Journal of supercritical fluids*, 27(2), 187-193.
- Vo-Dinh, T., Alarie, J.-P., Cullum, B. M., & Griffin, G. D. (2000). Antibody-based nanoprobe for measurement of a fluorescent analyte in a single cell. *Nature biotechnology*, 18(7), 764-767.
- Wang, P., Liu, J., Li, C., Chen, W., & Zhao, H. (2011). *Temperature sensing experiment of fiber Bragg grating packaged by copper capillary without strain*. Paper presented at the Optoelectronics and Microelectronics Technology (AISOMT), 2011 Academic International Symposium on.
- Wang, Y., Yang, M., Wang, D., Liu, S., & Lu, P. (2010). Fiber in-line Mach-Zehnder interferometer fabricated by femtosecond laser micromachining for refractive index measurement with high sensitivity. *JOSA B*, 27(3), 370-374.
- Wang, Z., Shen, F., Song, L., Wang, X., & Wang, A. (2007). Multiplexed fiber Fabry-Perot interferometer sensors based on ultrashort Bragg gratings. *Photonics Technology Letters, IEEE*, 19(8), 622-624.
- Wei, T., Han, Y., Tsai, H.-L., & Xiao, H. (2008). Miniaturized fiber inline Fabry-Perot interferometer fabricated with a femtosecond laser. *Optics letters*, 33(6), 536-538.
- Wolfbeis, O. S. (2008). Fiber-optic chemical sensors and biosensors. *Analytical chemistry*, 80(12), 4269-4283.
- Woolley, A. T., Guillemette, C., Cheung, C. L., Housman, D. E., & Lieber, C. M. (2000). Direct haplotyping of kilobase-size DNA using carbon nanotube probes. *Nature biotechnology*, 18(7), 760-763.
- Wu, D., Zhu, T., Chiang, K. S., & Deng, M. (2012). All single-mode fiber Mach-Zehnder interferometer based on two peanut-shape structures. *Journal of Lightwave Technology*, 30(5), 805-810.
- Wu, D., Zhu, T., Deng, M., Duan, D.-W., Shi, L.-L., Yao, J., & Rao, Y.-J. (2011). Refractive index sensing based on Mach-Zehnder interferometer formed by three cascaded single-mode fiber tapers. *Applied optics*, 50(11), 1548-1553.
- Wu, Q., Semenova, Y., Wang, P., & Farrell, G. (2011). High sensitivity SMS fiber structure based refractometer-analysis and experiment. *Optics Express*, 19(9), 7937-7944.

- Yao, C., Wu, H., Ge, M., Yang, L., Zeng, Y., Wang, Y., & Jiang, J. (2007). Triangle-shape ZnO prepared by thermal decomposition. *Materials Letters*, 61(16), 3416-3420.
- Yawong, O., Choopun, S., Mangkorntong, P., Mangkorntong, N., & Chiang, M. (2005). Zinc Oxide Nanostructure by Oxidization of Zinc Thin Films. *University Journal Special Issue on Nanotechnology 4 (1)*.
- Yeo, T., Sun, T., & Grattan, K. (2008). Fibre-optic sensor technologies for humidity and moisture measurement. *Sensors and Actuators A: Physical*, 144(2), 280-295.
- Yuan, L., Yang, J., & Liu, Z. (2008). A compact fiber-optic flow velocity sensor based on a twin-core fiber Michelson interferometer. *Sensors Journal, IEEE*, 8(7), 1114-1117.
- Zhang, N., Chen, W., Zheng, X., Hu, W., & Gao, M.-L. (2013). Optical sensor for steel corrosion monitoring based on etched fiber Bragg grating sputtered with iron film.
- Zheng, Y., Dong, X., Zhao, C., Li, Y., Shao, L., & Jin, S. (2013). Relative humidity sensor based on microfiber loop resonator. *Advances in Materials Science and Engineering*, 2013.
- Zhu, T., Wu, D., Liu, M., & Duan, D.-W. (2012). In-line fiber optic interferometric sensors in single-mode fibers. *Sensors*, 12(8), 10430-10449.
- Zibaii, M. I., Kazemi, A., Latifi, H., Azar, M. K., Hosseini, S. M., & Ghezelaigh, M. H. (2010). Measuring bacterial growth by refractive index tapered fiber optic biosensor. *Journal of Photochemistry and Photobiology B: Biology*, 101(3), 313-320.

LIST OF PUBLICATION AND PAPERS PRESENTED

Journal Publications

- 1) Lokman, A., Irawati, N., Arof, H., Harun, S. W., & Ali, N. M. (2014). Dumbbell shaped inline Mach-Zehnder interferometer for sensor applications. *optoelectronics and advanced materials-rapid communications*, 8(5-6), 395-398.
- 2) Lokman, A., Batumalay, M., Harun, S. W., Arof, H., & Counts, A. T. C. (2014). Humidity sensor based on tapered single mode fiber coated with a hydroxyethyl cellulose/poly-vinylidene fluoride composite. *Ukr. J. Phys. Opt*, 15, 96-101.
- 3) Lokman, A., Nodehi, S., Batumalay, M., Arof, H., Ahmad, H., & Harun, S. W. (2014). Optical fiber humidity sensor based on a tapered fiber with hydroxyethylcellulose/polyvinylidene fluoride composite. *Microwave and Optical Technology Letters*, 56(2), 380-382.
- 4) Lokman, A., Arof, H., & Harun, S. W. (2015). Dumbbell shaped inline Mach-Zehnder interferometer for glucose detection. *Measurement*, 59, 167-170.
- 5) Lokman, A., Arof, H., & Harun, S. W. Optical Fiber Relative Humidity Sensor Based on Inline Mach Zehnder Interferometer with ZnO Nanowires Coating.
- 6) Lokman, A., Arof, H., & Harun, S. W. (2015). Tapered fiber coated with hydroxyethyl cellulose/polyvinylidene fluoride composite for relative humidity sensor. *Sensors and Actuators A: Physical*, 225, 128-132.
- 7) Lokman, A., Arof, H., & Harun, S. W. Inline Mach Zehnder Interferometer with ZnO Nanowires Coating for the measurement of uric acid concentrations *Sensors and Actuators A* (Under Review)
- 8) Lokman, A., Irawati, N., Arof, H., Harun, S. W., & Ali, N. M. Dumbbell Shaped Inline Mach-Zehnder Interferometer for Bio-Chemical detection. *IEEE sensors*.
(Under Review)

Papers Presented

- 1) Lokman, A., Irawati, N., Arof, H., Harun, S. W., & Ali, N. M Dumbbell shaped inline Mach–Zehnder interferometer for glucose detection. Regional Conference on Science, Technology and Social Sciences.
- 2) Lokman, A., Arof, H., Ali, N. M., & Harun, S. W. (2015). Dumbbell shaped inline Mach–Zehnder interferometer for bio-chemical detection. *Jurnal Teknologi*, 74(8).

University of Malaya

APPENDIX

A selection of published works are attached in this appendix.

University of Malaya